공학박사 학위논문

Microstructure engineering, mechanical properties, and coloration of lithium disilicate glass-ceramics

리튬다이실리케이트 결정화 유리의 미세구조 제어,
기계적 물성 및 착색 특성

2020 년 8 월
서울대학교 대학원
재료공학부
김 다 미

Abstract

Microstructure engineering, mechanical properties, and coloration of lithium disilicate glass-ceramics

Dami Kim

Department of Materials Science and Engineering

Graduate School

Seoul National University

As dental loss and periodontal disease increase due to global aging, so does the demand for dental prostheses. Among various artificial dental materials, lithium disilicate ($Li_2Si_2O_5$, LS2) glass-ceramics (GCs) have been used for the anterior application like ceramic crown materials owing to their excellent aesthetics and mechanical properties. Recently, it has been impossible for a large number of patients to use multiple fixtures placed on the gum bone owing to weakening of the gum bone caused by old age, and thus the demand for fixed dental prostheses has increased greatly.

Since fixed dental prostheses require mechanical properties superior to single crowns, it is necessary to improve the mechanical properties of the LS2 GCs. While several studies have been conducted to improve the mechanical properties of LS2 GCs, no remarkable improvement has been reported. In order to improve the mechanical strength of the GCs, it is essential to control the microstructure, but a systematic approach for this point had never been tried sufficiently, which motivated the first topic of crystallization sequence and microstructure of lithium disilicate glass-ceramics. In this study, to control the microstructure of LS2 GCs, we attempted a new approach by investigating the crystallization sequence for the SiO_2-Li_2O-K_2O-ZnO-P_2O_5 system. To investigate the crystallization behavior, the Z/K ratios of precursor glasses were varied from 0 to 3.5 while the nucleating agent of P_2O_5 and glass modifiers of ZnO plus K_2O were fixed to have 1.5 and 4.5 mol% relative to LS2, respectively. For the samples prepared by two-stage heat treatments of 500 ℃ for 1 h and 800 ℃ for 2 h in air, the LS2 nucleation rate was increased with increasing the Z/K ratio due to the variation in crystallization sequence from type II (Li_2SiO_3: LS) to type I (LS+LS2) in addition to an amorphous phase separation in base glass. Consequently, with increasing the Z/K ratio, the LS2 crystalline phase within the glass matrix continuously changed from larger acicular ones to smaller equiaxed ones. Within the best of our knowledge, this is the first report that the crystallization sequence can be changed by adjusting the ratio of additives to induce a dramatic change in the microstructure.

Secondly, we investigated the effect of microstructure on mechanical properties of LS2 GCs for the SiO_2-Li_2O-P_2O_5-K_2O-ZnO system since microstructure engineering was enabled from the above study. The microstructures of GC samples, having three different compositions but the same total 6 mol% of additives (P_2O_5,

ZnO, K_2O), could be controlled by varying heat treatment conditions of glass samples. In addition to major LS2 crystalline phase, two other minor crystalline phases of Li_3PO_4 (LP) and cristobalite were detectable. Average crystal sizes of GC samples were in the region of 0.3 – 10 μm, and the volume fractions of crystalline phases were in the region of 0.70–0.73. The biaxial flexural strength was improved with decreasing the average crystal size from ~10 to ~1 μm by following the Hall-Petch relationship, and the maximum flexural strength of 445.8 ± 7.2 MPa was obtainable from the GC samples with the additive compositions of 1.5 mol% P_2O_5, 2.75 mol% K_2O and 2 mol% of ZnO which were nucleated at 540 ºC for 1 h and grown at 850 ºC for 4 h. When 8.4 vol.% cristobalite was incorporated into the sample, however, there was a severe scattering in flexural strength data due to the formation of microcracks induced by the beta-to-alpha transition of cristobalite and also due to a micro tensile stress in the residual glassy phase induced by a large difference in thermal expansion coefficients between crystal and residual glassy phases. Meanwhile, the Vickers hardness was increased with decreasing the average crystal size down to ~0.3 μm, indicating that the factors for the deterioration of flexural strength have a negligible effect on hardness. It can also be suggested that the biaxial flexural strength may be further improved by decreasing the crystal size if the formation of cristobalite phase in GCs can be avoided or at least suppressed below a certain amount, and also by minimizing the micro tensile stress in the residual glassy phase due to the difference in the TEC between the crystalline phases and the residual glassy phase.

Thirdly, for the dental application of LS2 GCs, it is essential to reproduce color and transparency similar to human teeth for the patient satisfaction. However, it is very difficult to identify the coloration mechanism of LS2 GCs, and thus it is hard

to find reports on this topic. Therefore, tried to identify the coloring mechanism of the V_2O_5 colorant, which is known to impart yellowish color, and its effect on crystallization behavior for two different systems of SiO_2-Li_2O-P_2O_5-K_2O-ZnO and SiO_2-Li_2O-P_2O_5-K_2O-Al_2O_3. For this study, the amount of V_2O_5, SiO_2 + Li_2O, and P_2O_5 were fixed to have 0.5, 93.5, and 1.5 mol%, respectively, while the ratios of both ZnO/K_2O (Zn/K) and Al_2O_3/K_2O (Al/K) were varied from 0.5 to 2. The GC samples were prepared by two-stage heat treatments of 500 °C for 1 h as a nucleation stage and 600, 700, and 800 °C for 2 h as a growth stage in air. The light green glass samples having only V^{5+} ion continuously changed to violet, blue, green, and brown for GC samples due to its reduction into V^{4+} and V^{3+} ions with progressing crystallization. TEM-EDS analyses revealed that a small amount of V^{5+} ion was incorporated into both LS2 and SiO_2 crystalline phases, causing greenish fluorescence, while most of vanadium ions remained in a residual glassy matrix. At the growth temperature of 800 °C, while the growth rate of LS2 was increased by lowering the viscosity of the glass matrix, and thus the LS2 crystal size of the $GVZ_{1.5}$ and GVZ_3 samples became larger (~1 μm) compared with its size below 500 nm for the samples without V_2O_5 colorant. The $GVAl_{1.5}$ and $GVAl_3$ samples exhibited the smaller size (<1 mm) than $GVZ_{1.5}$ and GVZ_3 samples because of higher nucleation rate and lower growth rate, leading to undesirable high translucency for the dental application. The color of LS2 GCs was found to change with crystallization due to a variation in the valency state of the colorant V ions in residual glassy matrix, suggesting that the design of the residual glassy matrix after crystallization is crucial for the coloration of LS2 GCs.

Finally, in order to achieve the color similar to human teeth, the effects of CeO_2 and TiO_2 colorants on coloration, crystallization behavior, and mechanical properties

were investigated for the SiO_2-Li_2O-K_2O-ZnO-P_2O_5 system. Combination of CeO_2 and TiO_2 were chosen since they are known to impart a yellowish color which is sufficient to reproduce colors similar to human teeth. As a result, the combination of CeO_2 and TiO_2 enhanced yellowish color as the Ti^{4+} ion reduced Ce^{4+} to Ce^{3+} ion. However, the significant decrease in reddish color, which is required to produce a human tooth color, was obtained. In addition, the translucency was too high for dental application. Meanwhile, nano-sized CeO_2 crystalline phase precipitated with the addition of 1 mol% or more of CeO_2, lowering translucency than human teeth. It was found that CeO_2 acted as a nucleation inhibitor of LS2 crystals, resulting in a decrease in mechanical strength as the crystal size increased. On the other hand, with the ternary colorants of CeO_2-V_2O_5-MnO_2 for the SiO_2-Li_2O-K_2O-ZnO-P_2O_5 system, where MnO_2 was selected as a reddish coloring agent, reddish color was insufficient because Mn^{3+} ions are reduced to colorless Mn^{2+} by Ce^{4+}, which made us to know that it is critical to select a colorant whose valency is unaltered by other additives. Therefore, by adding Er_2O_3 to the CeO_2-V_2O_5-Er_2O_3 mixture for reddish color, it was possible to realize the colors similar to human teeth for the SiO_2-Li_2O-K_2O-ZnO-P_2O_5 system. Consequently, LS2 GCs similar to human teeth with a biaxial flexural strength of 430 MPa could be successfully fabricated.

Table of contents

List of tables

List of figures

Chapter 1

Introduction

Glass-ceramics (GCs), usually produced by forming a crystalline phase in an amorphous matrix, are known to possess good characteristics such as high fracture toughness, high chemical stability, low thermal expansion coefficient, high transparency in the visible light, and a low dielectric constant [1]. Hence, they have been widely used for real applications such as insulating (or sealing) materials, optical grating, telescope mirror, radomes, magnetic memory disk substrates, cooktops, and medical applications [2-4].

Dental restoration materials require good biocompatibility, high strength, and high aesthetics to meet the demands of patients. All-ceramic systems have become commercially available since the 1980s because their translucency is superior to traditional porcelain fused to metal [5], and they fulfill the aesthetic requirements for dental applications. For the application of posterior teeth, mechanical properties are more important than aesthetics as they receive relatively higher load. Meanwhile, for anterior teeth, the aesthetics is more important than mechanical properties even though high strength is required as well.

Lithium disilicate (LS2) glass-ceramics (GCs) have been successfully used for dental restoration in the past few decades because of their high flexural strength (σ_f) of 400 ± 40 MPa and high fracture toughness (K_{IC}) of 3.3 ± 0.3 MPa$\cdot$m$^{0.5}$ which are

typically achieved by the molding/pressing process [5, 6]. In particular, due to their high quality aesthetics such as their producibility in various shades and translucencies, LS2 GCs have been applied to all-ceramic crowns for the anterior teeth region [7]. Moreover, advanced computer-aided design and manufacturing technologies (CAD/CAM) have increased the market share of LS2 GCs when the machinable lithium metasilicate (LS) block was firstly introduced in 2006. When an LS block with an appropriate shape after milling is transformed into the LS2 phase at approximately 850 °C, it normally possesses good mechanical properties of $\sigma_f >$ 300 MPa and $K_{IC} \approx 2.3$ MPa·m$^{0.5}$ [4, 8].

Dental zirconia, typically 3 mol% yttrium-stabilized tetragonal zirconia polycrystalline ceramics, has been successfully applied to dental restoration in various forms such as crowns, fixed partial dentures, implant abutments, and dental implants due to its high flexural strength of 900–1200 MPa and high fracture toughness of 9–10 MPa·m$^{1/2}$ [9-11]. Zirconia is highly attractive for anterior application because of its superior mechanical properties. Its opaque features, however, hinder real application. Recently, the translucent nano-sized zirconia has been reported, which was fabricated at the sintering temperatures ranging from 1000–1100 °C by using the spark plasma sintering technique [12]. However, the translucency of nano-sized zirconia was incompatible to LS2 GCs because of light scattering at the residual pores. Residual pores are unavoidable with the sintering process, and a significant decrease in translucency occurs when the thickness exceeds 0.75 mm [7, 12-15]. Therefore, LS2 GCs are still preferable for anterior application because of its high translucency. Nevertheless, the mechanical properties of LS2 GCs should be further improved for the longevity of the product and survival rate of the current anterior application, and also for the potential application of

posterior three-unit dental bridges requiring no less than 500 MPa flexural strength and 3.5 MPa·m$^{1/2}$ fracture toughness [16].

In order to improve the mechanical strength of LS2 GCs in a multicomponent system with nucleating agents or glass modifiers, enormous efforts have been made to refine the LS2 crystal embedded in GCs through an optimal heat treatment condition. A fine-grained LS2 microstructure is normally achievable by employing nucleating agents such as P_2O_5, ZrO_2, and TiO_2. Among these additives, P_2O_5 is known to be the most effective for increasing the nucleation rate since it promotes the bulk nucleation of LS2 by forming a steep compositional gradient in the vicinity of amorphous LP phase, where it acts as the heterogeneous nucleation site for both metastable LS and stable LS2 phases [17, 18]. Krüger *et al.* [14] demonstrated that, while ZrO_2 increases the nucleation rate of LS phase in the early crystallization stage, it suppresses the growth rate of LS2 phase because the zirconium ion increases the viscosity of the residual glassy phase, leading to lowered mechanical strength [19, 20]. Also, it is reported that TiO_2 dominantly promotes surface nucleation which is less effective for the improvement of mechanical strength [21]. Optimal three-step heat treatments are reported to induce highly intertwined colonies in the microstructure, leading to a high flexural strength of 562 ± 107 MPa and a high fracture toughness of 3.5 ± 0.1 MPa·m$^{1/2}$ [22].

Also, the additives for the crystallization in GCs greatly influence the crystallization sequence during heat treatment, which can cause the formation of metastable phases or secondary phases, and vary the nucleation and growth of final crystalline phases. In the Li_2O-SiO_2 binary system as well as multicomponent LS2 systems, many researchers reported the lithium metasilicate (Li_2SiO_3, LS) as a

metastable phase formed earlier than the LS2 phase or simultaneously crystallized with the LS2 phase in the early crystallization stage [23-25]. According to the MAS-NMR studies on the SiO_2-Li_2O system [26, 27], the Q^m distribution concept enables the measurement of different local silicon environments in crystalline silicates, where Q species are designated as Q^4 (SiO_2), Q^3 ($Li_2O \cdot 2SiO_2$), and Q^2 ($Li_2O \cdot SiO_2$). In particular, the glass modifier K_2O is known to induce LS crystallization by causing the disproportionation of Q^3 into Q^2 and Q^4 in glass [28], and the LS phase impedes the growth of the LS2 phase [29]. By varying the glass modifiers in the LS2 system, the crystallization sequence can be controlled. Nevertheless, the effect of additives on the crystallization sequence has not yet been clarified yet.

Thus, new ideas for the further enhancement of mechanical properties of LS2 GCs is required. Therefore, we tried to understand the effect of crystallization sequence on the microstructure of LS2 GCs. **In Chapter 3**, a dramatic change in microstructure from large acicular-shaped crystal morphology to fine equiaxed crystals is controlled by the alteration of crystallization sequence from sequence type II (LS) and type I (LS+LS2). To the best of our knowledge, this report is the first regarding microstructure engineering of LS2 GCs by controlling the crystallization sequence.

Based on the results in Chapter 3, the engineered microstructure on mechanical properties is reported **in Chapter 4**. The crystal size was controlled by adding the nucleating agent P_2O_5, adjusting the ratio of the glass modifiers Z/K, and using various heat treatments. Furthermore, in order to relieve the tensile stress in the residual glassy matrix caused by a difference in the thermal expansion coefficient (TEC) between the residual glassy matrix and crystalline phases, the cristobalite

Chapter 1: Introduction

phase with higher TEC than the LS2 phase was incorporated for the enhancement of mechanical strength. The effect of cristobalite and increased TEC of residual glassy matrix on the mechanical properties of LS2 GCs are reported.

In dental restoration, both high mechanical properties and appropriate optical properties, including color and translucency well matching with (or similar to) human teeth, are required for the satisfaction of patient demands. Human teeth are primarily composed of opaque dentin and translucent enamel. The major source of color is from dentin, and translucency is a result of light reflected from the enamel surface and light scattering within enamel and dentin [30]. The color coordinates of human teeth were reported by measuring 600 individual teeth in CIELab color space with parameters L* (67.6 ±7.0), a* (4.3 ± 2.1), and b* (12.1 ± 3.3) [31]. The translucency of human teeth enamel and dentin were evaluated by translucency parameter (TP) and contrast ratio (CR). The TPs of human enamel and dentin with a thickness of 1 mm were 18.7 and 16.4, respectively, and the mean CR was inversely proportional to the TP [32].

In order to obtain a proper color in GCs, colorants are generally added to the base glass composition. Colorants normally consist of transition metals with $3d$ orbitals or rare-earth elements having $4f$ orbitals which can absorb or emit light with a specific wavelength. LS2 GCs have been doped with many kinds of colorants such as Cr_2O_3 [33], V_2O_5 and CeO_2 [34], and MnO_2 [35, 36], in order to manifest the appropriate color for the reproduction of human teeth, and their coloration was discussed in terms of optical absorption and fluorescence. However, the effect of the colorant on the optical properties and crystallization behavior in LS2 GCs have never been fully elucidated. Thus, the effort to understand the coloration mechanism with

progressing crystallization in LS2 GCs is required.

In Chapter 5, the coloration mechanism in LS2 GCs is reported. With the same amount of V_2O_5 colorant in different glass compositions, the color was dramatically changed with progressing crystallization from light greenish in glass to violet, green, and brown in GCs. The light green glass samples having only V^{5+} ion continuously changed to violet, blue, green, and brown for GC samples due to its reduction into V^{4+} and V^{3+} ions with progressing crystallization. The underlying mechanisms of the coloration mechanism in GCs is discussed qualitatively. To the best of our knowledge, a study of this kind has not been reported on the above-mentioned coloration in GCs.

In Chapter 6, the optimization of coloration for LS2 GC with various colorants are investigated. The colorants selected are CeO_2 and V_2O_5 for b* parameter (yellowish), MnO_2 and Er_2O_3 for a* parameter (reddish). Moreover, the TiO_2 was added with CeO_2 simultaneously since the mixture of CeO_2 and TiO_2 is known to impart yellowish color. Not only the coloration but also the crystallization behavior of LS2 GCs is discussed. Finally, the optimal amount of additives is determined for the imitation of color in the human teeth.

References

[1] W. Holand, G.H. Beall, Glass ceramic technology, 2nd ed ed., John Wiley & Sons inc., New Jersey, 2012.

[2] E.D. Zanotto, Bright future for glass-ceramics American Ceramics Society Bulletin, 89 (2010) 19-27.

[3] O. Bretcanu, E. Verné, M. Cöisson, P. Tiberto, P. Allia, Magnetic properties of the ferrimagnetic glass-ceramics for hyperthermia, J. Magn. Magn. Mater., 305 (2006) 529-533.

[4] W. Höland, V. Rheinberger, E. Apel, C. van't Hoen, M. Höland, A. Dommann, M. Obrecht, C. Mauth, U. Graf-Hausner, Clinical applications of glass-ceramics in dentistry, Journal of Materials Science: Materials in Medicine, 17 (2006) 1037-1042.

[5] W. Höland, M. Schweiger, M. Frank, V. Rheinberger, A comparison of the microstructure and properties of the IPS Empress® 2 and the IPS Empress® glass-ceramics, Journal of biomedical materials research, 53 (2000) 297-303.

[6] M. Schweiger, W. Höland, M. Frank, H. Drescher, V. Rheinberger, IPS Empress 2: a new pressable high-strength glass-ceramic for esthetic all-ceramic restorations, Quintessence Dent Technol, 22 (1999) 143-151.

[7] H.H. Harianawala, M.G. Kheur, S.K. Apte, B.B. Kale, T.S. Sethi, S.M. Kheur, Comparative analysis of transmittance for different types of commercially available zirconia and lithium disilicate materials, The journal of advanced prosthodontics, 6 (2014) 456-461.

[8] C. Ritzberger, M. Schweiger, W. Höland, Principles of crystal phase formation in ivoclar vivadent glass-ceramics for dental restorations, J. Non-Cryst. Solids, 432 (2016) 137-142.

[9] P. Christel, A. Meunier, M. Heller, J. Torre, C. Peille, Mechanical properties and short-term in vivo evaluation of yttrium-oxide-partially-stabilized zirconia, Journal of biomedical materials research, 23 (1989) 45-61.

[10] B. AL-AMLEH, K. Lyons, M. Swain, Clinical trials in zirconia: a systematic review, Journal of oral rehabilitation, 37 (2010) 641-652.

[11] I. Denry, J.R. Kelly, State of the art of zirconia for dental applications, Dent. Mater., 24 (2008) 299-307.

[12] H. Zhang, B.-N. Kim, K. Morita, H.Y.K. Hiraga, Y. Sakka, Effect of sintering temperature on optical properties and microstructure of translucent zirconia prepared by high-pressure spark plasma sintering, Science and technology of advanced materials, 12 (2011) 055003.

[13] Ö. Malkondu, N. Tinastepe, E. Akan, E. Kazazoğlu, An overview of monolithic zirconia in dentistry, Biotechnology & Biotechnological Equipment, 30 (2016) 644-652.

[14] Y.-M. Chen, R.J. Smales, K.H.-K. Yip, W.-J. Sung, Translucency and biaxial flexural strength of four ceramic core materials, Dent. Mater., 24 (2008) 1506-1511.

[15] A. Vichi, M. Sedda, R. Fabian Fonzar, M. Carrabba, M. Ferrari, Comparison of Contrast Ratio, Translucency Parameter, and Flexural Strength of Traditional and "Augmented Translucency" Zirconia for CEREC CAD/CAM System, Journal of Esthetic and Restorative Dentistry, (2015).

[16] I.O.f. Standards, ISO 6872: 2008. Dentistry: ceramic materials, in, International Organization for Standards Geneva, 2008.

[17] G. Wen, X. Zheng, L. Song, Effects of P_2O_5 and sintering temperature on microstructure and mechanical properties of lithium disilicate glass-ceramics, Acta Mater., 55 (2007) 3583-3591.

[18] S.C. von Clausbruch, M. Schweiger, W. Höland, V. Rheinberger, The effect of P_2O_5 on the crystallization and microstructure of glass-ceramics in the SiO_2–Li_2O–K_2O–ZnO–P_2O_5 system, J. Non-Cryst. Solids, 263 (2000) 388-394.

[19] S. Krüger, J. Deubener, C. Ritzberger, W. Höland, Nucleation Kinetics of Lithium Metasilicate in ZrO_2-Bearing Lithium Disilicate Glasses for Dental Application, International Journal of Applied Glass Science, 4 (2013) 9-19.

[20] E. Apel, C. van't Hoen, V. Rheinberger, W. Höland, Influence of ZrO_2 on the crystallization and properties of lithium disilicate glass-cer amics derived from a multi-component system, J. Eur. Ceram. Soc., 27 (2007) 1571-1577.

[21] H.R. Fernandes, D.U. Tulyaganov, J.M.F. Ferreira, The role of P_2O_5, TiO_2 and ZrO_2 as nucleating agents on microstructure and crystalli zation behaviour of lithium disilicate-based glass, Journal of Materials Science, 48 (2012) 765-773.

[22] S. Huang, Y. Li, S. Wei, Z. Huang, W. Gao, P. Cao, A novel hi gh-strength lithium disilicate glass-ceramic featuring a highly intertwine d microstructure, J. Eur. Ceram. Soc., 37 (2017) 1083-1094.

[23] M.P. BOROM, A.M. TURKALO, R.H. Doremus, Strength and Mi crostructure in Lithium Disilicate Glass-Ceramics, J. Am. Ceram. Soc., 58 (1975) 385-391.

[24] T. Headley, R. Loehman, Crystallization of a Glass-Ceramic by E pitaxial Growth, J. Am. Ceram. Soc., 67 (1984) 620-625.

[25] P.C. Soares, E.D. Zanotto, V.M. Fokin, H. Jain, TEM and XRD study of early crystallization of lithium disilicate glasses, J. Non-Cryst. Solids, 331 (2003) 217-227.

[26] B. De Jong, C.M. Schramm, V.E. Parziale, Silicon-29 magic angl e spinning NMR study on local silicon environments in amorphous an d crystalline lithium silicates, J. Am. Chem. Soc., 106 (1984) 4396-44 02.

[27] R. Dupree, D. Holland, M. Mortuza, A MAS-NMR investigation of lithium silicate glasses and glass ceramics, J. Non-Cryst. Solids, 116 (1990) 148-160.

[28] H.R. Fernandes, D.U. Tulyaganov, A. Goel, J.M.F. Ferreira, Effect of K_2O on structure–property relationships and phase transformations i n Li2O–SiO2 glasses, J. Eur. Ceram. Soc., 32 (2012) 291-298.

[29] S. Huang, Z. Huang, W. Gao, P. Cao, Trace phase formation, cry stallization kinetics and crystallographic evolution of a lithium disilicate glass probed by synchrotron XRD technique, Scientific reports, 5 (201

5) 9159.

[30] C.P. Bergmann, A. Stumpf, Dental Ceramics: Microstructure, Properties and Degradation, Springer Science & Business Media, 2013.

[31] M. Rubino, J. Garcia, L.J. Barco, J. Romero, Colour measurement of human teeth and evaluation of a colour guide, Color Research & Application, 19 (1994) 19-22.

[32] B. Yu, J.-S. Ahn, Y.-K. Lee, Measurement of translucency of tooth enamel and dentin, Acta Odontologica Scandinavica, 67 (2009) 57-64.

[33] S. Morimoto, S. Khonthon, Y. Ohishi, Optical properties of Cr^{3+} ion in lithium metasilicate $Li_2O \cdot SiO_2$ transparent glass–ceramics, J. Non-Cryst. Solids, 354 (2008) 3343-3347.

[34] S.J. Rukmani, R.K. Brow, S.T. Reis, E. Apel, V. Rheinberger, W. Höland, Effects of V and Mn Colorants on the Crystallization Behavior and Optical Properties of Ce-Doped Li-Disilicate Glass-Ceramics, J. Am. Ceram. Soc., 90 (2007) 706-711.

[35] A.R. Molla, R.P.S. Chakradhar, C.R. Kesavulu, J.L. Rao, S.K. Biswas, Microstructure, mechanical, EPR and optical properties of lithium disilicate glasses and glass–ceramics doped with Mn^{2+} ions, J. Alloys Compd., 512 (2012) 105-114.

[36] A. Gaddam, H.R. Fernandes, D.U. Tulyaganov, M.J. Pascual, J.M. Ferreira, Role of manganese on the structure, crystallization and sintering of non-stoichiometric lithium disilicate glasses, RSC Advances, 4 (2014) 13581-13592.

Chapter 2

General background

2.1 Glass and glass-ceramics

Glass is transparent non-crystalline solid obtained by continuous cooling from the liquid state. Fig. 2.1 illustrates the volume-temperature diagram for a glass-forming liquid. When a liquid or a melt cools, its volume decreases. In general, crystallization occurs at the melting T_m and a volume decrease due to higher density of crystal than that of liquid (a→b→d in Fig. 2.1). If the cooling is enough to rapid suppressing the crystallization at T_m, the volume decreases continuously along the line (a→b→c) reaching super-cooled liquid region. These super-cooled liquid is thermodynamically metastable with respect to crystalline. With further decreasing of temperature, the significant change in slope is observable in glass transformation range. Finally, the slope becomes parallel to the contraction line of crystalline form (d→c). In glass transformation region, the location of glass transition temperature T_g is determined by the cooling rate. If the cooling is fast, T_g is placed in higher temperature $(T_f)_2$ than that of the glass with slower cooling rate $(T_f)_1$, thereby the volume of the glass with fast cooling is larger than that of the glass with slower cooling rate. This is unlike transitions between thermodynamically stable phase (either first- or higher-order phase transitions). Therefore, glass transition is the

'pseudo' second-order phase transition since the value of the T_g is not defined by thermodynamics alone, but also depends on kinetic parameters (rate of cooling) [1-3].

Glass-ceramics (GCs) are ceramic materials, which is initially prepared as glasses, shaped by glass-forming techniques, and fabricated by the controlled nucleation and crystallization process. There are two type of process such as conventional forming bulk glass and power route i.e. sintering, and each process dominantly relate to the volume (bulk) crystallization and surface crystallization. Microstructure of the GCs can be designed by an adequate heat treatment and an additional additive for the nucleation and crystal growth. GCs have been shown the suitable properties for various application such as favorable thermal, chemical, biological, dielectric properties, generally superior to metals and organic polymers, and mechanical properties achieved by the fine-grained interlocking crystal morphology. [4-7].

Nucleation

Nucleation is a critical factor for controlled crystallization since the evolution of crystals in a base glass consisted of two stages with a formation of submicroscopic nuclei and their growth into macroscopic crystals [3, 8-10]. The thermodynamic driving force of the nucleation is the change in Gibbs free energy (ΔG) between the volume contribution (ΔG_v) and the surface contribution (ΔG_0) as shown in Fig. 2.2(a).

$$\Delta G = -\Delta G_V + \Delta G_0 \quad (1)$$

The volume contribution ΔG_v is the portion of energy obtained in the nucleation process, hence it becomes negative. Assuming a spherical form,

$$-\Delta G_V = -\frac{4}{3}\pi r^3 \Delta g_v \quad (2)$$

where r is the radius of the nucleus and Δg_v is the change in the free energy in transforming a unit volume of the liquid to a unit volume of the crystal. The surface contribution ΔG_0 is the energy provided when a nucleus formed, thus it becomes positive:

$$\Delta G_0 = 4\pi r^2 \sigma \quad (3)$$

where σ is surface tension. Therefore, the net change in energy, ΔG is given by Eq. (4).

$$\Delta G = -\frac{4}{3}\pi r^3 \Delta g_v + 4\pi r^2 \sigma \quad (4)$$

The critical size, $r*$, of a spherical nucleus is determined by differentiating ΔG with respect to r and setting equal to zero:

$$r^* = (\frac{2\sigma}{\Delta g_V}) \quad (5)$$

According to classical theory of homogeneous steady state crystal nucleation (i.e. time-independent), the nuclei precipitate in a homogeneous super-cooled liquid. The nucleation rate, defined as the number of nuclei formed per unit volume in unit time, is given by

$$I = I_0 \exp(-\frac{W^* + \Delta G_D}{k_B T}) \quad (6)$$

where, I_o is the pre-exponential term, W^* is the thermodynamic energy barriers for nucleation of a critical sized nucleus and ΔG_D is kinetic energy barriers for transfer of atoms through the solid-liquid interface to this nucleus i.e. activation energy for

molecular transport (or viscous flow) in the matrix phase. The I_o is expressed as the following,

$$I_0 = 2n_v V^{1/3} (\frac{kT}{h})(\frac{\sigma}{kT})^{1/2} \quad (7)$$

where n_v is the number of 'formula units' of the crystallizing component phase per unit volume of the liquid, V is the volume per formula unit, σ is the crystal-liquid interfacial free energy per unit area and h is Planck's constant. In practice, I_o varies between 10^{41} and 10^{42} m^{-3}s^{-1} for different condensed systems.

The thermodynamic barrier W^* for the formation of a stable nucleus is given by Eq. (8).

$$W^*_{homo} = \frac{16\pi}{3}(\frac{\sigma^3}{\Delta g_V^2}) \quad (8)$$

In addition, it is usually assumed that the kinetic barrier ΔG_D can be expressed by effective diffusion coefficient D as given by Eq. (9),

$$D = \frac{kT\lambda^2}{h}\exp(-\frac{\Delta G_D}{kT}) \quad (9)$$

where λ is a quantity of the order of atomic dimensions (jump distance). Using Stokes-Einstein relation in Fig. (10), D can be related to the viscosity (η) of glass.

$$D = \frac{kT}{3\pi\lambda\eta} \quad (10)$$

Meanwhile, when "foreign" surfaces are present acting as external catalysts, heterogeneous nucleation take place by the formed nuclei on preferred nucleation sites including pre-existing interfaces, previously nucleated phases, surface defects and container wall as shown in Fig. 2.2(b). Thus, heterogeneous steady-state nucleation rate is given by Eqs. (11) – (13).

$$I_{st}^{het} = N^S \frac{kT}{h} \exp\left(-\frac{W_{hetero}^* + \Delta G_D}{kT}\right) \quad (11)$$

$$\varphi = f(\theta) = \frac{1}{4}(1 - \cos\theta)^2 (2 + \cos\theta) \quad (12)$$

$$W_{hetero}^* = W_{homo}^* \varphi \qquad (13)$$

where N^S is the number of 'structural units' in contact with the catalyzing surface per unit volume and θ is the contact angle. Thus, when θ is 0° (fully wetting condition), then W_{hetero}^* becomes W_{homo}^*, and when θ is 90°, then W_{hetero}^* becomes $W_{homo}^*/2$, and when θ is 180° (fully non-wetting condition), then W_{hetero}^* is equal to W_{homo}^*.

It is noted that the above equations are valid for time-independent process. In practice, unlike in metals, an equilibrium size distribution of nuclei in glass is not obtained immediately at a given temperature due to its very high viscosity. Therefore, a steady state nucleation in glass might take a long time. The number of nuclei $N(t)$ at time is given by Eq. (14),

$$\frac{N(t)}{I\tau} = \frac{t}{\tau} - \frac{\pi^2}{6} - 2\sum_{n=1}^{\infty} \frac{(-1)^n}{n^2}]\exp\left(-\frac{n^2 t}{\tau}\right) \quad (14)$$

where τ is an induction time and n is an integer. For $t > 5\tau$, this reduces to simple linear relation as the following,

$$N(t) = I_{st}\left(t - \frac{\pi^2}{6}\tau\right) \quad (15)$$

Thus, the time lag τ can be easily estimated by using the induction period t_{ind}.

$$\tau = \frac{6}{\pi^2} t_{ind} \quad (16)$$

Crystal growth

After a nucleus with critical size is formed, crystal growth occurs by diffusion of atom from liquid to the interface. According to Turnbull [11], the mathematical description of crystal growth u is given by Eq. (17),

$$u = av\exp(-\frac{\Delta E}{kT})[(1-\exp(\frac{\Delta g_v}{kT})] \quad (17)$$

where u is crystal growth rate, a is jump distance between the two sites, v is the atomic jump frequency, ΔE is barrier height between free energy of liquid and crystal, Δg_v is the change in the free energy in transforming a unit volume of the liquid to a unit volume of the crystal. It was suggested that the activation energy for the rate of crystal growth should be the same as those that control diffusive flow, thus ΔE is replaced by the diffusion coefficient D given by Eq. (18).

$$D = a^2 v\exp(-\frac{\Delta E}{kT}) \quad (18)$$

$$u = \frac{D}{a}[(1-\exp(\frac{\Delta g_v}{kT})] \quad (19)$$

The equation for crystal growth rate is rearranged as Eq. (19). Taking into account the Stokes-Einstein relation (Eq. (10) between the diffusion coefficient and the viscosity, this equation transforms into

$$u = \frac{fkT}{3\pi a^2 \eta}[1-\exp(\frac{\Delta g_v}{kT})] \quad (20)$$

where f is the fraction of the surface area where growth sites is available.

2.2 Lithium disilicate glass-ceramics

LS2 GCs was firstly introduced by Stookey [12] in 1959. Fig. 2.3 illustrates a phase diagram of binary Li_2O-SiO_2 system. The classical nucleation theory is well agreed in Li_2O-SiO_2 system confirmed by experimental measured thermodynamic parameters [9]. Therefore, the binary Li_2O-SiO_2 system was regarded as a model system for the study of glass nucleation and crystallization mechanisms. In particular, the multicomponent Li_2O-SiO_2 system have attracted a lot of interests for dental application since the fine-grained microstructure with randomly distributed needle-shape crystal morphology imparts the excellent mechanical properties. Commercially, LS2 GCs with a high flexural strength (σ_f) of 400 ± 40 MPa and high fracture toughness (K_{IC}) of 3.3 ± 0.3 MPa·$m^{1/2}$ were firstly introduced in market as IPS Empress 2 (Ivoclar Vivadent, Lichtenstein) at 1998 [13, 14]. These material was replaced by IPS e.max Press (Ivoclar Vivadent, Lichtenstein) with an enhanced optical and mechanical properties by employing technical improvements in the production processes at 2005 [15]. With an advances in digital technology, computer-aided design/computer-aided manufacturing (CAD/CAM) technology has been applied to machining dental ceramics due to its advantages contributing to time saving with single visit compared with conventional restoration process at least 3 visits to clinic [16]. Recently, the attempts to further enhance the mechanical properties have been made to expand the application from the single crown to three-unit bridges.

2.3 Color and the optical properties of glass-ceramics

Color in glass can be achieved by addition of transition metal or rare earth elements having $3d$ or $4f$ orbitals which have specific absorption in visible wavelength. The absorption depends on the specific valence state of colorant ion and determines the appearance of characteristic color. The valence state of the colorant ion predominantly depends on the composition of the residual glassy matrix and redox reaction between colorant ions. [8, 17]. Table 2.1 summarizes the color generated by transition metal and rare-earth element in glass.

Bamford [18] described the absorption spectra of the transition elements in glass and generally explained in terms of ligand field theory (crystal field theory) or molecular orbital theory. Fig. 2.4(a) shows the free ions (no ligand field) and central metal ion in octahedral or tetrahedral complexes. When the ions are incorporated in complexes, the spectroscopic ground state of free ion is split by the surrounding electric field. For instance, transition metal ion possesses d orbital consisted of d_{xy}, d_{xz}, d_{yz}, d_{z2} and d_{x2-y2}. Fig 2.4(b) presents the of splitting of the degenerate d-orbitals due to an octahedral or tetrahedral ligand field. Since the ligands approach the metal ion along the x, y and z axes, the electron in d_{z2} and d_{x2-y2} orbitals receive greater repulsion, causing a splitting in the energy levels of the d-orbitals. The new round state locates a lower level than original grown state, $3/5\Delta$ and $2/5\Delta$ for tetrahedral and octahedral coordination, respectively. This splitting is caused by several factors such as the radii of the transition metal and ligands, and the polarizability of ligands. In addition, the stabilization energy of the octahedral coordination is generally higher than that of tetrahedral coordination [19]. Consequently, the ions prefer octahedral coordination in glass unless there are other structural limitations.

The absorption band can be identified by the using of Tanabe-sugano diagram as shown in Fig.2.5. Tanabe-Sugano diagrams is based on octahedral system [20]. It contains spin-allowed transition and spin-forbidden transition. Horizontal axis is octahedral ligand field (Δ_o) divided by Racah parameter (B). Racah parameter is a measure of the repulsion between sample multiplicity. Vertical axis is consisted of energy of excited states (E) divided by Racah parameter. Referring the Tanabe-sugano diagram, the observed absorption band can be identified and the degree of splitting in ligand field can be estimated.

In GCs, the transition metal cation or rare earth elements is expected to be placed in residual glassy matrix unless it forms solid solution in crystal. The valency of colorant ion is governed by the environment such as glass composition and oxygen pressure, which might affect redox state of colorant ion [21]. If the multiple colorant ion is added to glass at the same time, the redox reaction occurs between the colorant ions. The activity of redox ion in glass is mainly determined by the nature of redox ion, coordination number and symmetry and polarizability of the ligands associated with the redox ion [21].

Table 2.1. Colors generaged by transition metal and rare-earth elements in glass [8]

	Transition metal ions			Rare earth ions	
Configuration	Ion	Color	Configuration	Ion	Color
	Ti^{4+}	Colorless	$4f^0$	La^{3+}	None
d^0	V^{5+}	Faint yellow to colorless		Ce^{4+}	Weak yellow
	Cr^{6+}	Faint yellow to colorless	$4f^1$	Ce^{3+}	Weak yellow
	Ti^{3+}	Violet-purple	$4f^2$	Pr^{3+}	Green
d^1	V^{4+}	Blue	$4f^3$	Nd^{3+}	Violet-pink
	Mn^{6+}	Colorless	$4f^4$	Pm^{3+}	None
d^2	V^{3+}	Yellow-green	$4f^5$	Sm^{3+}	None
d^3	Cr^{3+}	Green	$4f^6$	Sm^{2+}	Green
d^4	Cr^{2+}	Faint blue		Eu^{3+}	None
	Mn^{3+}	Purple	$4f^7$	Eu^{2+}	Brown
d^5	Mn^{2+}	Light yellow		Gd^{3+}	None
	Fe^{3+}	Faint Yellow to Colorless	$4f^8$	Tb^{3+}	None
d^6	Fe^{2+}	Blue-green	$4f^9$	Dy^{3+}	None
	Co^{3+}	Faint Yellow to Colorless	$4f^{10}$	Dy^{2+}	Brown
d^7	Co^{2+}	Blue-pink		Ho^{3+}	Yellow
d^8	Ni^{2+}	Brown-purple	$4f^{11}$	Er^{3+}	Weak pink
d^9	Cu^{2+}	Blue-green	$4f^{12}$	Tm^{2+}	None
d^{10}	Cu^+	Colorless	$4f^{13}$	Yb^{3+}	None
			$4f^{14}$	Lu^{3+}	None
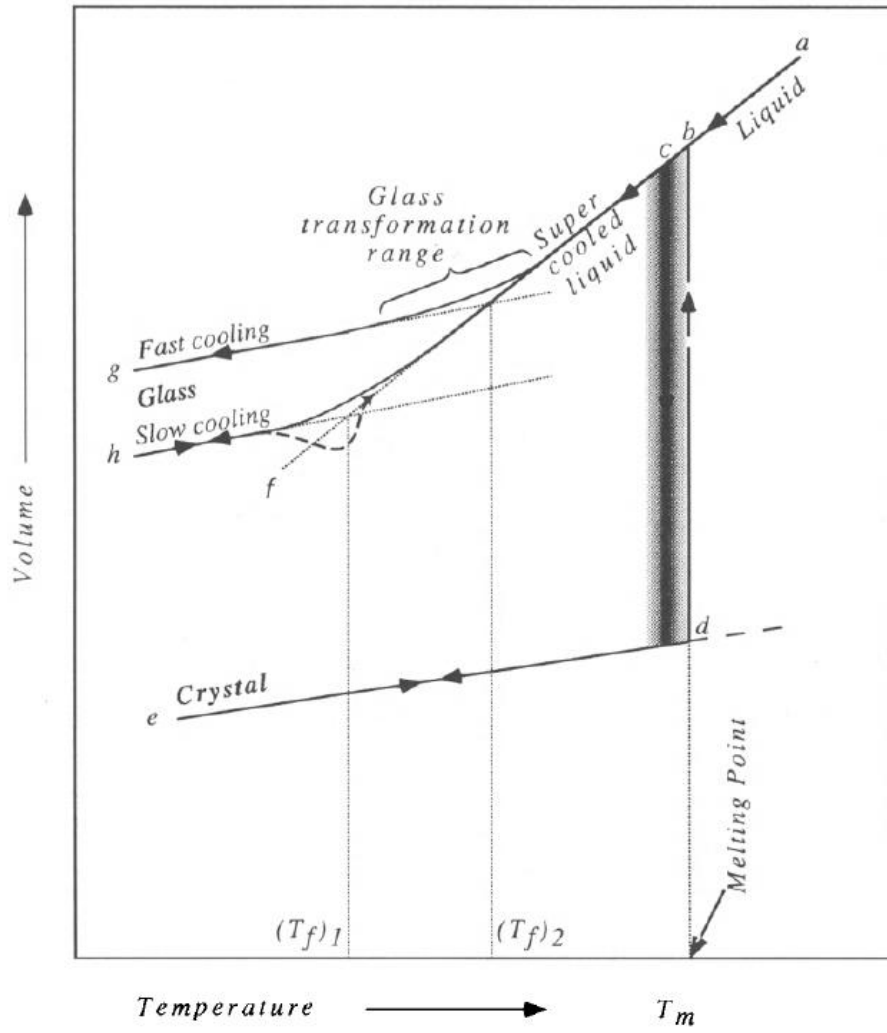
Fig. 2.1. The volume-temperature diagram for a glass-forming liquid [8].

(a)

$\Delta G_0 = 4\pi r^2 \sigma$

Free enthalpy ΔG

$+$

0

ΔG^*

r^*

Nuclear radius r

$\Delta G = -\Delta G_V + \Delta G_0$

$-$

$-\Delta G_V = \frac{4}{3}\pi r^3 \Delta g_V$

(b) Main phase

Nucleus

Contact angle θ

$\theta = 180°$

Substrate of alien nucleus
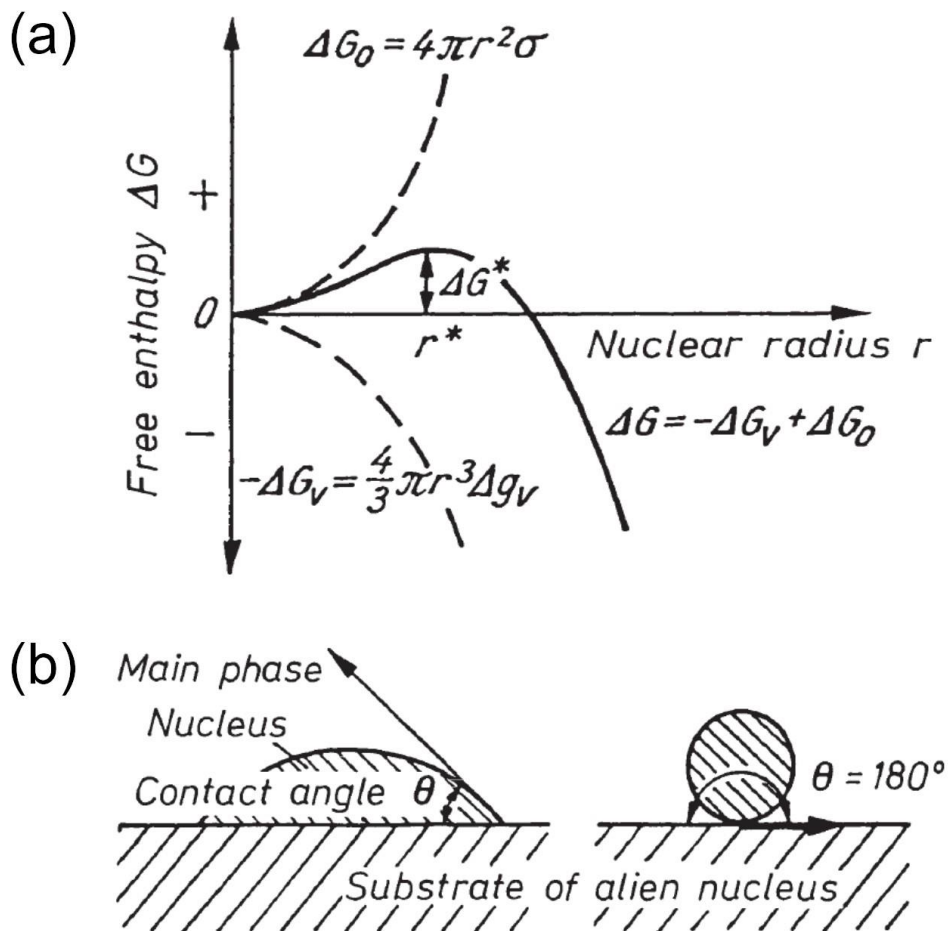
Fig. 2.2. (a) Changes in Gibbs free energy (ΔG) as function of the radius of nucleus size (r) and (b) Model for heterogeneous nucleation [10].
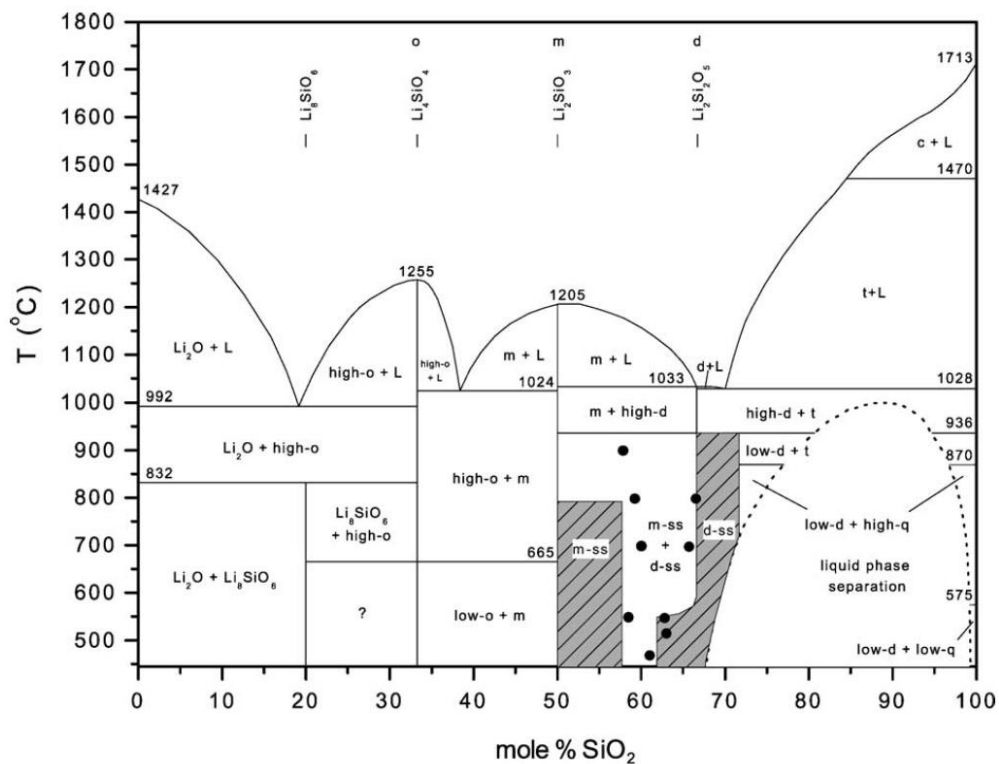
Fig. 2.3. Phase diagram of the Li_2O-SiO_2 system [22].

(a)

(b)

$d_{x^2-y^2}$ d_{z^2}

e_g

$\frac{3}{5}$ o

E

o

$\frac{2}{5}$ o

t_{2g}

d_{xy} d_{xz} d_{yz}

Octahedral

d_{xy} d_{xz} d_{yz}

t_2

$\frac{2}{5}$ t

t

$\frac{3}{5}$ t

e

$d_{x^2-y^2}$ d_{z^2}
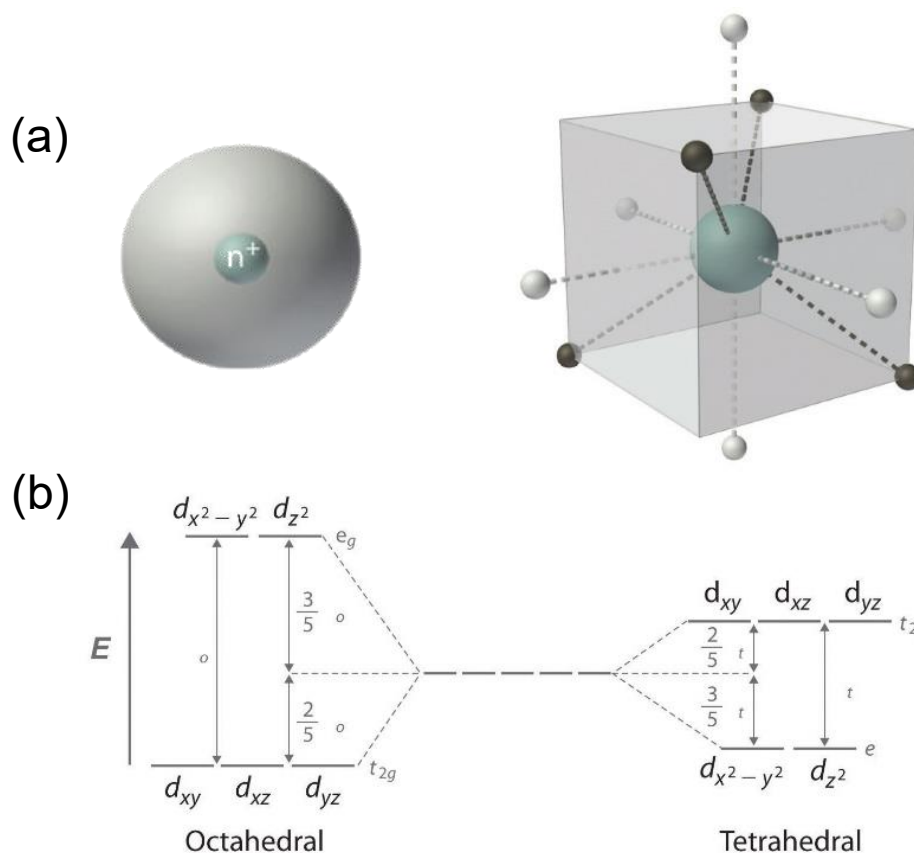
Tetrahedral

Fig. 2.4. (a) Transition metal cation (left) and central metal ion in octahedral or tetrahedral complexes (right), (b) Crystal field splitting of the degenerate d-orbitals due to an octahedral ligand field (left diagram) and the tetrahedral ligand field (right diagram) [23].
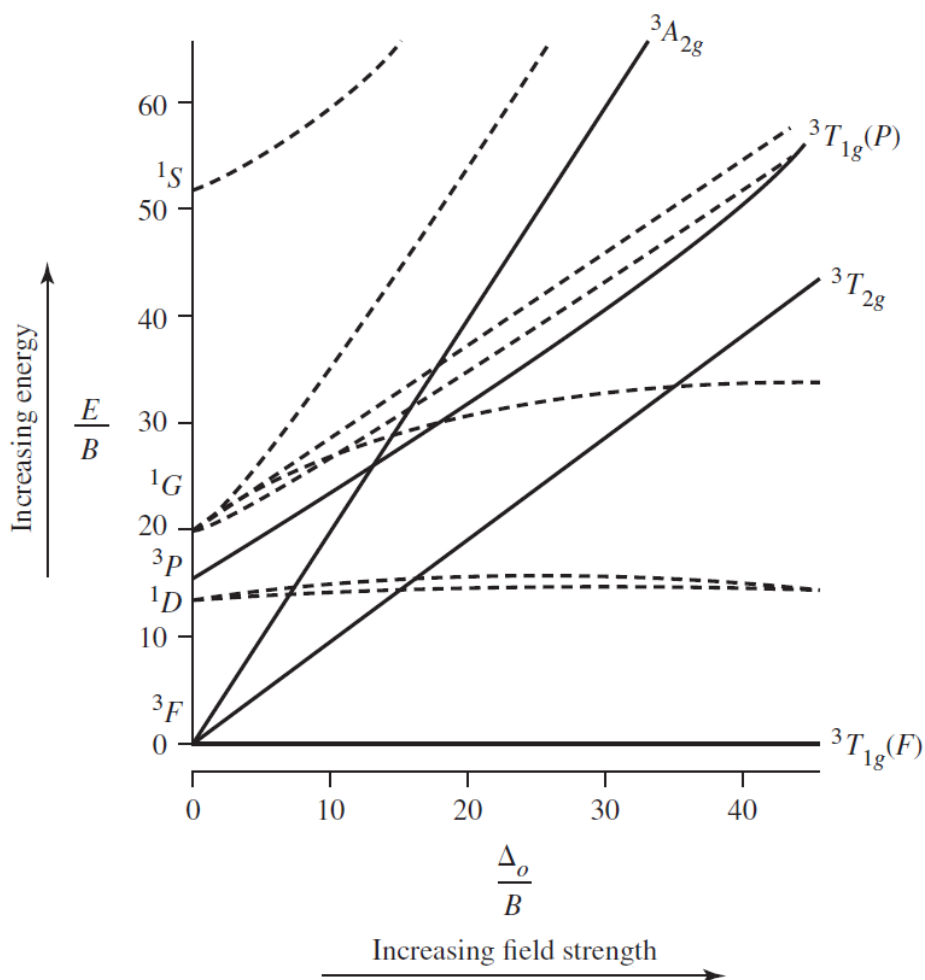
Figure 2.5. Tanabe-sugano diagram of a $3d^2$ electronic configuration in octahedral ligand field [20]. The solid line is spin-allowed transition and the dot is spin-forbidden transition

References

[1] K. Rao, Structural chemistry of glasses, Elsevier, 2002.

[2] I.S. Gutzow, O.V. Mazurin, J.W. Schmelzer, S.V. Todorova, B.B. Petroff, A.I. Priven, Glasses and the glass transition, John Wiley & Sons, 2011.

[3] R.H. Doremus, Glass science, 1994.

[4] P.W. McMillan, Glass-ceramics, 1964.

[5] W. Holand, G.H. Beall, Glass ceramic technology, 2nd ed ed., John Wiley & Sons inc., New Jersey, 2012.

[6] E. El-Meliegy, R. van Noort, Glasses and Glass Ceramics for Medical Applications, Springer Science & Business Media, 2011.

[7] H. Bach, D. Krause, Analysis of the composition and structure of glass and glass ceramics, Springer Science & Business Media, 2013.

[8] A.K. Varshneya, Fundamentals of inorganic glasses, Elsevier, 2013.

[9] P. James, M. Lewis, Glasses and glass-ceramics, Volume nucleation in silicate glasses, Chapman and Hall, London, (1989).

[10] W. Vogel, Glass chemistry, Springer Science & Business Media, 2012.

[11] D. Turnbull, Formation of crystal nuclei in liquid metals, J. Appl. Phys., 21 (1950) 1022-1028.

[12] S. Stookey, Catalyzed crystallization of glass in theory and practice, Industrial & Engineering Chemistry, 51 (1959) 805-808.

[13] M. Schweiger, W. Höland, M. Frank, H. Drescher, V. Rheinberger, IPS Empress 2: a new pressable high-strength glass-ceramic for esthetic all-ceramic restorations, Quintessence Dent Technol, 22 (1999) 143-151.

[14] W. Höland, M. Schweiger, M. Frank, V. Rheinberger, A comparis on of the microstructure and properties of the IPS Empress® 2 and th e IPS Empress® glass-ceramics, Journal of biomedical materials researc h, 53 (2000) 297-303.

[15] F. Zarone, M. Ferrari, F.G. Mangano, R. Leone, R. Sorrentino, "Digitally oriented materials": focus on lithium disilicate ceramics, Inter national journal of dentistry, 2016 (2016).

[16] J.-H. Kim, S. Oh, S.-H. Uhm, Effect of the crystallization process on the marginal and internal gaps of lithium disilicate CAD/CAM cro wns, BioMed research international, 2016 (2016).

[17] W.A. Weyl, Coloured glasses, in: Part of a collection of researc h on crystalline glazes donated (c. 1990) to CSAD by CI Brown. See Shelf 8, Boxes 5, 6, 7, Society of glass technology, 1981.

[18] C. Bamfort, Control of Colour and Generation in Glass, in, Elsevi er-North Holland Publication, Amsterdam, 1977.

[19] A.M. Nassar, N. Ghoneim, Vanadium contribution in different gla sses in view of the ligand field theory, J. Non-Cryst. Solids, 46 (1981) 181-195.

[20] G.O. Spessard, G.L. Miessler, Inorganic chemistry, 2009.

[21] A. Paul, Chemistry of glasses, Springer Science & Business Medi a, 1990.

[22] P.C. Soares, E.D. Zanotto, V.M. Fokin, H. Jain, TEM and XRD study of early crystallization of lithium disilicate glasses, J. Non-Cryst. Solids, 331 (2003) 217-227.

[23] R.J. Lancashire, A. Awan, H. Truong, Crystal Field Theory, https://chem.libretexts.org/Bookshelves/Inorganic_Chemistry/Modules_and_ Websites_(Inorganic_Chemistry)/Crystal_Field_Theory/Crystal_Field_Theo ry

Chapter 3

Crystallization sequence and microstructure for the SiO$_2$-Li$_2$O-P$_2$O$_5$-K$_2$O-ZnO system

3.1 Introduction

Various additives have been employed for the dental applications of LS2 GCs to control their microstructures during crystallization and finally to obtain appropriate optical and mechanical properties. The additives are generally classified into three different types of nucleating agent, glass modifier and glass intermediate, where the nucleating agents include TiO_2, ZrO_2, and P_2O_5, typical glass modifiers are composed of Na_2O and K_2O, and glass intermediates consist of Al_2O_3, B_2O_3, ZnO, CaO, MgO, and BaO [1-3]. As previously reported by many researchers [4-7], the representative nucleating agent for LS2 GCs is P_2O_5 which is well-known to promote the nucleation rate as a heterogeneous nucleation center, resulting in a fine-grained microstructure of interlocked LS2 phase. In general, the glass modifiers are added to promote the atomic diffusion for crystal growth and also to control the chemical stability of a residual glassy phase after crystallization. For instance, if alkali oxides such as K_2O are added as glass modifiers, the viscosity of a glass can be decreased and thus its viscous flow can be increased so that a residual stress in GCs, induced by an abrupt density change due to crystallization in the glass matrix, can be released [7]. On the other hand, glass intermediates such as Al_2O_3 and ZnO are known to

28

improve the chemical stability of residual glassy phase and also affect optical translucency and mechanical properties of GCs [8, 9].

In this chapter, the K_2O glass modifier and ZnO glass intermediate were selected in addition to the nucleating agent P_2O_5 since K_2O favors the LS crystallization and ZnO is known to induce amorphous phase separation and also impart the chemical durability in a residual glassy phase [7]. Previous studies on the SiO_2-Li_2O-ZnO-K_2O-P_2O_5 system [5, 8, 10] were conducted by increasing the amount of P_2O_5-K_2O-ZnO additives relative to the amount of the Li_2O-SiO_2 matrix. However, this approach seems to be very limited for understanding the crystallization sequence of LS and LS2 because the relative amount of the Li_2O-SiO_2 matrix is consistently varied. Thus, while the amount of the P_2O_5 nucleating agent relative to that of the Li_2O-SiO_2 matrix was fixed to have 1.5 mol%, the mixing ratios of ZnO/K_2O (Z/K) between ZnO and K_2O glass modifiers were varied from 0 to 3.5 in order to investigate their effects on the crystallization sequence and the microstructure of LS2 GCs. All samples were prepared by two-stage heat treatments composed of a nucleation stage and a growth stage, which is the conventional method for producing fine-grained GCs.

3.2 Experimental

The precursors were SiO_2 (99%, Daejung Chemical Co., Ltd, Korea), Li_2CO_3 (98%, Daejung Chemical Co., Ltd, Korea), $(NH_4)_2HPO_4$ (98.5%, Daejung,Korea), K_2CO_3 (99%, Kojundo Chemical Lab. Co., Ltd, Japan), and ZnO (99%, Kojundo

Chapter 3: Crystallization sequence and microstructure for the SiO₂-Li₂O-P₂O₅-K₂O-ZnO system

Chemical Lab. Co., Ltd, Japan). The molar ratio of SiO_2 to Li_2O in the LS2 matrix was 2.39:1. The total amount of additives relative to the Li_2O-SiO_2 matrix was fixed to have 6 mol%, The nominal compositions of samples are listed in Table 3.1. The precursors were weighed, mixed by 3D-mixer (Korea machine engineering, KMC-T2, Korea) for 30 min, put into a Pt crucible, and melted at 1400°C for 2 h in air in an elevator furnace. The melts were poured into a stainless crusher to make a frit. The frit was re-melted under the same conditions for a homogenization of glass. The re-melted glasses were cast into a cylindrical graphite mold with the diameter of 13 mm and the height of 20 mm, and subsequently annealed at 450°C for 30 min in air to remove a residual stress induced during cooling. The crystallization behavior was observed by differential scanning calorimetry (DSC, SDT Q600, TA instruments, USA). The glass particle of ~ 50 mg (>500 μm,) was used to prevent a surface crystallization, and heated to 1100°C in a Pt cell with the heating rate of 10°C /min.

The glass block samples were nucleated at 500°C for 1 h in air with the heating rate of 10°C/min, and subsequently raised up to 600°C, 700°C, and 800°C for crystallization with the heating rate of 30°C/min for 2 h. For microstructural observation, crystallized samples were polished and etched with a 15 vol% HF solution for 5 – 20 sec. The morphologies of the crystalline phases were observed by field emission scanning electron microscopy (FE-SEM, JSM6701F, Jeol, Japan). X-ray diffraction (XRD, D/max 2500, Rigaku, Japan) was carried out to identify the crystalline phases of crystallized samples with Cu Kα (λ=1.5401Å) radiation produced at 40 kV and 100 mA. The diffraction pattern was scanned from 10° to 80° with the step size of 0.02° and the scan speed of 5°/min.

Chapter 3: Crystallization sequence and microstructure for the SiO$_2$-Li$_2$O-P$_2$O$_5$-K$_2$O-ZnO system

The crystallization sequence was analyzed by High-temperature X-ray diffraction (HT-XRD, D/max 2500, Rigaku, Japan) with Cu Kα (λ=1.5401 Å) radiation produced at 40 kV and 200 mA. The monolithic glass samples with the dimension of 1.6 mm × 12 mm × 19 mm were initially heated to 460°C with the heating rate 20°C/min and maintained for 5 min. XRD analyses were performed at temperature ranging from 460 to 600°C in steps of 20°C and 600 to 900°C in steps of 25°C with 2θ scan from 10 to 50° and scan speed of 2°/min.

3.3 Results

3.3.1 Crystallization behavior

The DSC curves obtained from all glass samples with the heating rate of 10°C/min are shown in Fig. 3.1. For a comparison, we also performed the DSC analysis for the glass sample with only ZnO-P$_2$O$_5$ additives (i.e., without K$_2$O) of which sample ID is Z4.5. Several exothermic peaks and one endothermic peak are observable in Fig. 3.1. Their characteristic temperatures analyzed by DSC are listed in Table 3.2, where T$_x$, T$_p^{-1}$ and δT$_p$ are onset temperature, inverse temperature and height of exothermic peak, respectively. The samples of K4.5, Z/K0.35 and Z/K0.5 represent three different exothermic peaks. With increasing the Z/K ratio, the first and third exothermic peaks shift to lower temperatures while the second exothermic peak moved to higher temperature. In addition, with increasing the Z/K ratio, while the first exothermic peak height increases, the third peak height decreases. The third peak finally disappears in

the sample of Z/K2, and hence only two exothermic peaks are observed in the Z/K2, Z/K3.5 and Z4.5 samples.

3.3.2 Crystallization sequence

To confirm the thermal events responsible for the exothermic peaks of DSC curves, and also to ensure the crystallization sequence in detail, *in-situ* HT-XRD analyses were performed for the samples of K4.5, Z/K0.5, Z/K1, Z/K 2 and Z4.5. The HT-XRD patterns obtained at various heat-treatment temperatures ranging from 460 to 900ºC are illustrated in Fig. 3.2, where the color bars display the intensities of diffraction patterns. Here, it should be noticed that, at the early crystallization stage, the peak intensities of the LS phase for the sample K4.5 in Fig. 3.2(a) exhibits the highest values compared with those of samples having the Zn/K ratio higher than K4.5 shown in Figs. 3.2(b)-(d). The cristobalite phase crystallizes at the lowest temperature in the sample K4.5 compared with the samples having higher Zn/K ratios. On the other hand, the peak intensities of the LS2 phase in the early crystallization stage and crystallization temperature of cristobalite are increased with increasing the Z/K ratio. Interestingly, as shown in Fig. 3.2(d), at the early crystallization stage of the sample Z/K2, while the intensities of (111) main peak and (200) second peak for the LS phase are degraded, the third peak of (310) becomes the main peak. Finally, the peak near at 33º, most probably the LS peak of (310), is clearly observed until 850ºC and subsequently disappears in the sample Z4.5, which will be further discussed later.

Chapter 3: Crystallization sequence and microstructure for the SiO₂-Li₂O-P₂O₅-K₂O-ZnO system

Referring to the HT-XRD patterns in Fig. 3.2, the DSC exothermic peaks could be identified. The first exothermic peak of K4.5 sample is attributed to a crystallization of the LS phase and those of Z/K0.5, Z/K1 and Z/K2 samples are due to a simultaneous crystallization of LS and LS2 phases although the peak intensities of the LS phase at (111) and (200) are continuously lowered with increasing the Z/K ratio. The second exothermic peak of K4.5 sample is obviously due to the crystallization of cristobalite since the diffraction peaks at 21.5º in Fig. 3.2(b)-(d) move to the higher temperatures with increasing the Z/K ratio, which corresponds to the peak shift of second exothermic peak to higher temperature in DSC curves in Fig. 3.1. Finally, the third exothermic peak is considered to originate from the development of the LS2 crystalline phase by reaction between LS and cristobalite because K4.5 sample clearly shows the reaction of LS with crisotbalite, which is also supported by the fact that, with increasing the Z/K ratio, the third exothermic peak shifts to lower temperature and its maximum height decreases.

3.3.3 Phase analysis

Fig. 3.3 represents the XRD patterns of samples crystallized by two-stage heat treatments at 500ºC for 1 h, and subsequently at 600ºC, 700ºC, 800ºC and 850ºC for 2 h in air. The sample K4.5 is composed of the LS primarily phase with a small peak of the LS2 phase at 600ºC as shown in Fig. 3.3(a). Fig. 3.3(a) also shows that the cristobalite phase is observed in addition to LS and LS2 phases at 700ºC, and the LS2 primary phase with a small peak of the LP phase are detectable at 800ºC and 850ºC, implying that the LS2 phase becomes primary one due to a solid state reaction

between LS and cristobalite. The crystallization exothermic peak of the LP phase may be undetectable because its amount is very small.

In the sample Z/K0.3, a small amount of LS2 phase is detected at 600 °C together with the LS phase. At 700°C, however, the LS phase disappears, and only the LS2 phase exists without the formation of cristobalite as shown in Fig. 3.3(b). Therefore, the samples heat-treated above 700°C consist of the LS2 and LP phases. For the samples from Z/K0.5 to Z/K3.5 heat-treated at 600°C, the XRD peak intensities of the LS2 phase gradually increased with increasing the Z/K ratio compared with those of the LS phase. In Fig. 3.3(c) for the sample of Z/K0.5, one can see that the cristobalite appears at 700°C and 800°C but disappears at 850°C. On the other hand, the cristobalite survives at 800°C and enhances at 850°C for the samples with higher Z/K ratio up to Z/K3.5 in Figs. 3(d)-(f). However, the unknown phase is detectable in the sample of Z4.5 at 600°C as shown in Fig. 3(e) with arrow symbol, and it disappears at 800°C.

3.3.4 Microstructure

Fig. 3.4 shows the microstructures of the samples crystallized by two-stage heat treatments at 500°C for 1 h as the nucleation stage and at 800°C for 2 h as the crystal growth stage. Since the LP phase might be resolved by HF solution, and only LS2 and cristobalite phases could be observed in the microstructure. The sample K4.5 shows an acicular crystalline phase having the long-length dimension of ~3 μm. The aspect ratio of acicular phase is decreased with increasing the Z/K ratio, and its

average size is also decreased, resulting in the fine-grained structure of ~100 nm in the sample Z4.5, indicating that the higher Z/K ratio causes the higher nucleation rate. This is also observed in other report [11].

3.4 Discussion

3.4.1 Crystallization sequence

As previously described, the Z/K ratio dramatically affects the temperature of DSC exothermic peak, crystallized phase and the microstructure in two-stage heat treatments. To understand this effect of Z/K ratio, the crystallization sequences were analyzed and compared with each other.

According to previous reports [8, 12-14], the reaction sequence in our LS2 GCs can be expressed as the following.

$$\mathrm{Li_2O\,(glass)} + 2Q^3\mathrm{(glass)} \rightarrow \mathrm{Li_2Si_2O_5\,(cryst.)} \qquad (1)$$
$$\mathrm{Li_2O\,(glass)} + Q^3\mathrm{(glass)} \rightarrow \mathrm{Li_2SiO_3(cryst.)} + Q^4\mathrm{(glass)} \qquad (2)$$
$$\mathrm{Li_2SiO_3\,(cryst.)} + Q^4\mathrm{(glass)} \rightarrow \mathrm{Li_2Si_2O_5\,(cryst.)} \qquad (3)$$
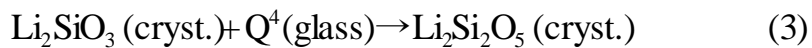
Huang *et al.* [15-17] suggested that the crystallization sequence can be classified into three different types. In type I, a simultaneous nucleation of both metastable LS and stable LS2 phases occurs at lower temperature, and LS is transformed into LS2 at higher temperature. In type II, only the LS nucleates and transforms into LS2. Whereas, in type III, stable nucleation and growth of LS2 occur without forming

metastable LS. While the crystallization sequences of type I and II were reported for the SiO$_2$–Li$_2$O–P$_2$O$_5$–Al$_2$O$_3$–K$_2$O–(ZrO$_2$) system by Bischoff *et al.* [18] and for the SiO$_2$-Li$_2$O-Al$_2$O$_3$-P$_2$O$_5$-ZrO$_2$ system by Huang *et al.* [19] the crystallization sequence of type II was reported for the SiO$_2$-Li$_2$O-MgO-Al$_2$O$_3$-P$_2$O$_5$-ZrO$_2$ system also by Huang *et* al. [16, 20]. Unlike the reaction sequence of type II by Eqs. (1) – (3), in our study, the crystallization sequence observed in the sample K4.5 can be interpreted as another type II (LS) by the Eq. (2) and the following Eqs. (4) and (5).

$$Q^4(\text{glass}) \rightarrow \text{cristobatle (cryst.)} \qquad\qquad (4)$$
$$Li_2SiO_3(\text{cryst.}) + \text{cristobalite (cryst.)} \rightarrow Li_2Si_2O_5(\text{cryst.}) \quad (5)$$
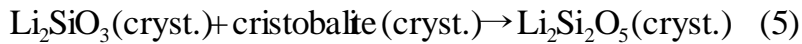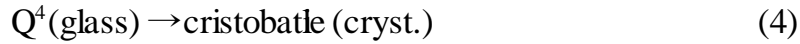
The glass phase remained after crystallization of the LS phase was crystallized to the cristobalite phase as given by Eq. (4). Thus, the solid state reaction is considered to occur between LS and cristobalite phases to form the LS2 phase as expressed by Eq. (5). This is in good agreement with the previous reports for the SiO$_2$-Li$_2$O-ZnO-P$_2$O$_5$-K$_2$O system by Clausbruch *et al.* [5, 8] and for the SiO$_2$-Li$_2$O-Al$_2$O$_3$-P$_2$O$_5$-ZrO$_2$ system by Huang et al. [12], showing that the peak intensity of the LS2 phase considerably increases while those of cristobalite and LS are disappeared. The development of the LS2 phase by reaction between LS phase and amorphous or crystalline silica phase seems to depend on the glass composition. On the other hand, the samples Z/K0.5, Z/K1 and Z/K2 can be interpreted by another type I (LS+LS2) as given by Eqs. (1), (2), (4) and (5). As a previously mentioned, the K$_2$O favors the LS crystallization by disproportionation of glass structure forming Q^2 and Q^4, therefore, the higher Z/K ratio suppresses the formation of LS phase and promotes LS2 phase in early crystallization stage because the amount of K$^+$ ion is lowered so

that the disproportionation of glass network inducing the crystallization of LS phase is decreased.

The variation of crystallization sequence from type II in the sample of K4.5 to type I in the samples of Z/K0.5, Z/K1 and Z/K2 is closely related to the nucleation rates of LS and LS2 phases. According to previous reports on determining the nucleation rate of LS2 by DSC analyses for Li$_2$O-SiO$_2$ [21-24], where only one exothermic peak was observed at ~600°C, the maximum height of the exothermic peak, δT_p is proportional to the total number of nuclei, and the inverse temperature of exothermic peak, T_p^{-1} is proportional to the density of nuclei. In the sample K4.5 with crystallization sequence type II, the peak height, δT_p and inverse temperature, T_p^{-1} of the first exothermic peak due to the crystallization of the LS phase are the lowest compared with samples with higher Z/K ratio, indicating the lowest total number of nuclei and the lowest density of nuclei. On the other hand, with the increasing the Z/K ratio, both δT_p and T_p^{-1} of the first exothermic peak are increased, which is attributable to an enhanced crystallization of the LS2 phase. The enhanced crystallization of the LS2 phase at the early crystallization stage with increasing the Z/K ratio is also evidenced by the HT-XRD patterns in Fig. 3.2. As mentioned it previously, the reduction in the LS phase peak intensity implied the enhanced crystallization of the LS2 phase. In addition, Zn is known to cause the amorphous phase separation [25] which can promote the nucleation rate by the enhancement of surface energy in vicinity of boundaries. Thus, it can be concluded that the nucleation of LS2 phase was enhanced with increasing the Z/K ratio because of crystallization sequence change from type II to type I and also increased amorphous phase separation with increasing the Zn content.

Chapter 3: Crystallization sequence and microstructure for the SiO₂-Li₂O-P₂O₅-K₂O-ZnO system

3.4.2 Solid solution of Zn²⁺ in LS2 and LS phases

To explain the peculiar behavior of diffraction peak degradation of the LS phase in HT-XRD patterns with increasing the Z/K ratio, the HT-XRD patterns of all samples at high temperatures ranging from 580 °C to 725°C, where the evolution of LS diffraction peak is clearly observed, are displayed in Fig. 3.5(a). Not only the deteriorated diffraction peak of the LS phase is detectable but also the peak shift is pronounced with increasing the Z/K ratio, showing that the second peak of (200) and third peak of (310) move to higher diffraction angles, whereas the fourth peak of (002) shifts to lower diffraction angle. The calculated lattice parameters and cell volumes of the LS and LS2 phases of samples are shown in Figs. 3.5(b) and (c). With increasing the Z/K ratio, the a and b lattice parameters of the LS phase are decreased but c lattice parameter is increased so that the unit cell volume is finally reduced. On the other hand, in the LS2 phase, all a, b and c lattice parameters are decreased, and consequently the unit cell volume is reduced.

The crystal structure of the LS phase consists of the $[SiO_4]$ single unit forming chain silicate, and chain silicates are connected by the Li^+ ion tetrahedra while that of the LS2 phase is composed of the $[Si_2O_5]^{2-}$ units forming layer-like structure which are connected by the Li^+ ion tetrahedra [26]. With increasing the Z/K ratio, the lattice parameters of LS and LS2 phases are predominantly changed, and their unit cell volumes are reduced as shown in Figs. 3.7(a) and (b), implying that a solid solution might be formed in both LS and LS2 phases by the substitution of Zn^{2+} for the Li^+ site since the ionic size of Zn^{2+} (0.6 Å) is similar to Li^+ (0.59 Å) [27] although this possibility of the solid solution formation requires further study for obtaining a

direct evidence. The substitution may be possible with the formation of cation vacancies to maintain the electrical charge neutrality as expressed by the following Eq. (6).

$$2\text{Li}^+ \rightarrow \text{Zn}^{2+} + \text{V}_c \qquad (6)$$
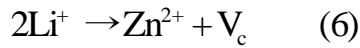
Therefore, the unit cell volume can be reduced by the substitution of Zn^{2+} for the Li$^+$ site because of a simultaneous formation of cation vacancies.

In addition, the incorporation of K$^+$ into LS and LS2 phases is impossible due to its larger ionic size of 1.37 Å. Therefore, the higher Z/K ratio might cause the Zn-substituted LS and LS2 phases, resulting in a significant change in their crystal structures. If other types of glass modifiers with larger ionic size are added instead of Zn^{2+} ion, it would not be included into the crystal structure. Instead, it may exist in residual glassy phase affecting the crystal growth rate only.

3.4.3 Effect of crystallization sequence on microstructure

The crystallization sequence affects the microstructure of glass-ceramics severely. The reason of acicular crystalline phase observed at the sample K4.5 in Fig. 3.4(a) is attributed to the crystallization sequence type II. In type II, the LS phase forms earlier than the LS2 phase, followed by precipitation of cristobalite, and finally the LS phase reacts with cristobalite at high temperature (> 700°C) with high growth rate to form the LS2 phase, as described by Eq. (5). According to the DSC analysis

Chapter 3: Crystallization sequence and microstructure for the SiO₂-Li₂O-P₂O₅-K₂O-ZnO system

results, the nuclei density of the K4.5 sample is relatively lower than those of sample with higher Z/K ratios, implying that a small amount of LS nuclei might be formed. This relatively small amount of LS nuclei grew at low temperature near to 600°C, and reacted with the cristobalite phase crystallized at higher temperature nearly 700°C, and consequently resulted in the LS2 phase with a large aspect ratio. However, the aspect ratio of LS2 phase decreased with increasing the Z/K ratio because of the enhancement of nucleation of LS2 phase in early crystallization. Furthermore, the formation of the cristobalite phase might hinder the crystal growth of the LS2 phase, resulting in a low aspect ratio of the LS2 crystalline phase.

Meanwhile, Clausbruch *et al.* [8] reported the effect of ZnO on the microstructure of glass-ceramics for a system which was similar to our system in the point that the amount of P_2O_5 was fixed to have 1.5 mol% but different from ours in the point that the amount of the SiO_2-Li_2O glassy matrix was consistently decreased with increasing the ZnO additive. In contrast to our results, from the sample containing ZnO 0 to 5 mol%, the crystallization sequence changed from type I to II. (in this study, the crystallization sequence type changed from II to I in the samples with ZnO 0 to 4.5 mol%). This opposite trend of crystallization sequence is tentatively attributed to decrease of the SiO_2-Li_2O glassy matrix with increasing the ZnO additive. They obtained the microstructure by single stage heat-treatment at the temperature region of 860 - 900°C for 30 min and it was not significantly changed. They concluded that different phase formation of the samples in the lower temperature, i.e. crystallization sequence had a negligible effect on the average size and shape of final LS2 main crystalline phases. However, since we carried out the two-step heat-treatments for nucleation and growth in this study while they

performed crystallization via single stage heat-treatment, and hence the holding at nucleation stage is believed to cause a significant difference in the size and shape of final LS2 primary crystalline phases.

3.5 Summary

With increasing the Z/K ratio, the crystallization sequence changed from type II (LS) in the sample of K4.5 to type I (LS+LS2) in other samples including Zn^{2+} ion because K$^+$ ion, which assist the LS crystallization by the disproportionation of glass network, was lowered in its amount. Because of the crystallization sequence change from type II to type I in addition to an increased amorphous phase separation of base glass, the nucleation rate of LS2 phase was enhanced with increasing the Z/K ratio, which led to a decrease in average LS2 crystalline size. The nucleation rate of LP phase was increased by increased amorphous phase separation with increasing the Zn content. The aspect ratios of the LS2 crystallites were decreased with increasing the Z/K ratio due to a decrease in its growth rate. In addition, the Zn^{2+} ion is soluble in LS and LS2 crystalline phases since its ionic radius is similar to Li$^+$ ion, resulting in the contraction of their unit cell volumes by the formation of vacancy at the Li$^+$ ion site. In conclusion, it is crucial to control the relative ratio of the additive components for engineering the microstructure of GCs, ranging from fine equiaxed LS2 crystalline phase, suitable for the enhancement of mechanical strength, to large acicular-shaped one with high aspect ratio, favorable for the improvement of fracture toughness.

Chapter 3: Crystallization sequence and microstructure for the SiO₂-Li₂O-P₂O₅-K₂O-ZnO system

Table 3.1. Compositions of the glass samples (in mol%).

Sample ID	SiO$_2$	Li$_2$O	P$_2$O$_5$	K$_2$O	ZnO
K4.5	66.27	27.73	1.5	4.5	0
Z/K0.35	"	"	"	3.5	1
Z/K0.5	"	"	"	3	1.5
Z/K1	"	"	"	2.25	2.25
Z/K2	"	"	"	1.5	3
Z/K3.5	"	"	"	1	3.5
Z4.5	"	"	"	0	4.5

Table 3.2. Characteristic temperatures of the glass samples analyzed by DSC with the heating rate of 10ºC/min, where T_g, T_x, T_p^{-1} and δT_p, T_m are glass transition temperature, onset temperature, inverse temperature, height of exothermic peak and melting temperature, respectively.

Sample ID		1st exothermic peak			2nd exothermic peak			3rd exothermic peak			
	T_g (ºC)	T_{x1} (ºC)	T_{p1}^{-1} ($\times 10^{-3}$, /ºC)	δT_{p1} (W/g)	T_{x2} (ºC)	T_{p2}^{-1} ($\times 10^{-3}$, /ºC)	δT_{p2} (W/g)	T_{x3} (ºC)	T_{p3}^{-1} ($\times 10^{-3}$, /ºC)	δT_{p3} (W/g)	T_m (ºC)
K4.5	464.9	587.0	1.62	0.34	671.2	1.46	0.15	760.8	1.29	0.21	955.1
Z/K0.35	465.3	584.9	1.63	0.58	675.2	1.47	0.21	733.1	1.34	0.15	964.9
Z/K0.5	465.4	583.3	1.65	0.70	682.0	1.45	0.17	724.4	1.35	0.07	982.2
Z/K1	465.4	577.7	1.68	1.02	693.1	1.42	0.14	-	-	-	988.0
Z/K2	465.6	583.1	1.67	1.53	722.2	1.37	0.26	-	-	-	993.3
Z/K3.5	463.5	571.4	1.71	1.79	739.0	1.34	0.17	-	-	-	986.9
Z4.5	455.4	565.6	1.74	3.3	875.7	1.13	0.27				990.7
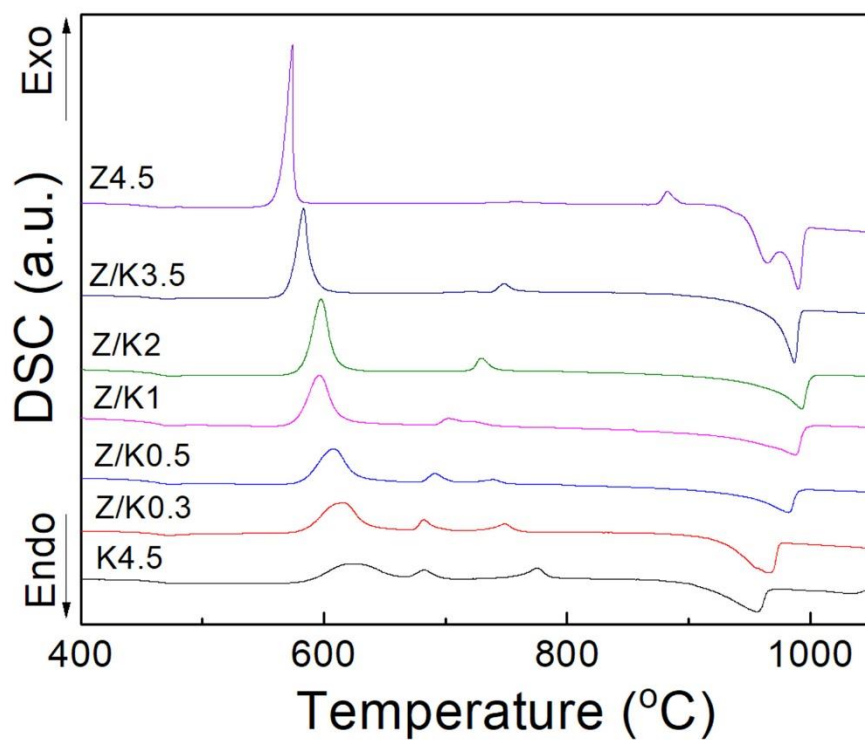
Fig. 3.1. DSC curves of the glass samples with the heating rate of 10ºC/min in air.
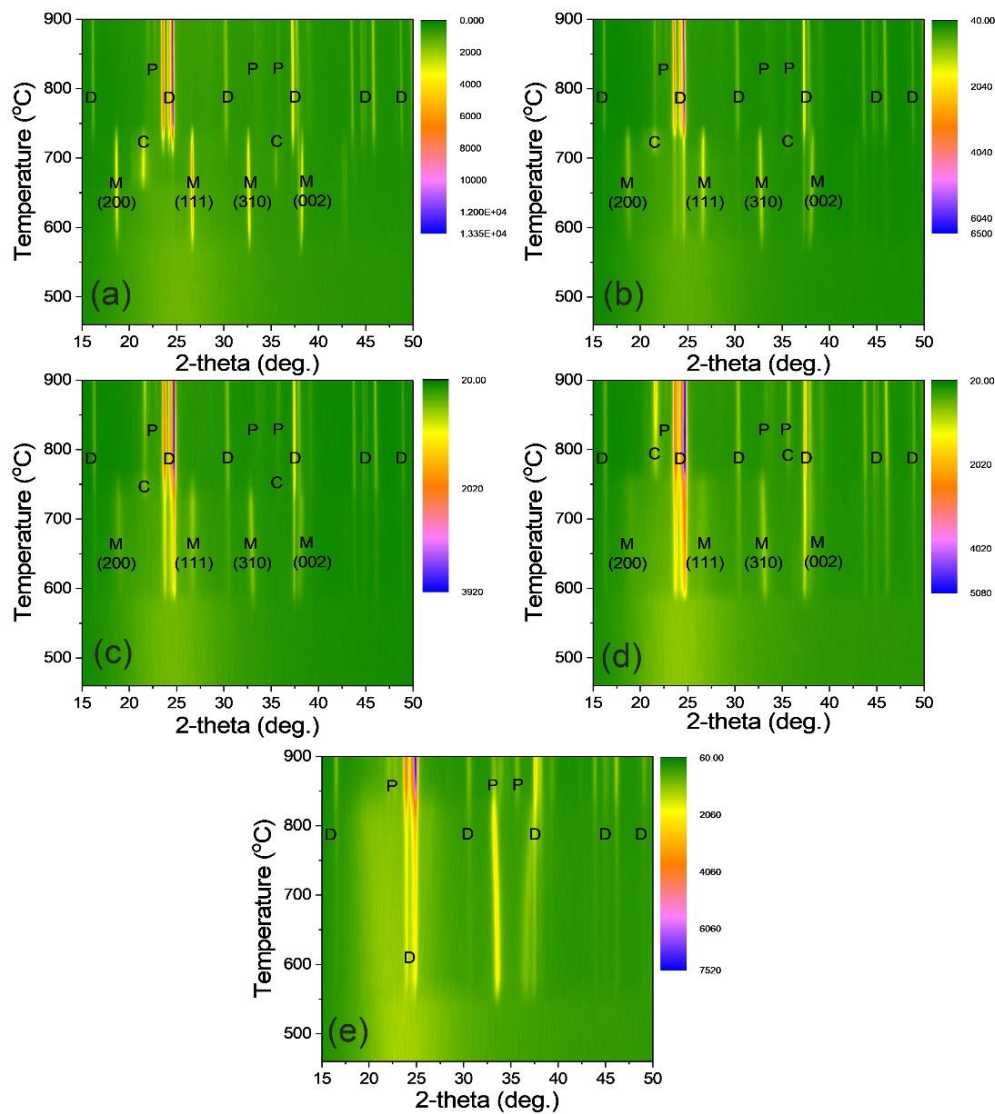
Fig. 3.2. High-temperature XRD patterns for the samples of (a) K4.5, (b) Z/K0.5, (c) Z/K1, (d) Z/K 2, and (e) Z4.5 where D, M, C, and P denote LS2, LS, cristobalite and LP, respectively.
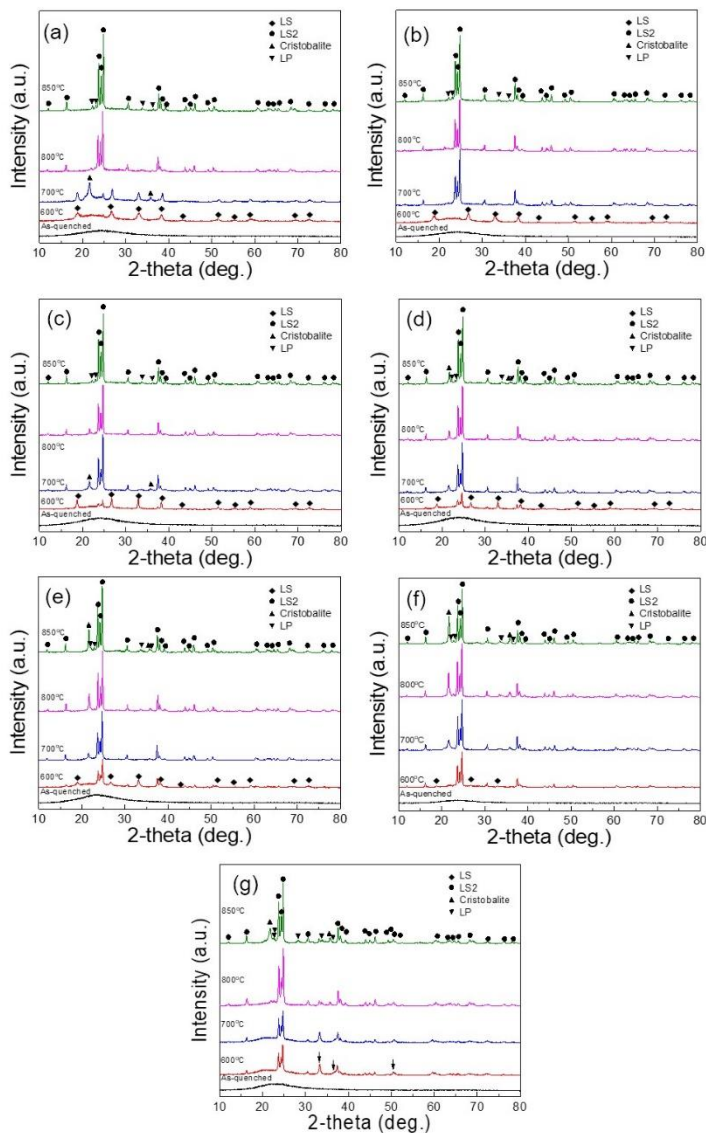
Fig. 3.3. The XRD patterns of the samples of (a) K4.5, (b) Z/K0.35, (c) Z/K0.5, (d) Z/K1, (e) Z/K2, (f) Z/K3.5 and (g) Z4.5 All samples were nucleated at 500 ℃ for 1 h and subsequently heat-treated at 600℃, 700℃, 800℃ and 850℃ for 2 h in air. (●: LS2, ◆: LS, ▼: LP, ▲: cristobalite,↓: unknown, ICDD PDF number of references: LS2 [04-010-3965], LS [04-008-3005], LP [04-015-2197], β-cristobalite [00-039-1425])

Chapter 3: Crystallization sequence and microstructure for the SiO$_2$-Li$_2$O-P$_2$O$_5$-K$_2$O-ZnO system
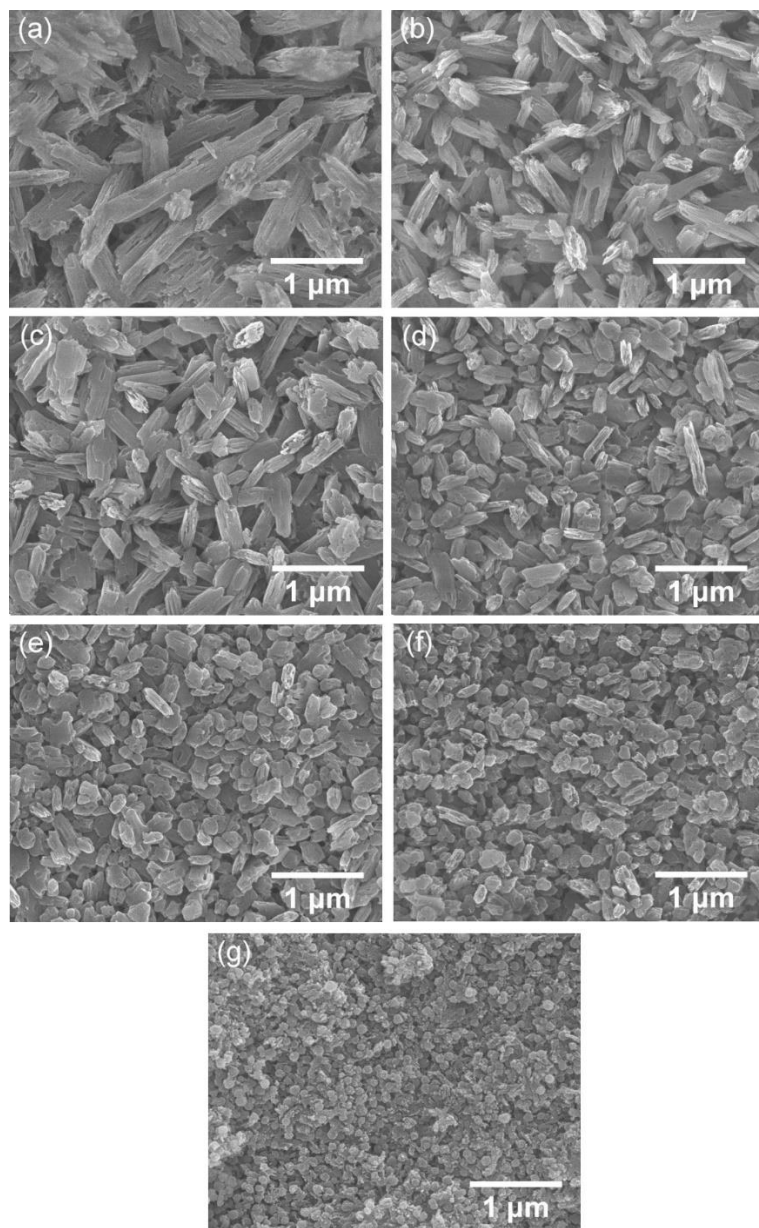
Fig. 3.4. Microstructures of samples (a) K4.5, (b) Z/K0.3, (c) Z/K0.5, (d) Z/K1, (e) Z/K2, (f) Z/K3.5 and (g) Z4.5. All samples were nucleated at 500 ℃ for 1 h and subsequently grown at 800 ℃ for 2 h. Sample surface was etched by HF 15 vol% for 10~30 sec.
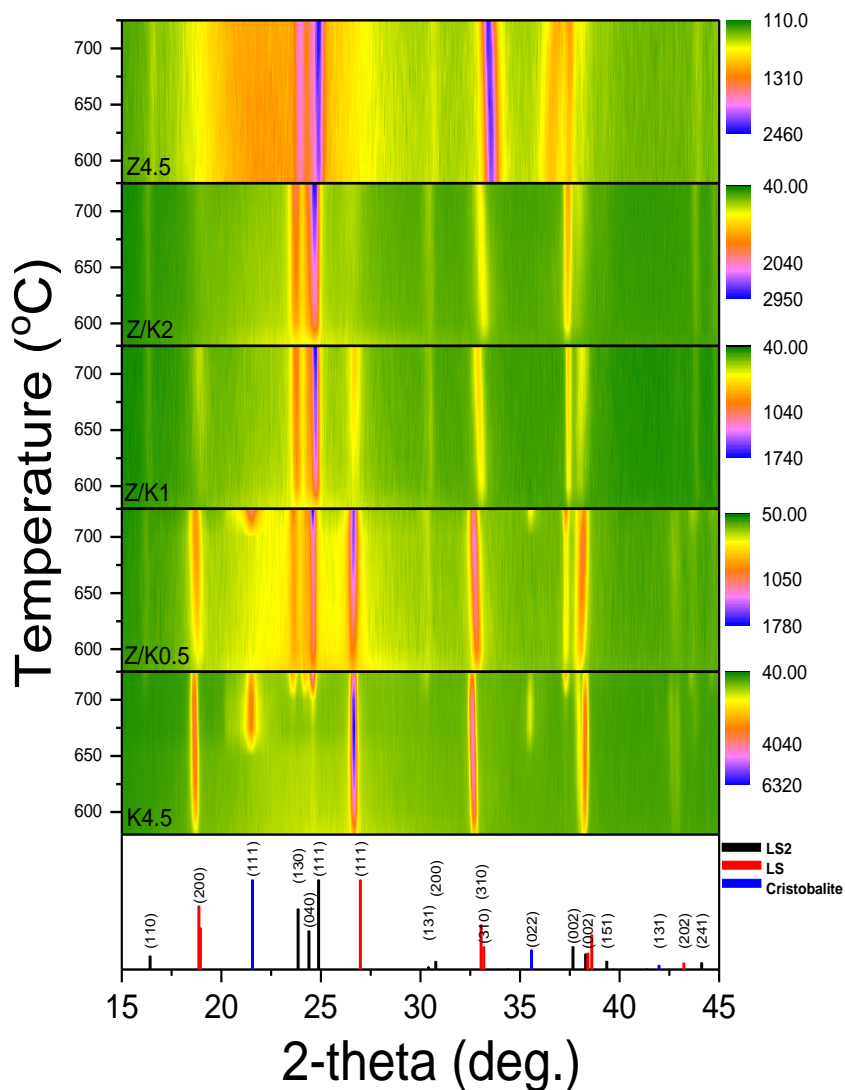
Fig. 3.5. (a) High-temperature XRD patterns of all samples in the range of 580-720 ºC and calculated lattice parameters and unit cell volume of (b) LS and (c) LS2 phases at 700 ºC.

Fig. 3.5. (b) (continued)

Fig. 3.5. (c) (Continued)

References

[1] E. El-Meliegy, R. van Noort, Glasses and Glass Ceramics for Medical Applications, Springer Science & Business Media, 2011.

[2] H.R. Fernandes, D.U. Tulyaganov, J.M.F. Ferreira, The role of P$_2$O$_5$, TiO$_2$ and ZrO$_2$ as nucleating agents on microstructure and crystallization behaviour of lithium disilicate-based glass, Journal of Materials Science, 48 (2012) 765-773.

[3] Z. Luo, J. Zhou, J. Li, C. Zhang, A. Lu, Effects of MO (M= Mg, Ca, Ba) on crystallization and flexural strength of semi-transparent lithium disilicate glass-ceramics, Bull. Mater. Sci., 34 (2011) 1511-1516.

[4] H. Harper, P. James, P. McMillan, Crystal nucleation in lithium silicate glasses, Discuss. Faraday Soc., 50 (1970) 206-213.

[5] S.C. von Clausbruch, M. Schweiger, W. Höland, V. Rheinberger, The effect of P$_2$O$_5$ on the crystallization and microstructure of glass-ceramics in the SiO$_2$–Li$_2$O–K$_2$O–ZnO–P$_2$O$_5$ system, J. Non-Cryst. Solids, 263 (2000) 388-394.

[6] X. Zheng, G. Wen, L. Song, X.X. Huang, Effects of P$_2$O$_5$ and heat treatment on crystallization and microstructure in lithium disilicate glass ceramics, Acta Mater., 56 (2008) 549-558.

[7] P. Hing, P. McMillan, A transmission electron microscope study of glass-ceramics, Journal of Materials Science, 8 (1973) 340-348.

[8] S.C. von Clausbruch, M. Schweiger, W. Höland, V. Rheinberger, Effect of ZnO on the crystallization, microstructure, and properties of glass-ceramics in the SiO$_2$-Li$_2$O-ZnO-K$_2$O-P$_2$O$_5$ system, Glass Sci. Technol., 74 (2001) 223-229.

[9] H.R. Fernandes, D.U. Tulyaganov, A. Goel, M.J. Ribeiro, M.J. Pascual, J.M.F. Ferreira, Effect of Al$_2$O$_3$ and K$_2$O content on structure, properties and devitrification of glasses in the Li$_2$O–SiO$_2$ system, J. Eur. Ceram. Soc., 30 (2010) 2017-2030.

[10] G. Partridge, Phases and transformations in lithium-zinc silicate glass-ceramics, Glass Technol., 20 (1979) 246.

[11] C.-M. Kim, H.-B. Lim, Y.-S. Kim, S.-H. Kim, K.-S. Oh, C.-Y. Kim, Effect of Various Oxides on Crystallization of Lithium Silicate Glasses, Journal of the Korean Ceramic Society, 48 (2011) 269-277.

[12] S. Huang, P. Cao, Y. Li, Z. Huang, W. Gao, Nucleation and Crystallization Kinetics of a Multicomponent Lithium Disilicate Glass by in Situ and Real-Time Synchrotron X-ray Diffraction, Crystal Growth & Design, 13 (2013) 4031-4038.

[13] D. Holland, Y. Iqbal, P. James, B. Lee, Early stages of crystallisation of lithium disilicate glasses containing P_2O_5–An NMR study, J. Non-Cryst. Solids, 232 (1998) 140-146.

[14] W. Höland, E. Apel, C. van 't Hoen, V. Rheinberger, Studies of crystal phase formations in high-strength lithium disilicate glass–ceramics, J. Non-Cryst. Solids, 352 (2006) 4041-4050.

[15] S. Huang, Z. Huang, W. Gao, P. Cao, Trace phase formation, crystallization kinetics and crystallographic evolution of a lithium disilicate glass probed by synchrotron XRD technique, Scientific reports, 5 (2015) 9159.

[16] S. Huang, Z. Zujovic, Z. Huang, W. Gao, P. Cao, Crystallization of a high-strength lithium disilicate glass-ceramic: An XRD and solid-state NMR investigation, J. Non-Cryst. Solids, 457 (2017) 65-72.

[17] S. Huang, Z. Huang, W. Gao, P. Cao, Structural Response of Lithium Disilicate in Glass Crystallization, Crystal Growth & Design, 14 (2014) 5144-5151.

[18] C. Bischoff, H. Eckert, E. Apel, V.M. Rheinberger, W. Höland, Phase evolution in lithium disilicate glass–ceramics based on non-stoichiometric compositions of a multi-component system: structural studies by [29]Si single and double resonance solid state NMR, PCCP, 13 (2011) 4540-4551.

Chapter 3: Crystallization sequence and microstructure for the SiO$_2$-Li$_2$O-P$_2$O$_5$-K$_2$O-ZnO system

[19] S. Huang, Z. Huang, W. Gao, P. Cao, In Situ High-Temperature Crystallographic Evolution of a Nonstoichiometric Li$_2$O·2SiO$_2$ Glass, Inorg. Chem., 52 (2013) 14188-14195.

[20] S. Huang, Y. Li, S. Wei, Z. Huang, W. Gao, P. Cao, A novel high-strength lithium disilicate glass-ceramic featuring a highly intertwined microstructure, J. Eur. Ceram. Soc., 37 (2017) 1083-1094.

[21] C.S. Ray, D.E. Day, Determining the nucleation rate curve for lithium disilicate glass by differential thermal analysis, J. Am. Ceram. Soc., 73 (1990) 439-442.

[22] M.C. Weinberg, Interpretation of DTA experiments used for crystal nucleation rate determinations, J. Am. Ceram. Soc., 74 (1991) 1905-1909.

[23] C.S. Ray, X. Fang, D.E. Day, New Method for Determining the Nucleation and Crystal-Growth Rates in Glasses, J. Am. Ceram. Soc., 83 (2000) 865-872.

[24] V.M. Fokin, A.A. Cabral, R.M.C.V. Reis, M.L.F. Nascimento, E.D. Zanotto, Critical assessment of DTA–DSC methods for the study of nucleation kinetics in glasses, J. Non-Cryst. Solids, 356 (2010) 358-367.

[25] M. Goswami, G.P. Kothiyal, L. Montagne, L. Delevoye, MAS-NMR study of lithium zinc silicate glasses and glass-ceramics with various ZnO content, J. Solid State Chem., 181 (2008) 269-275.

[26] F. Liebau, Untersuchungen an schichtsilikaten des formeltyps Am(Si$_2$O$_5$) n. I. Die kristallstruktur der zimmertemperaturform des Li$_2$Si$_2$O$_5$, Acta Crystallogr., 14 (1961) 389-395.

[27] R.T. Shannon, C.T. Prewitt, Effective ionic radii in oxides and fluorides, Acta Crystallographica Section B: Structural Crystallography and Crystal Chemistry, 25 (1969) 925-946.

Chapter 4

Effects of microstructures on the mechanical properties of lithium disilicate glass-ceramics for the SiO$_2$-Li$_2$O-P$_2$O$_5$-K$_2$O-ZnO system

4.1 Introduction

In order to improve the mechanical strength of LS2 GCs in a multicomponent system with nucleating agent or glass modifiers, enormous efforts have been made to refine the LS2 crystal embedded in GCs through an optimal heat treatment condition. To further enhance the mechanical properties of GCs, one should take the morphology, average size, and volume fraction of crystalline phase into account. The mechanical properties of GCs are mainly dependent on the volume of crystalline phase because the glassy matrix is more brittle than crystalline phase.

In general, the grain-size dependence of mechanical properties is historically described with the Hall-Petch relation not only for metals but also for ceramics [1]. The Hall-Petch relation in flexural strength and hardness was observed for several GCs with various microstructures modified by the crystallization processes [2-5]. However, as previously mentioned, high flexural strength and high fracture toughness in LS2 GCs are normally derived from the sample including lath-shaped crystals with high aspect ratio which hinder the crack propagation known as "interlocking effect". Therefore, it must be interesting to confirm whether the Hall-

Petch relation is applicable to LS2 GC or not. If the Hall-Petch relation works for LS2 GC, it will be very useful for the improvement of mechanical properties. Furthermore, it is well known that the difference in thermal expansion coefficient (TEC) between precipitate (crystal) and residual glass matrix in GCs can lead to the improvement of mechanical properties through the generation of compressive stress in residual glass phase when the TEC of precipitate is higher than that of glass matrix [6]. The TEC values of LS2 glass and LS2 crystal are reported to be 12.8×10^{-6}/°C and 10.8×10^{-6}/°C by Mastelaro *et al.* [7], and 12.5×10^{-6}/°C and 10.0×10^{-6}/°C by Freiman and Hench [8], respectively. Since the TEC of crystalline phase is smaller than that of glassy matrix, the tensile stress induced in glassy matrix deteriorates the flexural strength of LS2 GCs.

The cristobalite phase is frequently reported as the secondary phase in LS2 GCs since it can be easily crystallized when a silica-rich phase separation occurs in residual glass phase during LS2 crystallization [9-11]. The TEC of cristobalite is reported to be 10.9×10^{-6}/°C by Aumento *et al.* [12]. Thus, the difference in TEC between cristobalite and residual glass phase could be significantly reduced, resulting in a reduced tensile stress in glassy matrix if the cristobalite phase is included in LS2 GCs. Here, it is noteworthy that the effect of cristobalite phase on mechanical properties of LS2 GCs has never been clarified [13].

In this chapter, we investigated the effects of microstructures on the mechanical properties of LS2 GCs for the SiO₂-Li₂O-P₂O₅-K₂O-ZnO system. In chapter 3 [14], it was that the crystal size and aspect ratio of LS2 phase were dramatically decreased with increasing the ZnO/K₂O (Z/K) ratio even though the nucleating agent of P₂O₅ was fixed to have 1.5 mol%. Moreover, the amount of cristobalite

was increased with increasing the Z/K ratio. Therefore, in this chapter, we varied the amount of P_2O_5, Z/K ratio, and heat treatment conditions to control the average size and volume fraction of LS2 crystalline phase, and also the amount of cristobalite.

4.2 Experimental

Table 4.1 presents the nominal compositions of glass samples which were designated to have the same total amount of 6 mol% additives but different Z/K ratios from 1 to 2 and also different amount of P_2O_5. Precursors of SiO_2 (99%, Daejung Chemical Co., Ltd, Korea), Li_2CO_3 (98%, Daejung Chemical Co., Ltd, Korea), $(NH_4)_2HPO_4$ (98.5%, Daejung,Korea), K_2CO_3 (99%, Kojundo Chemical Lab. Co., Ltd, Japan), and ZnO (99%, Kojundo Chemical Lab. Co., Ltd, Japan) were weighed to have the nominal compositions, and dry-mixed for 4 h in 3D-mixer. The batches were melted at 1400 °C for 2 h in a Pt crucible in air, and the melts were poured to crusher to produce the frits for a re-melting process. The re-melting was conducted at 1400 °C for 2 h, and the melts were cast using two types of graphite mold to form cylindrical shape with the diameter of 13 mm and the height of 20 mm for the biaxial flexural test, and rectangular shape with the size of $130 \times 130 \times 8$ mm for the fracture toughness test.

The glass samples were annealed at 450 °C for 30 min to release the thermal stress induced by quenching process, and then furnace-cooled to room temperature. To check the possibility of evaporation of elements during the re-melting process, the compositions of the glass samples were analyzed by wavelength dispersive X-

ray fluorescence (XRF) and the Inductively coupled plasma atomic emission spectroscopy (ICP-AES). A significant loss of constituent elements was unobservable, and the random error of each component was smaller than ± 0.5 %.

The crystallization behavior was analyzed by the differential scanning calorimetry (TA, Q600, USA) with the heating rate of 10 °C/min using glass particles (bigger than 500 μm in size) to prevent the surface crystallization since the glass particle under 500 μm forms the surface nuclei, causing the shift of exothermal peak toward lower temperature. The two-stage heat treatment for nucleation and growth was performed to control the crystal size and its volume fraction. For the selection of the nucleation temperatures, we referred to previous reports on the pure LS2 glass (~455 °C) [15], and also on the multicomponent systems [16] where the temperature of maximum nucleation rate tended to increase with increasing the P_2O_5. Thus, the temperatures for nucleation were selected 460, 500, and 540 °C for 1 h while the temperatures for crystal growth were selected to be 800 and 850 °C for 2 and 4 h to obtain GC samples (total 12 heat treatment groups per each composition).

The crystalline phases produced at different heat-treatment conditions were identified by X-ray diffraction (X-ray diffractometer, D/max 2500, Rigaku, Japan) using Cu Kα radiation produced at 40 kV and 100 mA. Diffraction patterns were collected by two-theta scan from 10 to 70° with a scan speed of 5 °/min and a step width of 0.02°. The GC samples were polished and etched using 15 vol% HF solution for 10 sec and their microstructures were observed by scanning electron microscopy (FE-SEM, JSM6701F, Jeol, Japan). Elemental mapping was performed to identify each phase using energy dispersive spectroscopy (EDS)

equipped in a field emission transmission electron microscope (FE-TEM, JEM2100F, Jeol, Japan) operated at 120 kV.

The mechanical strength of GCs samples was evaluated by a biaxial flexural test (piston-on-three-ball) referring to ISO 6872 [17]. The cylindrical samples were cut into disk-shaped specimens with the diameter of 13 mm and the thickness of 1.2 mm, and mirror-polished using diamond suspension (1 μm, Allied high tech products, INC. USA). Six samples were prepared per each heat treatment group. The specimens were subjected to biaxial flexural test using a universal testing machine (RB 302ML, R&B Co. Ltd, Korea) at a cross-head speed of 0.5 mm/min. The bi-axial flexural strength was calculated using the following Eq. (1).

$$\sigma = -0.2387P(X-Y)/b^2 \qquad (1)$$

where σ is the maximum tensile stress, - 0.237 is a numerical constant ($3/4\pi$), P is the total load causing fracture, b is the thickness of the specimen. X and Y are given as the following Eq. (2).

$$X = (1+v)\ln(r_2/r_3)^2 + [(1-v)/2](r_2/r_3)^2$$
$$Y = (1+v)[1+\ln(r_1/r_3)^2] + (1-v)(r_1/r_3)^2 \qquad (2)$$

The radii of support circle r_1, the piston tip r_2, and the sample r_3 were 4.8 mm, 0.6 mm, and 0.6 mm, respectively. The poisson's ratios, v, of most dental ceramics are reported in the region of 0.20 – 0.25 [18], and those of LS2 glass and GCs are known as 0.22–0.24, and 0.24–0.27, respectively [19, 20]. In this work, the v value of 0.25 was taken for the calculation of biaxial flexural strength.

The fracture toughness K_{IC} of GC samples was determined by the SEVNB (Single-Edge-V-Notched Beam) using the three-point bending method [21]. The

rectangular GC samples were shaped to have the dimension of 3 × 4 × 40 mm, and chamfered flat with 0.1 mm at 45° angle. The specimens were mirror-polished and notched at the surface of 3 × 40 mm using a razor blade with the diamond suspension. The depth of notch was about 1 mm and the radius of crack tip was under 15 μm observed by optical microscopy. The three-point bending test for the fracture toughness was carried out by a universal testing machine with a span of 30 mm and cross-head speed of 0.5 mm/min. The K_{IC} was calculated by the following Eq. (3),

$$K_{IC} = \frac{PS}{BW^{1.5}} \times \frac{3F(\alpha)\alpha^{0.5}}{2} \qquad (3)$$

where P is fracture load, and S is support span. B and W denote the thickness and width of specimen, respectively. The initial relative length of pre-crack α is the value of which notch depth a is divided by W. The $F(\alpha)$ with a span of 30 mm is given by Eq. (4).

$$F(\alpha) = 1.964 - 2.837\alpha + 13.71\alpha^2 - 23.25\alpha^3 + 24.13\alpha^4 \qquad (4)$$

The Vickers hardness was measured by a micro-Vickers indenter (Shimadzu, HMV-2T, Japan) with the load of HV 0.5 (4.903 N) and peak hold time of 10 sec. The six Vikers indents were made on each sample. The Vickers hardness was calculated by the applied load P and measured diagonal length of the indentation d as given by Eq. (5) [1].

$$H_V = 1.854 \times \frac{P}{d^2} \qquad (5)$$

The quantitative phase analysis using X-ray diffraction was performed using the Partial or No Known Crystal Structure (PONKCS) method [22, 23] which

requires the *ZMV* "calibration constant" of the unknown phase α, the glassy phase in herein, involving the known standard material *S*, Al_2O_3. The formula was expressed by the following Eq. (6),

$$(ZMV)_\alpha = \frac{W_\alpha}{W_s} \frac{S_s}{S_\alpha} (ZMV)_s \quad (6)$$

where *W* is the known weight fraction, *ZM* is mass of unit cell contents, *V* is the unit cell volume and *S* is the scale factor in Rietveld analysis. Details are described in our previous report [24]. The fitting of the X-ray diffraction pattern was conducted by the software TOPAS (Bruker, version 4.2). The calculated weight percentage of each crystalline phase was converted to its volume percentage using theoretical density.

The residual stress was evaluated by the XRD data of crystalline phase for each sample. The displacement of diffraction peaks represents a difference in the interplanar spacing of (*hkl*) planes between stressed sample and stress-free sample [7]. The strain can be calculated by the following Eq. (7)

$$\varepsilon_{hkl} = -0.5\Delta(2\theta)\cot(\theta) = \Delta d_{hkl}/d_{hkl}, \quad (7)$$

where ε_{hkl} is the relative strain of crystal lattice normal to (*hkl*) plane. The experimental residual stress was obtained by Hooke's law

$$\sigma_{exp.} = E_{hkl}\varepsilon_{hkl} \quad (8)$$

where E_{hkl} is the direction dependent elastic modulus of the crystal. Diffraction patterns were recorded from 23 to 25.5° with a step time of 1 sec/step and a step width of 0.008°. For the accurate 2θ measurement, the XRD data were calibrated by Si (100) substrate at 2θ angle of 69.1709°. The stress-free powder samples were prepared by crushing bulk samples using a zirconia mortar and pestle and then ball-

milling with ethanol. Stress-free powder samples were observed by SEM, and their particle size was close to that of individual crystal, indicating that the minimum stress is generated at the interface between crystalline phase and residual glassy phase. The Young's modulus required for the calculation of residual stress was obtained by a nano-indenter (TriboIndenter, Hysitron Inc., USA) using the Berkovich indenter.

Thermal expansion curves of glass and GC samples were collected by the dilatometer (Netzsch, DIL 402C, Germany) with the heating rate 5 °C/min in air. Cylindrical shaped samples with a 20 mm in length were prepared. The linear TEC value of each sample was calculated in the temperature ranging from 100 to 400 °C, and its error is in the range of $\pm\ 0.5\times10^{-6}$/°C.

4.3 Results

4.3.1 Microstrcture

Fig. 4.1 shows the microstructures of samples heat-treated at 500°C for 1 h as the nucleation step and subsequently at 800°C for 2 h as the growth step. It is obvious that the average crystal size decreases with increasing the amount of P_2O_5 from 1 to 1.5 mol%, which is attributable to an increase in heterogeneous nucleation sites by LP phase like previous reports [11, 25, 26]. In addition, with increasing the amount of P_2O_5, a continuous decrease in the aspect ratio of crystalline phase is observed, which is also in good agreement with previous report [25], suggesting that P_2O_5 alters the crystal/liquid interfacial energy as a function of crystallographic orientation, resulting in more isotopic crystal morphology.

The microstructures of P1.5Z/K2 samples with different nucleation and growth conditions are shown in Fig. 4.2. It is obvious that the smallest average crystal size is achievable using the nucleation temperature of 540 °C as shown in Fig. 4.2(i) compared with the nucleation temperatures of 460 °C (Fig. 4.2(a)) and 500 °C (Fig.4.2e)). At the nucleation temperatures of 460 and 500 °C, the increase of growth temperature from 800 to 850 °C leads to the increase of average crystal size as shown in Figs. 4.2(a) and (c), and 4.2(e) and (g), respectively. In contrast, for the nucleation temperature of 540 °C, the increase in average crystal size is less significant with increasing the growth temperature.

In Fig. 4.3, the aspect ratios versus crystal sizes are plotted for the GC samples prepared with various heat treatment conditions for glass samples with three different compositions. Here, it should be noted that both crystal size and aspect ratio values were assumed to be average values between LS2 and cristobalite phases since these two crystalline phases were indistinguishable in SEM micrographs as shown in Figs. 4.1 and 4.2. Meanwhile, the LP crystalline phase is well known to exist within LS2 or cristobalite phases as their nucleation sites [27]. First of all, from this figure, we can see that the average crystal size tends to decrease from ~10 μm to 270 nm and the aspect ratio also decreases from ~5.5 to 1.9 with increasing the amount of P_2O_5, implying that the aspect ratios of crystalline phases are governed mainly by the amount of P_2O_5 additive. The average crystal sizes varied from ~10 to 3 μm, and ~3 to 1 μm, and ~1 μm to 270 nm in the P1Z/K1, P1.25Z/K0.7, and P1.5Z/K2 samples, respectively. Secondly, in accordance with our expectation, the average crystal size consistently increases with increasing the holding time at the growth stage for given nucleation and growth temperatures. It must be noted that the smallest crystal sizes

are obtainable from the nucleation temperatures of 500 °C for P1Z/K1 and 540 °C for P1.25Z/K0.7 and P1.5Z/K2, implying that the maximum nucleation rates are increased with increasing the amount of P_2O_5.

Finally, LS2 GC samples from P1Z/K1 show the most significant variation in their aspect ratios compared with those from P1.25Z/K0.7 and P1.5Z/K2. Their aspect ratios are abruptly decreased with increasing the holding time from 2 to 4 h, which might be attributable to relatively lower nuclei density in P1Z/K1 samples since relatively lower nuclei density could facilitate the space for crystal growth, especially along the short length direction, leading to decreased aspect ratio. However, relatively higher nuclei densities in both P1.25Z/K0.7 and P1.5Z/K2 samples with increasing the amount of P_2O_5 might cause no significant variation in their aspect ratios not only due to a crystal impingement but also, as previously mentioned, due to the alteration of crystal/liquid interfacial energy as a function of crystallographic orientation, resulting in decrease of aspect ratio [38].

4.3.2 Mechanical properties

Fig. 4.4 presents the biaxial flexural strength as a function crystal size for GC samples which were prepared by varying heat treatment conditions. The biaxial flexural strengths of P1Z/K1 samples are increased with decreasing the average crystal size as shown in Fig. 4.4(a). The samples with the smallest average crystal size reaching ~3 μm exhibits the highest strength among all P1Z/K1 samples. The biaxial flexural strengths of P1.5Z/K0.7 samples nucleated at 460 °C are increased with decreasing the average crystal size as shown in Fig. 4.4(b). However, while the

samples nucleated at 500 and 540 °C and then grown at 800 °C have the average crystal size of ~1 μm, their flexural strengths are highly scattered in the region of 350 – 450 MPa. Interestingly, a severe scattering in flexural strength data is observable for P1.5Z/K2 samples regardless of average crystal size as shown in Fig. 4.4(c).

For all samples, the dependence of average crystal size on biaxial flexural strength was replotted as the plot of σ_f versus $d^{-1/2}$ in Fig. 4.4(d) to check whether the data would follow the Hall-Petch relation given by Eq. (9) [1],

$$\sigma_f = \sigma_y + k_y d^{-1/2} \quad (9)$$

where σ_y is the yield stress for the easiest slip system of a single crystal and k_y is constant and d is grain size. While the Hall-Petch relation is roughly observed for both P1Z/K1 and P1.25Z/K0.7 samples, the flexural strength data are widely scattered for P1.5Z/K2 samples, indicating that the data seriously deviate from the Hall-Petch relationship. The reason for this deviation from Hall-Petch relationship will be discussed later. The σ_y and k_y values of the Hall-Petch relation evaluated from the data of P1Z/K1 and P1.25Z/K0.7 samples with the crystal sizes ranging from 12 to 1 μm were 120.43 MPa and 0.36 MPa·m$^{1/2}$, respectively. It may be interesting to compare present data with a typical ceramics like alumina. Rice [28] summarized the flexural strength data of polycrystalline Al₂O₃. Although a large scattering is observed in the fine-grain branch data due to a variety of sources like sizes of flaws, surface finish, and pores, he found that an increasing trend in flexural strength with decreasing grain size was clearly observed down to nanocrystalline region in size. The σ_y and k_y values of polycrystalline Al₂O₃ ceramics with the average grain sizes

ranging from 10 to 0.7 μm were reported to have 156.58 MPa and 0.45 MPa·m$^{1/2}$, respectively, which are much higher than those of our GC samples.

Fig. 4.5 shows the Vickers hardness of GC samples with various heat treatments. The Vickers hardness data of P1Z/K1 samples are represented in Fig. 4.5(a). In this figure, when the average crystal size is in the region of 3–5 μm, the hardness values are in the region of 5.0–5.5 GPa and almost independent of the average crystal size. However, when the average crystal size is larger than ~ 7 μm, the data show a bimodal trend and thus seem to be highly scattered. On the other hand, as shown in Figs. 4.5(b) and (c), the Vickers hardnesses are increased with decreasing the average crystal size in P1.25Z/K0.75 and P1.25Z/K2 samples, and hence the Hall-Petch relation is reasonably satisfied below the average crystal size of ~ 7 μm in Fig. 5(d). The Hall-Petch relation for hardness is given by Eq. (10),

$$H = H_0 + k_h d^{-1/2} \quad (10)$$

where H_0 is the initial hardness and k_h is the Hall-Petch slope [29]. The H_0 and k_y values of the Hall-Petch relation evaluated from the data of P1.25Z/K0.7 and P1.5Z/K2 samples with the average crystal sizes ranging 4 to 0.27 μm were 5.04 GPa and 6.73×10^{-4} GPa·m$^{1/2}$, respectively. We can see the H_0 and k_y values of our samples are much lower than those of polycrystalline Al₂O₃ ceramics with the average grain sizes ranging from 2 to 4 μm [45] since those are reported to have 22.73 GPa and 4.10 ×10^{-4} GPa·m$^{1/2}$, respectively.

The fracture toughness test was carried out for the samples heat-treated at 500 °C for 1 h and then 800 °C for 2 h. The fracture toughness, average crystal size, and aspect ratio are listed in Table 4.2 in three different samples of P1Z/K1, P1.25Z/K0.7

and P1.5Z/K2. In contrast to the trend in their biaxial flexural strength and Vickers hardness data, the variation in their fracture toughness data is insignificant and almost irrespective of their average crystal sizes or aspect ratios.

4.3.3 Crystallization behavior

The DSC curves for glass samples are presented in Fig. 4.6, and their characteristic temperatures are summarized in Table 4.3. The samples of P1Z/K1 and P1.25Z/K0.7 reveal one exothermic peak while the sample of P1.5Z/K2 exhibits two exothermic peaks. To identify the potential phases related to these two DSC exothermic peaks, *in-situ* high-temperature XRD (HT-XRD) analyses were performed for the P1Z/K1 sample as shown in Fig. 4.7(a). From Fig. 4.7(a), in addition to strong LS2 peaks, very weak LS peaks are observable in the early crystallization stage below 600 °C, very weak cristobalite peak begins to appear at ~ 700 °C, and very weak LP peak emerges above 850 °C. The amounts of LS, cristobalite, and LP phases are considered to be insufficient for generating latent heat by their crystallization. Therefore, the T_{p1} value of the P1Z/K1 sample might be mainly related to the evolution of LS2 phase. Referring to our previous report [30], while the T_{p1} values of the sample P1.5Z/K2 (the sample ID with Z/K2 in the reference) were identified as the simultaneous crystallization of LS and LS2 phases, T_{p2} values were related to the evolution of cristobalite and solid-state reaction between LS and cristobalite. It is in good agreement with the previous report from Mortuza *et al*., [31] that the disproportionation in glass network from Q^3 (LS2) to Q^2 (LS) and Q^4 (SiO₂) is induced with increasing the amount of P₂O₅. With 1 mol% of P₂O₅ addition, the glass

network predominantly consisted of Q^3 crystallizes directly into LS2 phase. With increasing P_2O_5 up to 1.5 mol%, the disproportioned Q^2 and Q^4 are developed as LS in the early crystallization, and cristobalite phase is formed at higher temperature, resulting in the solid-state reaction between LS and cristobalite to form the LS2 phase. Moreover, with increasing the content of P_2O_5 from 1.0 to 1.5 mol%, the first exothermic peak (T_{p1}) shifts to lower temperature, and also its height (δT_{p1}) increases, implying that the nucleation rates of LS2 and/or LS phases might be significantly increased on the basis of the assumption that the greater shifts of T_{p1} to lower temperature and higher δT_{p1} reflect an increase in the concentration of nuclei [32, 33].

Fig. 4.7(b) exhibits the XRD patterns of samples heat-treated at 500°C for 1 h and 800°C for 2 h. The LS2 and LP phases are detectable in the sample of P1Z/K1.With increasing the content of P_2O_5, the intensities of cristobalite and LP phases are significantly improved. The volume fractions of crystalline phases of GC samples are presented in Fig. 4.7(c). The standard deviation of LS2 volume fraction is ~ 3%, and those of LP and cristobalite volume fractions are below 1% although samples were produced using various heat treatment conditions of total twelve groups, implying that the volume fractions of crystalline phases are insensitive to the nucleation temperature, crystal growth temperature, and growth time used for this study while the average crystal size and morphology are very sensitive to these processing parameters. The volume fractions of residual glassy phase in all samples are in the region of 27–30%. However, while the volume fraction of LS2 phase is decreased with increasing P_2O_5, those of LP and cristobalite phases are increased. Therefore, the dependence of biaxial flexural

strength and Vickers hardness on average crystal size for each composition is considered to be valid since the variation in the volume fractions of residual glassy phase is not so significant. Table 4.4 shows the volume fractions evaluated for the samples heat-treated at 500 °C for 1 h and then 800 °C for 2 h. It is noticeable that the decrease of biaxial strength with decreasing average crystal size is accompanied by the increase in the volume fractions of cristobalite and LP phases when that of main LS2 phase is decreased and the residual glassy phase is unaltered. Thus, the existence of cristobalite and LP phases seems to be unfavorable for the enhancement of biaxial strength.

4.3.4 Micro residual stress

The micro residual stress in LS2 phase is considered to be an important factor for the evaluation of internal residual stresses in GCs. The 2θ angles along the lattice planes of (130), (040) and (111) of LS2 phase in both stress-free powder and bulk samples are summarized in Table 4.5. The heat treatment conditions of bulk samples were exactly the same with those of samples for fracture toughness test. The micro residual stresses were evaluated by measuring the strain and the elastic modulus along each lattice plane. The elastic modulus of polycrystalline LS2 is reported as 122 GPa by Mastelaro *et al*. [7]. In this study, the elastic modulus of LS2 GCs was obtained by nano-indentation measurement as the value of 123.7 ± 7.5 GPa for P1.5Z/K2 sample, and it was employed to calculate the residual stress using Eqs. (7) and (8). The P1Z/K1 sample presents tensile stresses along the (130) and (040) planes whereas it shows compressive stress in (111) plane, and its

average stress in those three planes is 0.6 MPa. With increasing the P_2O_5 and Z/K ratio, the average compressive stresses were increased to -184.2 and -216.4 MPa for P1.25Z/K0.7 and P1.5Z/K2, respectively.

4.3.5 Thermal expansion

Fig. 4.8 displays the thermal expansion curves of the samples heat-treated at 500 °C for 1 h and then 800 °C for 2 h, For a comparison, those of corresponding as-quenched glass samples are also presented as the insets. The glass samples present a similar expansion behavior regardless of P_2O_5 and Z/K ratio, while the GCs exhibit the tendency of increase in thermal expansion with increasing the P_2O_5 and Z/K ratio. The P1Z/K1 sample without cristobalite phase exhibits the lowest thermal expansion in the temperatures ranging from 200 to 700 °C among all samples. The thermal expansion increases with increasing the amount of P_2O_5 and Z/K ratio. Particularly, the notable hump near ~ 200 °C is observed for the P1.5Z/K sample including a lot of cristobalite phase, suggesting that the alpha-to-beta transition of cristobalite phase occurs at ~200 °C. The equilibrium temperature of alpha-to-beta is known to locate at 220 °C [12], and the transition temperature is highly variable in the region of 170–270 °C for synthetic cristobalites since the structural substitution along with associated defects, vacancies and strains hinder the transformation between low-temperature α-tetragonal phase (ρ=2.33 g/cm³) and high-temperature β-cubic phase (ρ=2.20 g/cm³) [34]. A similar thermal expansion behavior due to the transition of alpha-to-beta cristobalite was also reported by other researchers [35, 36]. In addition,

when beta-to-alpha transition occurs, microcracks are known to be induced by 4.9 vol% reduction [37, 38]. Thus, highly scattered flexural strengths observed for the P1.5Z/K2 sample in Fig. 4.4(c) is presumably attributable to the formation of microcracks induced by considerable cristobalite phase. The measured TEC data in the temperature region of $100 - 400°C$ are listed in Table 4.6. The P1Z/K1 sample shows the lowest TEC value of $10.54×10^{-6}/°C$ while the P1.5Z/K2 sample reveals the highest TEC value of $12.90×10^{-6}/°C$. Interestingly, as-quenched glass samples exhibit the variation of TEC values opposite to their corresponding GC samples although it is not so significant. Furthermore, according to Villas-Boas *et al.*, [39], the TEC of residual glass ($\alpha_{res.glass}$) and average crystallized phases can be estimated using a rule of mixture using Eq. (11) as follows,

$$\alpha_{res.glass} = \frac{\alpha_{GCs} - f × \bar{\alpha}_{cryst.vol}}{1 - f} \quad (11)$$

where f is the volume fraction of crystalline phases measured using XRD and $\bar{\alpha}_{cryst.vo}$ is the average TEC of all crystallized phases. The average TECs of LS2, cristobalite and LP phases were taken as $10.4×10^{-6}$, $10.9×10^{-6}/°C$, and $14.5×10^{-6}/°C$, respectively, referring to the literatures [12, 39]. The calculated TEC values of residual glasses are remarkably increased from $10.48×10^{-6}$ to $16.84×10^{-6}/°C$ with increasing the of P₂O₅ and Z/K ratio while that of the average crystallized phases ($\alpha_{cryst.vol}$) is increased from $10.56×10^{-6}$ to $11.32×10^{-6}/°C$ as listed in Table 4.6. Therefore, the increase of TEC with increasing of P₂O₅ and Z/K ratio in GCs might be caused not only by the crystalline phases and also by residual glass phase. Further, the increase of compressive stress in LS2 phase shown in Table 4.4 might also be associated with the increase of TEC in residual glass phase surrounding the crystal phase.

4.4 Discussion

4.4.1 Identification of crystalline phases in the microstructures

In Figs. 4.1 and 4.2, it is impossible to distinguish three different crystalline phases of LS2, LP, and cristobalite, existing in GC samples as shown in Fig. 4.7(b), and thus all crystals in each sample were included to evaluate the average crystal size shown in Table 4.2 and Figs. 4.3–4.5. However, as shown in Fig. 4.7 and Table 4.4, the P1.5Z/K2 samples contain the considerable LP and cristobalite phases although the major phase is LS2 phase. At the growth temperature of 850 °C, a significant growth of crystals is observed in Figs. 4(c), (d), (g), (h), (k) and (l), which is accompanied by an increase in the aspect ratio. However, we can also observe some equiaxed submicron-sized crystals in Fig. 4(g). These equiaxed submicron crystals are suspected as cristobalite since LS2 phase is known to have growth anisotropy, resulting in rod-like crystals [25, 40].

However, it is important to differentiate the LS2 and cristobalite phases since the crystal morphology or distribution of cristobalite might affect the mechanical properties. Thus, we performed the TEM-EDS mapping to distinguish the LS2, and cristobalite phases for P1.5Z/K2 sample heat-treated at 500 °C for 1 h and then 800 °C for 2 h as shown in Fig. 4.9. In this figure, the dark gray represents the LS2 or cristobalite phases, and the bright gray denotes residual glassy phase or the LP phase since the heavy atom is brighter than light atom. As shown in Fig. 4.9(b), the additives of Zn and K for the crystallization are located in the residual glassy phase, and P resides in LP phase or residual glassy phase. Referring to previous reports [27, 41], the nano-sized LP phase could be observed as a

heterogeneous nucleation center for LS, LS2, and cristobalite phases. Likewise, nano-sized phases pointed by the arrows in Fig. 4.9(a) are believed to be LP phase. Unfortunately, however, as shown in Fig. 4.9(b), LS2 phase is indistinguishable from cristobalite phase via TEM-EDS analysis since Li in LS2 is undetectable. As a result, except P1Z/K1 sample with no cristobalite, the measured average crystal sizes in Table 4.2 and Figs. 3–5 might include the cristobalite crystals, producing the considerable errors in the average crystal size of LS2, especially for the P1.5Z/K2 sample with appreciable amount of cristobalite.

4.4.2 Factors affecting mechanical properties of LS2 GCs

As shown in Fig. 4.4, while the biaxial flexural strength data of P1Z/K1 and P1.25Z/K0.7 samples satisfy the Hall-Petch relation, those of P1.5Z/K2 samples seriously deviate from this relation. Such a serious deviation from the Hall-Petch relation for the P1.5Z/K2 sample, because of severely scattered flexural strength data, is primarily ascribed to the existence of a significant amount of cristobalite ($\sim$ 8.4 vol%) since its beta-to-alpha transformation can generate microcracks during the cooling process. Another factor affecting the mechanical properties of GC samples might be a significant difference in TEC between LS2 crystal and residual glassy phase which can generate micro stresses at the interface [42].

To further understand the above difference in the behaviors of flexural strength vs crystal size between P1Z/K1 and P1.5Z/K2 samples, we observed their fracture surfaces as shown in Fig. 4.10. The fracture surface of P1Z/K1 sample is smoother

than that of P1.5Z/K2 sample. It can be seen from Fig. 4.10(c) that the cracks might randomly propagate through LS2 crystals in the P1Z/K1 sample, suggesting intragranular fracture mechanism. On the contrary, in the P1.5Z/K2 sample, the microcracks might propagate with the curving and intersecting paths represented by the arrows in Fig. 4.10(d), indicating that the cracks might propagate through residual glassy phase, which is pretty similar to intergranular fracture mechanism in fine-grained ceramics, where the intergranular fracture occurs due to a highly concentrated stress at the grain boundary facet that makes crack propagation easier along the grain boundary [43]. These results also indicate that the micro tensile stresses generated in residual glassy phase are gradually increased with increasing the P_2O_5 and Z/K ratio because of TEC increment in residual glassy phase. The micro tensile stress in residual glassy phase can be confirmed by the counterpart compressive stress in LS2 crystal as presented in Table 4.5. Enhanced tensile stress in residual glassy phase promotes the crack propagation in residual glassy phase rather than crystalline phase when the external tensile stress is applied during the biaxial flexural strength test.

Li *et al.* [44] investigated the effect of LS2 crystal size on the mechanical properties of LS2 GCs (crystallinity of 66%). They found that the 3-point bending strength was gradually enhanced with increasing LS2 crystal size to a certain size due to the interlocking effect but it was decreased with further increasing crystal size due to an increased micro residual tensile stress in residual glassy phase, which was called as the dual effects of interlocking and micro residual stress. They suggested that higher micro residual tensile stress was caused by increased LS2 crystal size and crystal aspect ratio.

Unlike their report, however, the biaxial flexural strengths are improved with decreasing average crystal size in this study, following the Hall-Petch relation. With further refining crystal size, the flexural strengths are severely scattered mainly due to the formation of appreciable amount of criostbalite phase as previously mentioned. Furthermore, the micro tensile stress in residual glassy phase caused by a large difference in TEC between crystalline and residual glass phases can decrease the flexural strength as well.

According to the Hall-Petch relation in ceramics, the flexural strength is governed by the microplasiticity failure in large grain branches and the flaw failure in fine grain branches [43]. Therefore, the initial enhancement of flexural strengths for P1Z/K1 samples in Fig. 4.4(d) is considered to follow the microplastic failure where the crystal size might be larger than flaw size. while, for P1.5Z/K2 samples with finer crystal size, the fracture mechanism is considered as flaw failure. However, in GC samples, the Hall-Petch relation may be more complicated since the crystals are embedded in glassy matrix. A micro stress at the interface between crystal and residual glass matrix may also affect the failure mechanism determining fracture mode if the surface finishing, pores, and impurities in LS2 crystal are excluded. According to Hall-Petch relation, with decreasing crystal size, the flexural strength is expected to increase. However, the flexural strengths not only negatively deviate from the Hall-Petch relation but also highly scatter in Fig. 4.4 (d). The negative deviation of flexural strength with decreasing the crystal size might be due to the micro tensile stress in residual glassy phase, and the severe scattering of flexural strength might be due to the microcracks induced by cristobalite. Consequently, it can be suggested that the biaxial flexural strength may be further improved with

decreasing the crystal size if the formation of cristobalite phase in GCs can be avoided or at least suppressed below a certain amount, and also if the micro tensile stress in residual glassy phase due to the difference of thermal expansion between crystalline phase and residual glassy phase can be minimized.

Interestingly, as shown in Fig. 4.5, the Hall-Petch relation in Vickers hardness is preserved even for P1.5Z/K2 samples unlike their biaxial flexural strength data in Fig. 4.4, implying that it is almost independent of the microcracks induced by the structural transition of cristobalite and higher micro tensile stress in residual glassy phase. This result is in good agreement with the previous report by Li *et al.* [44] in that the nano-indentation hardness decreased with increasing the LS2 crystal size. They reported the hardness values ranging from 7 to 9 GPa which is higher than our Vickers hardness values ranging from 4.5 to 6 GPa. This discrepancy in the hardness values is most probably due to the intrinsic size effect that the contact depth of micro-indentation is always higher than that of nano-indentation, resulting in lower hardness values in micro-indentation [45-47]. Meanwhile, they also suggested that higher residual tensile stress in glassy matrix, formed in the GC samples with the LS2 average crystal sizes in the region of 1 – 5 μm, caused lower hardness because of reduced deformation-resistance. In contrast, in our work, higher residual tensile stress in glassy matrix was generated in the P1.5Z/K2 samples with the average crystal size ranging from 0.3 to 1 μm. These samples exhibited no degradation in Vickers hardness. Instead, it was consistently increased with decreasing the average crystal size as shown in Fig. 4.5(d), which is probably due to finer crystals which might reinforce the resistance for microplastic deformation by the retardation of dislocation motion [48]. In addition, enhanced deformation-resistance in the GCs

due to finer crystals might diminish the negative effect of residual tensile stress in glassy matrix on hardness.

On the other hand, the fracture toughness is almost unaltered with the crystal size, existence of cristobalite and higher TEC of residual glassy phase when the volume fractions of crystalline phase are similar to each other. It is known that the main factor for the toughening in GCs is the volume fraction of crystal phase [49, 50]. However, Hill *et al*., [51] reported that the fracture toughness increases with increasing the aspect ratio of crystal phase in baria-silicate GCs. They demonstrated that while toughing occurred in the samples with the aspect ratio values ranging from 1.4 to 3.6 due to a crack deflection, resulting in an increase in fracture toughness from 1.0 ± 0.1 to 1.4 ± 0.2 MPa·m$^{1/2}$, additional toughening mechanism could be found in the sample with higher aspect ratio of 8.1 most probably due to crack bridging, leading to fracture toughness of 2.2 ± 0.6 MPa·m$^{1/2}$. In our case, the aspect ratio of GCs varied from the 1.9 to 4.1 as shown in Table 2, indicating that the crack deflection might occur, however, there is no difference in fracture toughness. Moreover, it has been reported that the fracture toughness of GCs is affected by the TEC mismatch between crystal and residual glass phases, leading to a variation in the crack propagation path [49]. However, the effect of residual stress on fracture toughness is complicated in GCs with high volume fraction of crystal phase since the state of stress around the crystal can be very complex [52]. This complex stress state might be responsible for unaltered fracture toughness in our sample.

4.4 Summary

The total volume fractions of LS2, Li_3PO_4, and SiO_2 (cristobalite) crystalline phases in GC samples were in the region of 0.70–0.73 regardless of various heat treatment conditions. The Hall-Petch relation was obtainable from the dependence of biaxial flexural strength on average crystal size for the samples without cristobalite phase and with negligibly small micro stresses generated at the interface between LS2 crystal and residual glassy phase. In the GC samples having appreciable amount of cristobalite like 8.4 vol%, however, the biaxial flexural strength data as a function of average crystal size were significantly scattered and hence largely deviated from the Hall-Petch relation, which may be caused by the microcracks induced by beta-to-alpha transition of cristobalite during the cooling process after crystallization. In addition, an abrupt increase in TEC of residual glassy phase is considered to deteriorate the flexural strength by introducing a micro tensile stress in residual glassy phase. Interestingly, for the sample with 8.4 vol% cristobalite, unlike the flexural strength data, Vickers hardness data followed the Hall-Petch relation quite well since the micro tensile stress in residual glassy matrix might be diminished by the enhanced deformation-resistance. The fracture toughness was not sensitive to the factors like crystal size, existence of cristobalite, and significant tensile stress in residual glassy phase. Instead, it was mainly dependent on the total volume fraction of crystalline phases. Further improvement of the mechanical strength of LS2 GCs may be possible if the formation of cristobalite can be avoided or suppressed to a negligibly small amount, and also if the difference of thermal expansion between crystalline phase and residual glassy phase can be minimized.

Table 4.1. Table 1. Nominal compositions of glass samples (in mol %).

Sample ID	SiO_2	Li_2O	P_2O_5	K_2O	ZnO
P1Z/K1	66.27	27.73	1	2.5	2.5
P1.25Z/K0.7	66.27	27.73	1.25	2.75	2
P1.5Z/K2	66.27	27.73	1.5	1.5	3

Table 4.2. Fracture toughness (K_{IC}), average crystal size (along the long length), and aspect ratio for the samples heat-treated at 500°C for 1 h and then 800°C for 2 h.

Sample ID	K_{IC} (MPa·m$^{0.5}$)	Average crystal size (µm)	Aspect ratio
P1Z/K1	2.76 ± 0.14	7.3 ± 2.2	4.1 ± 1.4
P1.25Z/K0.7	2.43 ± 0.35	1.0 ± 0.3	2.9 ± 0.9
P1.5Z/K2	2.65 ± 0.39	0.4 ± 0.1	1.9 ± 0.7

Table 4.3. DSC characteristic temperatures of the glass samples measured with a heating rate of 10 °C/min in air, where T_g is the glass transition temperature, T_x is the onset temperature of the crystallization peak, T_p is the crystallization peak temperature, δT_p is the height of crystallization peak, and T_m is the melting peak temperature.

Sample ID	Glass transition	1st exothermic peak			2nd exothermic peak			Melting peak
	T_g (°C)	T_{x1} (°C)	T_{p1} (°C)	δT_{p1} (°C)	T_{x2} (°C)	T_{p2} (°C)	δT_{p2} (°C)	T_m (°C)
P1Z/K1	462.8	613.8	648	0.8	–	–	–	987.6
P1.25Z/K0.7	465.1	604.1	623	1.6	–	–	–	985.5
P1.5Z/K2	465.6	583.1	597	2.6	722.1	729.3	0.4	993.2

Table 4.4 Calculated volume fractions of crystalline phases by the PONCKS method in the samples heat-treated at 500ºC for 1 h and then 800ºC for 2 h.

Sample ID	Volume fraction of phases (vol%)			
	Residual glass	LS2	LP	Cristobalite
P1Z/K1	26.7 ± 0.9	69.1 ± 0.9	3.2 ± 0.1	–
P1.25Z/K0.7	26.1 ± 0.7	65.3 ± 0.7	4.5 ± 0.3	1.6 ± 0.3
P1.5Z/K2	28.6 ± 1.1	56.6 ± 1.1	6.4 ± 0.2	8.4 ± 0.3

Table 4.5. X-ray diffraction data, and experimental internal strains and stresses calculated by Eq. (7).

Sample ID	(hkl)	$2\theta_{powder}$	d_{powder} (Å)	$2\theta_{bulk}$	d_{bulk} (Å)	ε ($\times10^{-3}$)	$\sigma_{exp.}$ (MPa)
P1Z/K1	(130)	23.7563	3.7423	23.7537	3.7427	0.11	13.50
	(040)	24.2999	3.6598	24.2972	3.6602	0.11	13.69
	(111)	24.8041	3.5865	24.8093	3.5858	-0.21	-25.38
P1.25Z/K0.7	(130)	23.7576	3.7421	23.7891	3.7372	-1.31	-161.65
	(040)	24.3091	3.6584	24.3485	3.6526	-1.60	-197.47
	(111)	24.8054	3.5863	24.8448	3.5808	-1.56	-193.39
P1.5Z/K2	(130)	23.7576	3.7421	23.8007	3.7354	-1.79	-221.18
	(040)	24.3169	3.6573	24.3601	3.6509	-1.75	-216.44
	(111)	24.8133	3.5852	24.8564	3.5791	-1.71	-211.49

Table 4.6. Measured linear TEC of the glass and GCs, and calculated TEC values of residual glass and crystalline phases based on the rule of mixture in the temperature region of 100 – 400 °C.

Sample ID	TEC (10^{-6}/°C)			
	Glass	GCs	Residual glass	Average TEC of crystalline phases ($\alpha_{cryst.vol}$)
P1Z/K1	12.43	10.54	10.48	10.56
P1.25Z/K0.7	12.31	11.58	13.67	10.74
P1.5Z/K2	12.23	12.90	16.84	11.32
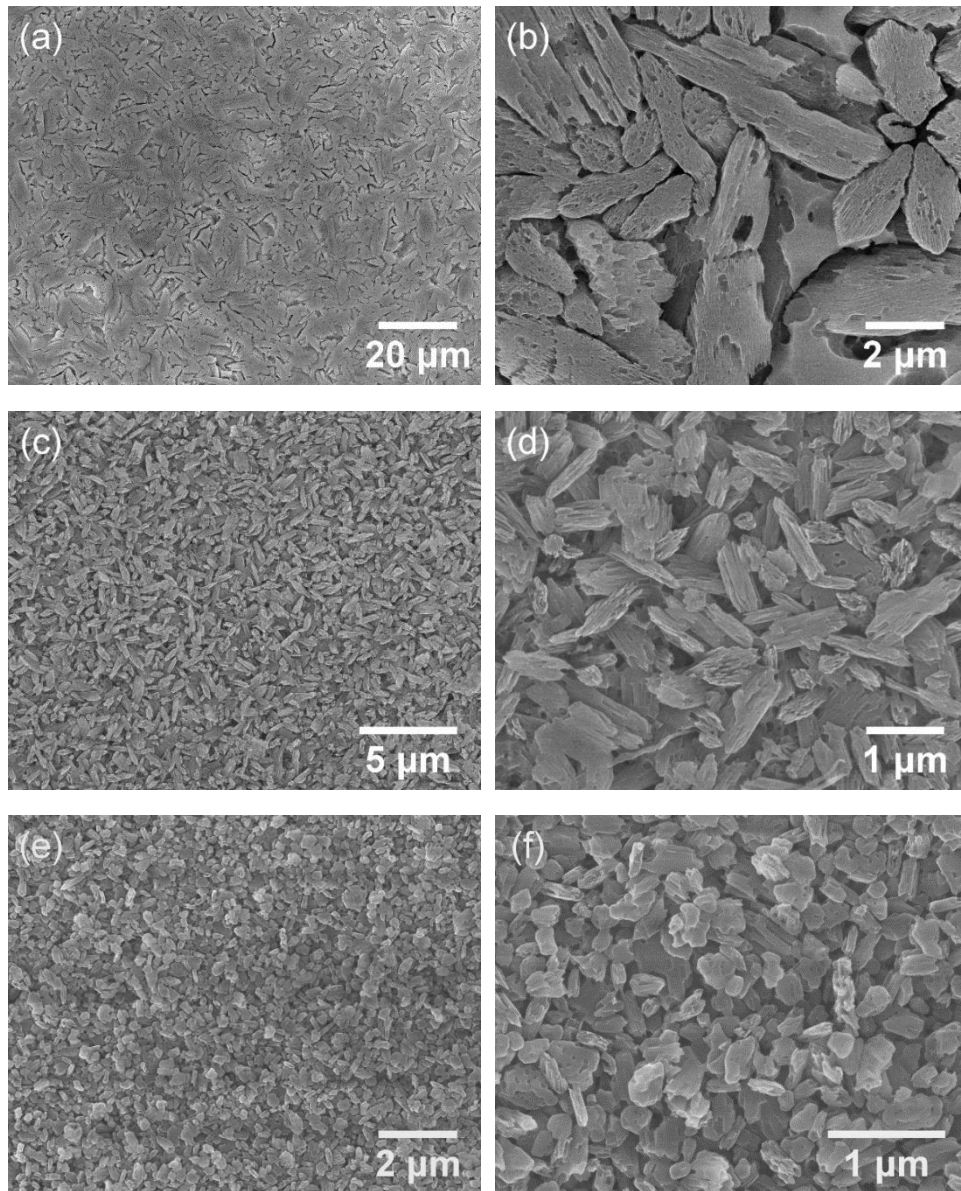
Fig. 4.1. SEM micrographs of (a–b) P1Z/K1, (c–d) P1.25Z/K0.7, and (e–f) P1.5Z/K2 with low (left) and high (right) magnifications. All samples were heat-treated at 500ºC for 1 h and then 800ºC for 2 h. The residual glassy phase was etched by 15 vol% HF solution for 10 sec
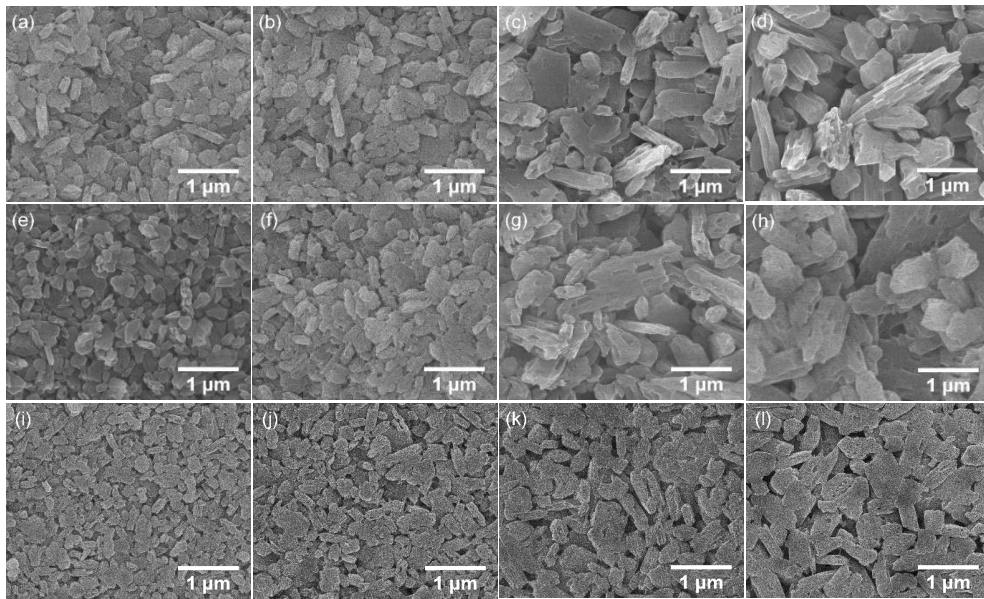
Fig. 4.2. SEM micrographs of P1.5Z/K2 samples nucleated at (a) – (d) 460 ℃, (e) – (h) 500 ℃, and (i) – (l) 540 ℃. At the growth temperature of 800 ℃, the GC samples (a), (e) and (i) were grown for 2 h, and (b), (f) and (j) for 4 h, respectively. At the growth temperature of 850 ℃, the samples (c), (g) and (k) were grown for 2 h, and (d), (h) and (l) for 4 h, respectively. The residual glassy phase was etched by 15 vol% HF solution for 10 sec.
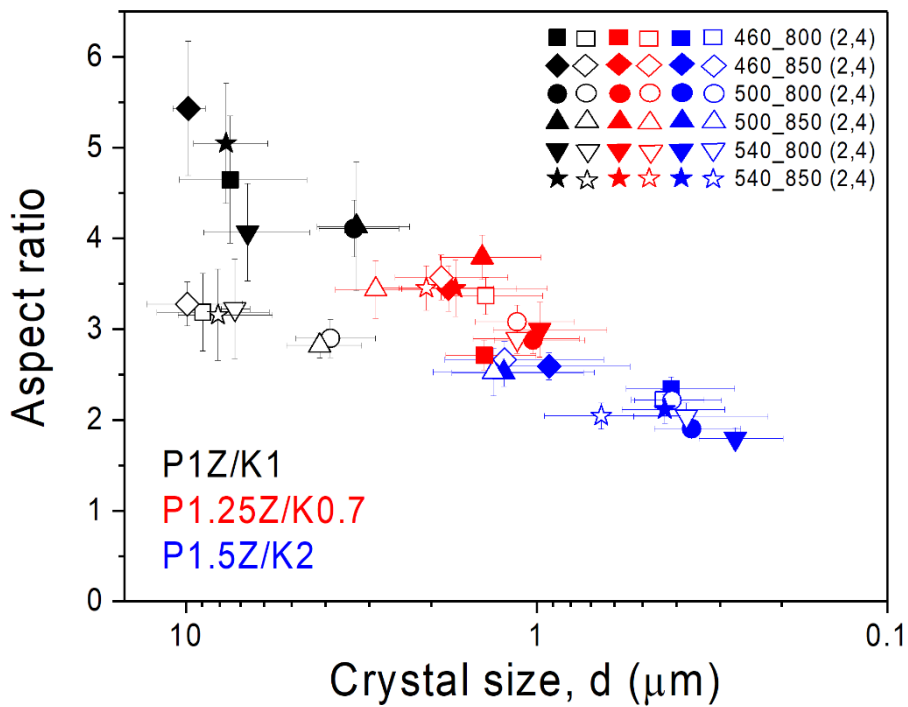
Fig. 4.3. Aspect ratio versus average crystal size (along the long length) of GC samples. Vertical and horizontal error bars represent standard deviations. The symbol was designated with the heat treatment conditions for nucleation (460, 500, 540 °C) for 1 h and crystal growth (800, 850 °C) for 2 h and 4 h. Closed symbols and opened symbols denote the holding times of 2 h and 4 h, respectively, at the growth stage.
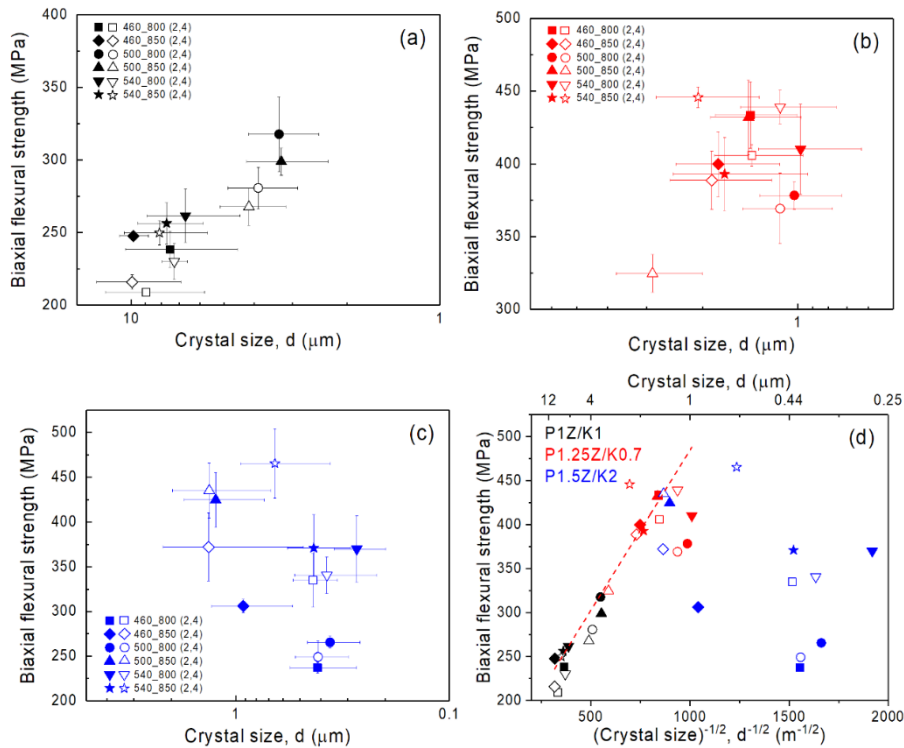
Fig. 4.4. Biaxial flexural strength versus average crystal size of GC samples (a) P1Z/K1, (b) P1.25Z/K0.7, (c) P1.5Z/K2, and (d) all data points in reciprocal of crystal size. Vertical and horizontal error bars represent standard deviations. The vertical and horizontal error bars were removed in (d) to easily differentiate each data point. The symbol was designated with the heat treatment conditions for nucleation (460, 500, 540 ºC) for 1 h and crystal growth (800, 850 ºC) for 2 h and 4 h. Closed symbols and opened symbols denote the holding times of 2 h and 4 h, respectively, at the growth stage. The red dashed line in (d) is the linear regression line of Hall-Petch relation given by Eq. (9) for the P1Z/K1 and P1.25Z/K0.7 samples (R^2=0.802).
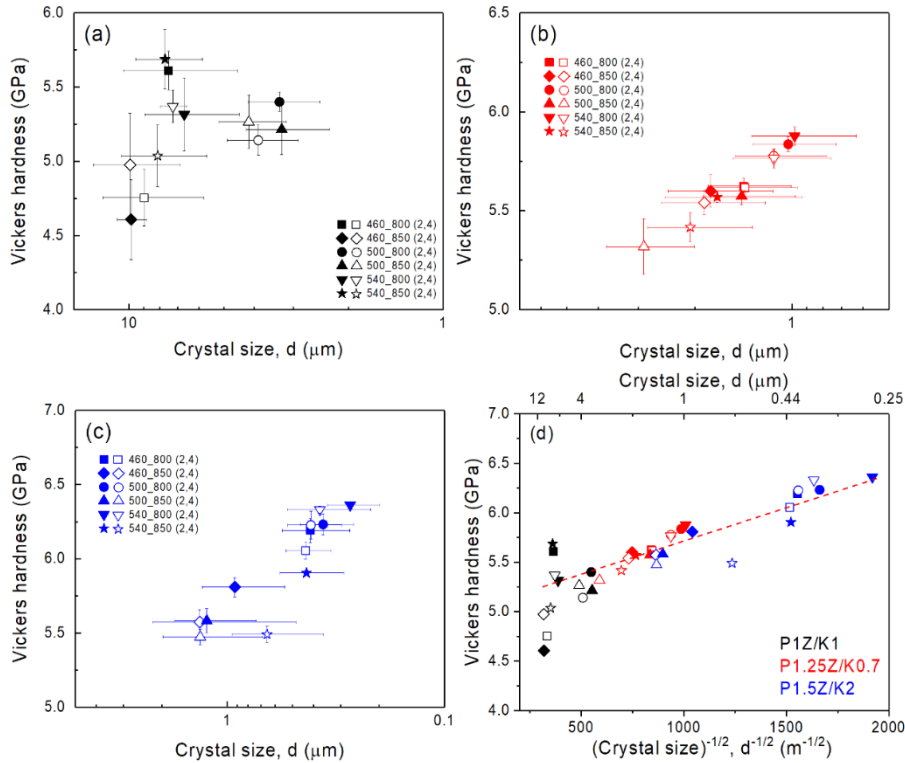
Fig. 4.5. Vickers hardness versus crystal size of samples (a) P1Z/K1, (b) P1.25Z/K0.7, (c) P1.5Z/K2, and (d) all data point in reciprocal of crystal size. Vertical and horizontal error bars represent standard deviations. The vertical and horizontal error bars were removed in (d) to easily differentiate each data point. The symbol was designated with the heat treatment conditions for nucleation (460, 500, 540 °C) for 1h and crystal growth (800, 850 °C) for 2 and 4 h. Closed symbols and opened symbols denote the holding times of 2 h and 4 h, respectively, at the growth stage. The red dash line in (d) is the linear regression line of Hall-Petch relation given by Eq. (10) for the P1.25Z/K0.7 and P1.5Z/K2 samples (R^2=0.858).
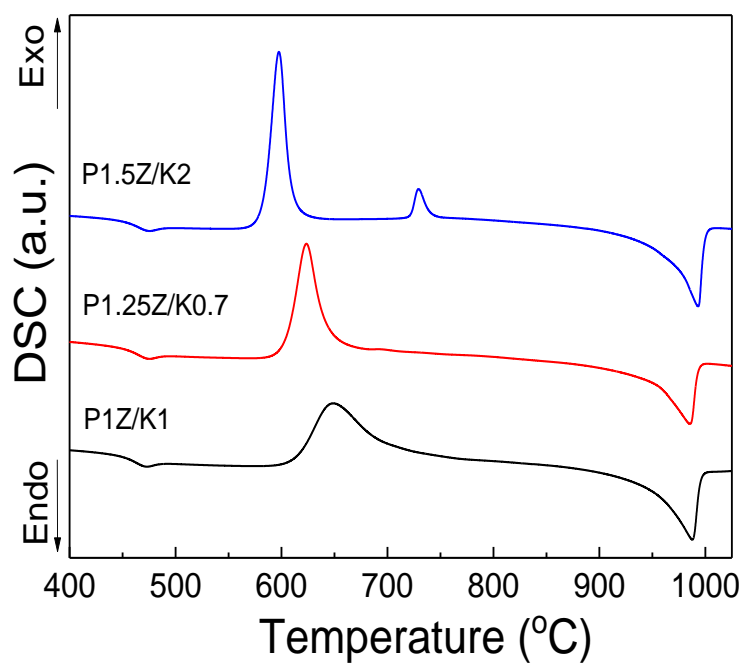
Fig. 4.6. DSC curves for glass samples with the heating rate 10°C/min in air.
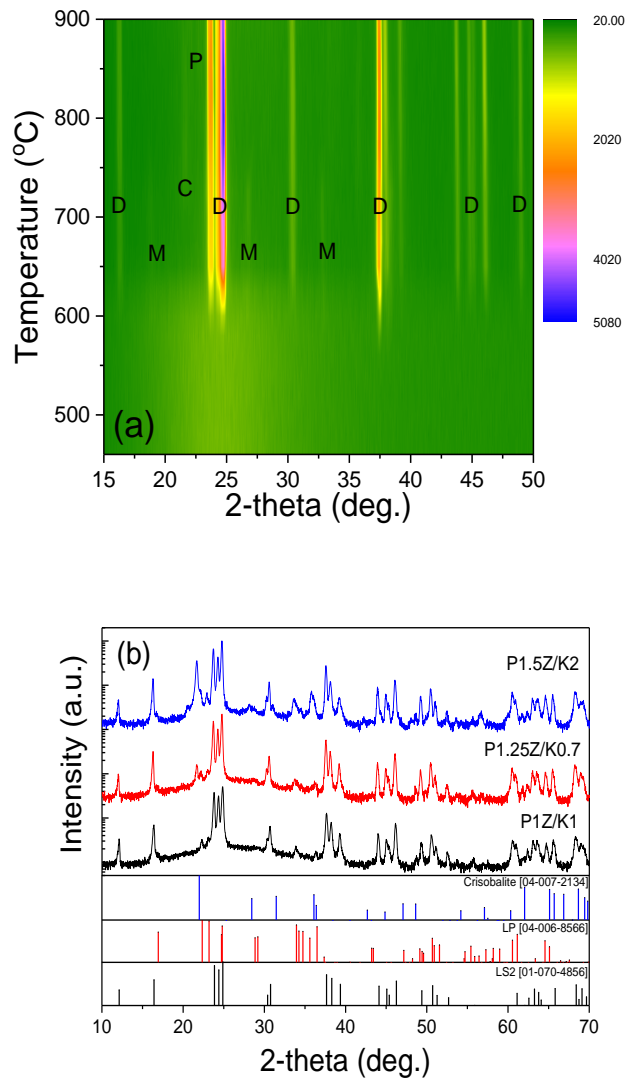
Fig. 4.7. (a) High-temperature XRD pattern for the P1Z/K1 glass sample where D and P denote LS2 and LP phase, respectively. (b) Room-temperature XRD patterns of the samples heat-treated at 500°C for 1 h and then 800°C for 2 h, (c) Quantitative phase analysis of GCs. ICDD PDF number of references: LS2 [01-070-4856], LP [04-006-8566], α-cristobalite [04-007-2134]
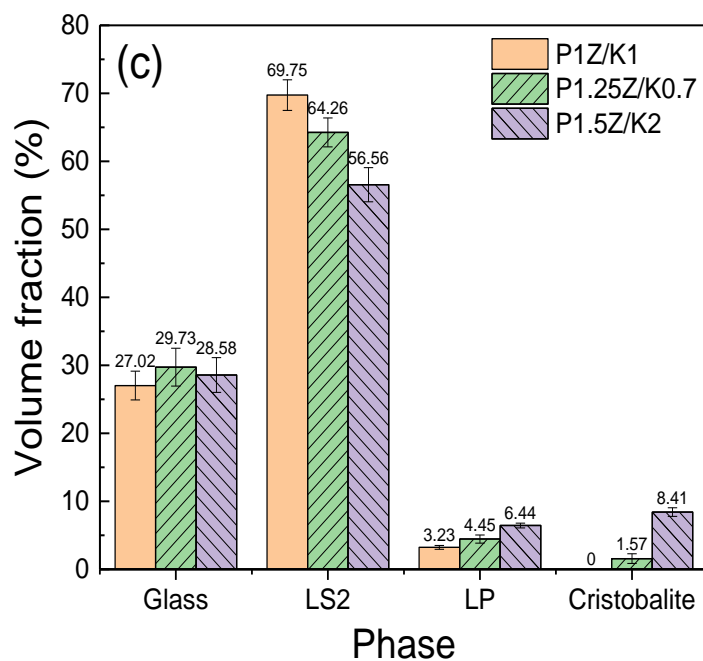
Fig. 4.7 (c) (continued)
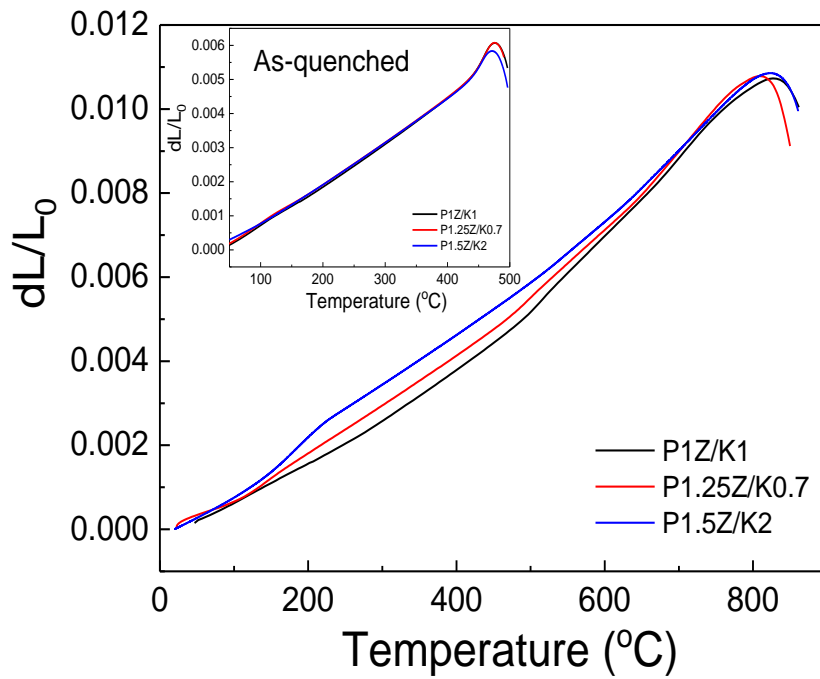
Fig. 4.8. Thermal expansion curves of GC samples heat treated at 500°C for 1 h and 800°C for 2 h The insets are the curves for corresponding glasses.
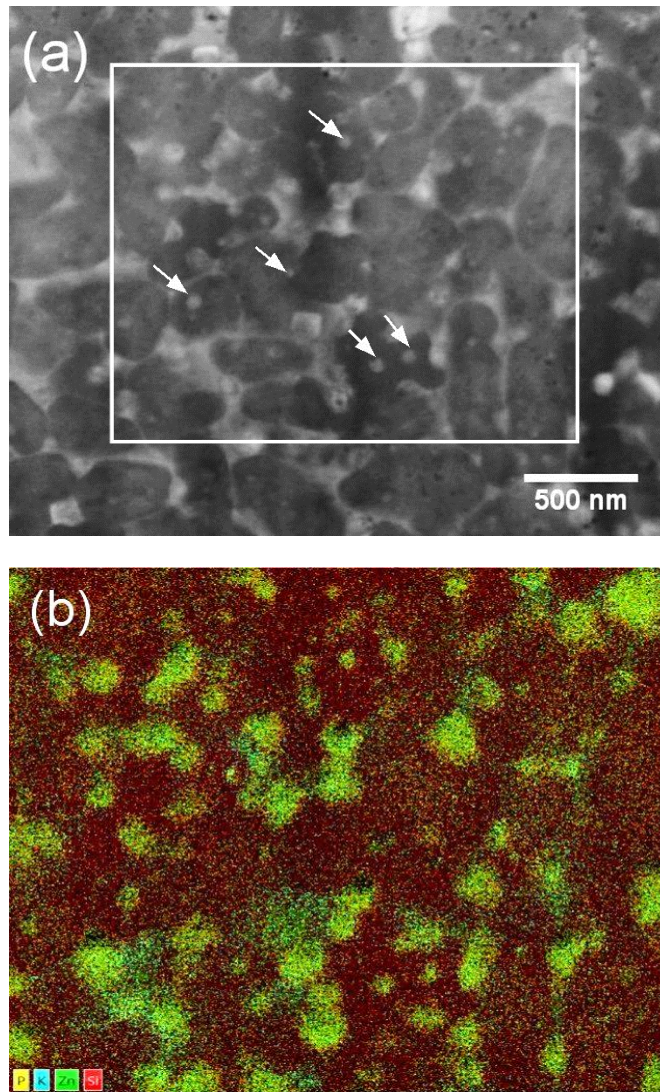
Fig. 4.9. TEM-EDS of (a) Electron image, (b) layered mapping for P (yellow), K (blue), Zn (green) and Si (red) elements. The arrows in (a) designate the LP phase.
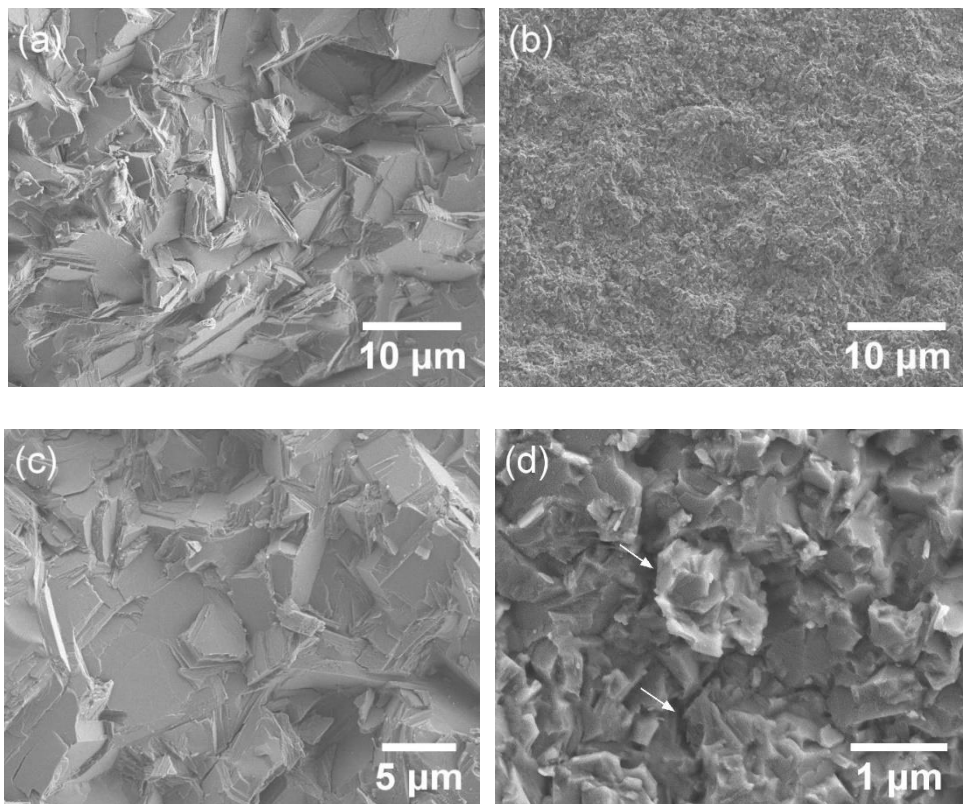
Fig. 4.10. SEM micrographs of the fracture surfaces for the GC samples after biaxial flexural test: (a) and (c) P1Z/K1, (b) and (d) P1.5Z/K2. The samples were heat-treated at 500ºC for 1 h and then 800ºC for 2 h.

References

[1] J.B. Wachtman, W.R. Cannon, M.J. Matthewson, Mechanical proper ties of ceramics, John Wiley & Sons, 2009.

[2] A.-M. Hu, K.-M. Liang, M. Li, D.-L. Mao, Effect of nucleation te mperatures and time on crystallization behavior and properties of Li_2O–Al_2O_3–SiO_2 glasses, Mater. Chem. Phys., 98 (2006) 430-433.

[3] A. Hu, M. Li, D. Mao, Growth behavior, morphology and properti es of lithium aluminosilicate glass ceramics with different amount of C aO, MgO and TiO_2 additive, Ceram. Int., 34 (2008) 1393-1397.

[4] M. Öveçoğlu, Microstructural characterization and physical propertie s of a slag-based glass-ceramic crystallized at 950 and 1100 ºC, J. Eu r. Ceram. Soc., 18 (1998) 161-168.

[5] M. Erol, S. Küçükbayrak, A. Ersoy-Mericboyu, M. Öveçoğlu, Cryst allization behaviour of glasses produced from fly ash, J. Eur. Ceram. S oc., 21 (2001) 2835-2841.

[6] R. Riedel, I.-W. Chen, Ceramics Science and Technology, Volume 1: Structures, John Wiley & Sons, 2015.

[7] V.R. Mastelaro, E.D. Zanotto, Anisotropic residual stresses in partia lly crystallized Li_2O–$2SiO_2$ glass-ceramics, J. Non-Cryst. Solids, 247 (1 999) 79-86.

[8] S. Freiman, L. Hench, Effect of Crystallization on the Mechanical Properties of Li_2O-SiO_2 Glass-Ceramics, J. Am. Ceram. Soc., 55 (1972) 86-90.

[9] W. Höland, G.H. Beall, Glass ceramic technology, 2nd ed ed., Joh n Wiley & Sons inc., New Jersey, 2012.

[10] S.C. von Clausbruch, M. Schweiger, W. Höland, V. Rheinberger, The effect of P_2O_5 on the crystallization and microstructure of glass-ce ramics in the SiO_2–Li_2O–K_2O–ZnO–P_2O_5 system, J. Non-Cryst. Solids, 263 (2000) 388-394.

[11] G. Wen, X. Zheng, L. Song, Effects of P_2O_5 and sintering tempe rature on microstructure and mechanical properties of lithium disilicate glass-ceramics, Acta Mater., 55 (2007) 3583-3591.

[12] F. Aumento, Stability lattice parameters and thermal expansion of beta-cristobalite, Am. Mineral., 51 (1966) 1167-&.

[13] L. Hallmann, P. Ulmer, M. Kern, Effect of microstructure on the mechanical properties of lithium disilicate glass-ceramics, Journal of the mechanical behavior of biomedical materials, 82 (2018) 355-370.

[14] D. Kim, H.-J. Kim, S.-I. Yoo, Effect of ZnO/K_2O ratio on the cr ystallization sequence and microstructure of lithium disilicate glass-cera mics, J. Eur. Ceram. Soc., 39 (2019) 5077-5085.

[15] A. Marotta, A. Buri, F. Branda, Nucleation in glass and differenti al thermal analysis, Journal of materials science, 16 (1981) 341-344.

[16] A. Ananthanarayanan, A. Dixit, R.K. Lenka, R.D. Purohit, V.K. S hrikhande, G.P. Kothiyal, Some studies on the phase formation and kin etics in TiO_2 containing lithium aluminum silicate glasses nucleated by P_2O_5, J. Therm. Anal. Calorim., 106 (2011) 839-844.

[17] O.I.d. Normalizacion, International Standard ISO 6872: Dentistry-c eramic Materials, ISO, 2008.

[18] R. Belli, M. Wendler, D. de Ligny, M.R. Cicconi, A. Petschelt, H. Peterlik, U.J.D.M. Lohbauer, Chairside CAD/CAM materials. Part 1: Measurement of elastic constants and microstructural characterization, 33 (2017) 84-98.

[19] A. Della Bona, K.J. Anusavice, P.H. DeHoff, Weibull analysis an d flexural strength of hot-pressed core and veneered ceramic structures, Dent. Mater., 19 (2003) 662-669.

[20] A. Della Bona, J.J. Mecholsky Jr, K.J. Anusavice, Fracture behavi or of lithia disilicate-and leucite-based ceramics, Dent. Mater., 20 (200 4) 956-962.

[21] J. Kübler, Fracture toughness of ceramics using the SEVNB meth

od; Round-Robin. VAMAS Report No. 37, ESIS Document D2–99, (1 999).

[22] I.C. Madsen, N.V. Scarlett, A. Kern, Description and survey of m ethodologies for the determination of amorphous content via X-ray po wder diffraction, Zeitschrift für Kristallographie Crystalline Materials, 2 26 (2011) 944-955.

[23] N.V. Scarlett, I.C. Madsen, Quantification of phases with partial o r no known crystal structures, Powder Diffr., 21 (2006) 278-284.

[24] D. Kim, H.-J. Kim, S.-I. Yoo, Effect of V_2O_5 colorant on the opt ical properties and crystallization behaviors of lithium disilicate glass-ce ramics, J. Alloys Compd., 836 (2020) 155333.

[25] Y. Iqbal, W. Lee, D. Holland, P. James, Crystal nucleation in P_2O_5-doped lithium disilicate glasses, Journal of materials science, 34 (19 99) 4399-4411.

[26] H.R. Fernandes, D.U. Tulyaganov, J.M.F. Ferreira, The role of P_2O_5, TiO_2 and ZrO_2 as nucleating agents on microstructure and crystalli zation behaviour of lithium disilicate-based glass, Journal of Materials Science, 48 (2012) 765-773.

[27] T. Headley, R. Loehman, Crystallization of a Glass-Ceramic by E pitaxial Growth, J. Am. Ceram. Soc., 67 (1984) 620-625.

[28] R. Rice, Ceramic tensile strength-grain size relations: grain sizes, slopes, and branch intersections, Journal of materials science, 32 (1997) 1673-1692.

[29] H. Ryou, J.W. Drazin, K.J. Wahl, S.B. Qadri, E.P. Gorzkowski, B.N. Feigelson, J.A. Wollmershauser, Below the Hall-Petch limit in na nocrystalline ceramics, ACS nano, 12 (2018) 3083-3094.

[30] S. Huang, Z. Huang, W. Gao, P. Cao, Trace phase formation, cry stallization kinetics and crystallographic evolution of a lithium disilicate glass probed by synchrotron XRD technique, Scientific reports, 5 (201 5) 9159.

[31] M.G. Mortuza, M.R. Ahsan, R. Dupree, D. Holland, Disproportion ation of Q_m ($0 \leq m \leq 4$) species in partially devitrified $Li_2Si_2O_5$ glasses with small amounts of P_2O_5, Journal of Materials Science, 42 (2007) 7 950-7955.

[32] C.S. Ray, Q. Yang, W.h. Huang, D.E. Day, Surface and internal crystallization in glasses as determined by differential thermal analysis, J. Am. Ceram. Soc., 79 (1996) 3155-3160.

[33] C.S. Ray, D.E. Day, An Analysis of Nucleation-Rate Type of Cur ves in Glass as Determined by Differential Thermal Analysis, J. Am. Ceram. Soc., 80 (1997) 3100-3108.

[34] D.E. Damby, E.W. Llewellin, C.J. Horwell, B.J. Williamson, J. N ajorka, G. Cressey, M. Carpenter, The α–β phase transition in volcanic cristobalite, J. Appl. Crystallogr., 47 (2014) 1205-1215.

[35] S. Dai, M.A. Rodriguez, J.J. Griego, Sealing Glass-Ceramics with Near Linear Thermal Strain, Part I: Process Development and Phase Id entification, J. Am. Ceram. Soc., 99 (2016) 3719-3725.

[36] A. Paul, Chemistry of glasses, Springer Science & Business Medi a, 1990.

[37] D.B. Peacor, High-temperature single-crystal study of the cristobali te inversion, Zeitschrift für Kristallographie-Crystalline Materials, 138 (1973) 274-298.

[38] R.C. Breneman, J.W. Halloran, Stress Development and Fracture o f Surface Nucleated Cristobalite on Silica Glass, J. Am. Ceram. Soc., 97 (2014) 3483-3488.

[39] M.O. Villas-Boas, F.C. Serbena, V.O. Soares, I. Mathias, E.D. Za notto, Residual stress effect on the fracture toughness of lithium disilic ate glass-ceramics, J. Am. Ceram. Soc., 103 (2020) 465-479.

[40] P. James, S. Keown, Study of crystallization in lithium silicate gl asses using high-voltage electron microscopy, Philos. Mag., 30 (1974) 789-802.

[41] W. Höland, E. Apel, C. van 't Hoen, V. Rheinberger, Studies of crystal phase formations in high-strength lithium disilicate glass–ceramics, J. Non-Cryst. Solids, 352 (2006) 4041-4050.

[42] F.C. Serbena, E.D. Zanotto, Internal residual stresses in glass-ceramics: A review, J. Non-Cryst. Solids, 358 (2012) 975-984.

[43] R.W. Rice, Mechanical properties of ceramics and composites: grain and particle effects, CRC Press, 2000.

[44] D. Li, J. Guo, X. Wang, S. Zhang, L. He, Effects of crystal size on the mechanical properties of a lithium disilicate glass-ceramic, Materials Science and Engineering: A, 669 (2016) 332-339.

[45] B.R. Lawn, R.F. Cook, Probing material properties with sharp indenters: a retrospective, Journal of Materials Science, 47 (2012) 1-22.

[46] A.-R. Alao, L. Yin, Nano-mechanical behaviour of lithium metasilicate glass–ceramic, Journal of the Mechanical Behavior of Biomedical Materials, 49 (2015) 162-174.

[47] C.M. Smith, D. Jiang, J. Gong, L. Yin, Determination of the mechanical behavior of lithium disilicate glass ceramics by nanoindentation & scanning probe microscopy, Mater. Chem. Phys., 148 (2014) 1036-1044.

[48] J. Pelleg, Mechanical properties of ceramics, Springer Science & Business, 2014.

[49] J. Swearengen, E. Beauchamp, R. Eagan, Fracture toughness of reinforced glasses, Crack Growth and Microstructure, (1978) 973-987.

[50] F. Serbena, I. Mathias, C. Foerster, E. Zanotto, Crystallization toughening of a model glass-ceramic, Acta Mater., 86 (2015) 216-228.

[51] T.J. Hill, J.J. Mecholsky, K.J. Anusavice, Fractal Analysis of Toughening Behavior in 3BaO. 5SiO₂ Glass-Ceramics, J. Am. Ceram. Soc., 83 (2000) 545-552.

[52] R. Belli, M. Wendler, M.R. Cicconi, D. de Ligny, A. Petschelt, K. Werbach, H. Peterlik, U. Lohbauer, Fracture anisotropy in texturized lithium disilicate glass-ceramics, J. Non-Cryst. Solids, 481 (2018) 457-469.

Chapter 5

Coloration mechanism in lithium disilicate glass-ceramics

5.1 Introduction

In this chapter, we investigated the effect of V_2O_5 colorant on the optical properties and crystallization of LS2 GCs. The V_2O_5 additive was selected as the colorant since it is known to impart a yellowish color (positive b*) to GCs with the combination of CeO_2 and TiO_2 [1]. In addition, to achieve a fine interlocking microstructure for high mechanical properties, additives are needed for crystallization. The P_2O_5 is a typical nucleating agent for LS2 GCs, and the glass modifier Al_2O_3 is known to promote crystallization of the LS phase, which is a transient phase of LS2, while ZnO is known to induce the LS2 phase directly [2-4]. These additives can affect the composition of the residual glassy matrix after crystallization. We anticipated that a continuous change in a local composition of the multicomponent LS2 system during crystallization would alter the valence state of the vanadium colorant ion and crystal field splitting in the residual glassy matrix, and thus affect the coloration. Therefore, we varied the ratio of additives for crystallization such as K_2O, ZnO, and Al_2O_3; both the ratios of Al_2O_3/K_2O (Al/K) and ZnO/K_2O (Zn/K) from 0.5 to 2, respectively. The

amounts of base glass matrix composed of Li_2O and SiO_2, and nucleating agent, P_2O_5, and oxide colorant, V_2O_5 were fixed to have 93.5, 1.5, and 0.5 mol%, respectively.

5.2 Experimental

The precursor materials were SiO_2 (99%, Daejung Chemical Co., Ltd, Korea), Li_2CO_3 (98%, Daejung Chemical Co., Ltd, Korea), $(NH_4)_2HPO_4$ (98.5%, Daejung, Korea), K_2CO_3 (99%, Kojundo Chemical Lab. Co., Ltd, Japan), ZnO (99%, Kojundo Chemical Lab. Co., Ltd, Japan), and V_2O_5 (99.9%, Kojundo Chemical Lab. Co., Ltd, Japan). The precursors were weighed to have the glass compositions listed in Table 5.1, mixed by 3D-mixer (Korea machine engineering, KMC-T2, Korea) for 30 min, and melted in a platinum crucible at 1400 °C for 2 h in air using an elevator furnace. The melts were poured into a crusher to obtain a glass frit. The glass frit was re-melted twice to improve its homogeneity at 1400 °C for 1 h, and then cast in a graphite mold with the diameter of 13 mm diameter and the thickness of 20 mm. As-cast glasses were annealed at 450 °C for 30 min to remove a residual stress. For the fabrication of GCs, the two-stage heat treatment was conducted for all samples at 500 °C for 1 h as the nucleation stage and at 600 °C, 700 °C, and 800 °C for 2 h as the growth stage.

The thermal characterization of glass crystallization was conducted with differential scanning calorimetry (DSC, SDT Q600, TA instruments, USA) using a Pt cell up to 1100 °C with the heating rate of 10 °C/min in air. The glass frits larger than 400 μm were used in order to prevent the effect of surface crystallization on the characteristic DSC temperatures, which can induce the shift of exothermic

crystallization peaks toward lower temperatures because of increased nucleation sites on the surface when the size of the glass is small [5]..

X-ray diffraction (XRD, D/max 2500, Rigaku, Japan) was carried out to analyze the crystalline phases with Cu Kα (λ = 1.5401 Å) produced at 40 kV and 100 mA. The scan range was from 10° to 80° with a step size of 0.02° and a scan speed of 5°/min. To monitor the crystallization sequence, high-temperature X-ray diffraction (HT-XRD, D/max 2500, Rigaku, Japan) with Cu Kα (λ = 1.5401 Å) radiation produced at 40 kV and 200 mA was also conducted. Monolithic glass samples with a dimension of 12 mm × 19 mm × 1.6 mm were used for HT-XRD analyses. Samples were initially heated to 460 °C with a heating rate of 20 °C/min and maintained for 5 min. HT-XRD analyses were performed at temperatures ranging from 460 to 600 °C at 20 °C intervals and 600 to 900 °C at 25 °C intervals with a 2θ scan from 10 to 50° with a scan speed of 2°/min.

The quantitative phase analysis using X-ray diffraction was performed by the Partial or No Known Crystal Structure (PONKCS) method. The fitting of the X-ray diffraction pattern was conducted by the software TOPAS (Bruker, version 4.2). The microstructures of GCs were observed using a field emission scanning electron microscope (FE-SEM, JSM6701F, Jeol, Japan) after etching samples in 15 vol% HF solution for 5-10 sec. The local compositions in the microstructures were analyzed by energy dispersive spectroscopy (EDS) equipped in a field emission transmission electron microscope (FE-TEM, JEM2100F, Jeol, Japan) operated at 200 kV. The TEM specimens were prepared by a focused ion beam (FIB, SII Nanotechnology, SMI3050E) system.

For optical analysis, glass and GC samples with the thickness of 1.2 mm were mirror-polished with a diamond suspension of 1 μm. The colors of the glass and GC samples were measured in the wavelength region of 380 – 780 nm by a UV-vis spectrometer (Shimadzu Corp, UV-2600, Japan) using CIE color coordination (CIE1976, illuminant D65, 10° Standard Observer function). Optical density was obtained from the ratio of absorbance relative to the sample thickness in the region of 220 – 1400 nm with a resolution of 0.5 nm. Commercial software (PeakFit, v4.12) was used for the Gaussian deconvolution of the absorption peaks. Photoluminescence spectra of samples were measured using a Xe flash lamp (PSI Co. Ltd, Korea) of 500W.

5.3 Results

5.3.1. Color analysis

Fig. 5.1 shows the photographs of the glass and GC samples. The V_2O_5-undoped $GZ_{1.5}$ glass and GC samples are transparent and colorless. The translucency decreases with increasing the growth temperature. While all the V_2O_5-doped glass samples are light greenish, the V_2O_5-doped GCs show diverse colors which are dependent on their glass composition and growth temperature. When the glass samples are heat-treated at 600 °C, $GVAl_{1.5}$, $GVAl_3$, and $GVZ_{1.5}$ are violet in color while GVZ_3 is bluish. The colors of $GVAl_{1.5}$ and $GVAl_3$ maintain violet with high translucency up to 700 °C while those of $GVZ_{1.5}$ and GVZ_3 reveal a bluish color with low translucency. When the glass is heat-treated at 800 °C, both $GVAl_{1.5}$ and $GVZ_{1.5}$ are greenish. However, $GVZ_{1.5}$ shows lower translucency than $GVAl_{1.5}$, and $GVAl_3$

is dark bluish. The brownish color of GVZ_3 is notably different from other samples. The color coordination for the samples based on CIELab color space are summarized in Table 5.2, where L* denotes lightness, the chromaticity parameter, a*, represents the green (negative) – red (positive) value, and the parameter b* indicates the blue (negative) – yellow (positive) value. The L* values of all samples are increased with the growth temperature, implying that the reflection of the incident light is enhanced by the crystallization. For $GVZ_{1.5}$ and GVZ_3, the b* values move to positive with increasing the growth temperature, and reach to 11.4 for GVZ_3 heat-treated at 800 °C. From the sample GVZ_3 heat-treated at 800 °C, the color appropriate for dental application is obtainable since it possesses L* of 62.2, a* of 0.6 and b* of 11.4.

5.3.2. Absorption and photoluminescence

The absorption spectra of all samples are represented in Fig. 5.2. All V_2O_5-doped glass samples reveal an intensive absorption in the UV region with UV cut-off at 365 nm. On the other hand, undoped glass exhibits lower UV absorption compared with V_2O_5-doped glasses as shown in Fig. 5.2(a). At the growth temperature of 600 °C, the absorption bands for $GVAl_{1.5}$ and $GVAl_3$ samples are observed at 17,600 and 10,300 cm^{-1}, and additional bands are detectable at 22,000 and 13,800 cm^{-1} in $GVZ_{1.5}$ and GVZ_3 as shown in Fig. 5.2(b). In Fig. 5.2(c), when the growth temperature is 700 °C, it is shown that the intensities of absorption bands at 22,000 and 17,600 cm^{-1} for $GVAl_3$ are increased compared with those for $GVAl_{1.5}$, Similarly, the intensities of absorption bands at 22,000, 17,600 and 13,800 cm^{-1} for GVZ_3 are higher than those for $GVZ_{1.5}$. At the growth temperature of 800 °C, the absorption bands at 17,600 and 10,300 cm^{-1} for both $GVAl_{1.5}$ and $GVAl_3$ are diminished while the

intensity of absorption band at 22,000 cm^{-1} is enhanced as shown in Fig. 5.2(d). For GVZ$_{1.5}$, the intensities of absorption bands at 17,600 and 13,800 cm^{-1} are unaltered. The intensity of absorption band at 22,000 cm^{-1} is, however, significantly increased for GVZ$_{1.5}$, and it is more significantly increased for GVZ$_3$.

The color of glass can be understood by the absorption bands generated by vanadium ions with specific oxidation states, and those absorption bands can be analyzed on the basis of the Tanabe-Sugano model [6]. Generally, the vanadium ions are known to exist as octahedrally coordinated V^{3+}, V^{4+}, and V^{5+} ions in oxide glass due to the ligand field of glass. The existence of V^{2+} ion in oxide glass is quite rare [7, 8]. Therefore, the possible vanadium ions in LS2 GCs are believed to be V^{3+}, V^{4+}, and V^{5+} ions. In the glass samples shown in Fig. 5.2(a), the broad absorption bands observed in the UV region and no additional absorption band beyond the UV region strongly support the charge transfer transition by V^{5+} ions which has no electrons in d shell, suggesting that all glass samples possess V^{5+} ions only regardless of the Al/K and Zn/K ratio.

The V^{4+} ion, having one electron in d shell, is known to have one absorption band from the ground state of $^3T_2$ to ^2E [9]. However, due to its ligand field of adjacent oxygen ions, the complex is tetragonally distorted, and its ground states are split into $^2B_2$ (ground) and ^2E, and ^2E states into $^2B_1$ and $^2A_1$, revealing three different absorption bands, respectively. The absorption bands from ground $^2B_2$ to $^2B_1$, ^2E, and $^2A_2$ are reported at 9,200, 16,400, and 23,800 cm^{-1}, respectively, in sodium silicate glass, and 9,600, 16,340, and 23,236 cm^{-1}, respectively, in sodium borosilicate glass [10, 11]. For the V^{3+} ion, having two electrons in d shell, it has three spin-allowed transitions from the ground $^3T_1$ (^3F) to $^3T_2$ (^3F), $^3T_1$ (^3P), and $^3A_2$ (^3F). The transition

from ground $^3T_1$ (^3F) to $^3T_2$ and $^3T_1$ were observed at 14,700 and 22,000 cm^{-1}, respectively, in sodium silicate glass, and 13,812 and 21,786 cm^{-1}, respectively, in zirconium fluoride glass, and 21,786 and 13,812 cm^{-1}, respectively, in phosphate glass [10, 12, 13]

Referring to previous reports [19-25], we could interpret the valency of vanadium ion in our samples. Deconvoluted absorption bands for the samples with distinct colors from violet, bluish, greenish, and brownish are represented in Fig. 5.3. As shown in Figs 5.3(a) and (b), the violet and bluish colors in GVAl$_3$ and GVZ$_3$ samples, respectively, possess mainly V^{4+} ion and relatively lower content of V^{3+} ion while the greenish color in GVAl$_{1.5}$ and GVZ$_{1.5}$ samples exhibits a decrease in V^{4+} ion but an increase in V^{3+} ion as shown in Fig. 5.3(c). It is noteworthy that, compared with the samples with relatively higher translucency grown at 600 °C, the samples with relatively lower translucency grown at 700 °C show higher optical densities even though their colors are identical as shown in Figs. 5.3(b) and (c), which might be ascribed to a light scattering from the crystalline phase which can enhance the extinction coefficient without altering the absorption bands. Finally, as shown in Fig. 5.3(d), the brownish color in GVZ$_3$ exhibits the largest content of V^{3+} ion among all samples with enhanced absorption intensities at 22,000 cm^{-1}. In addition, all GCs show a charge transfer in UV region, indicating the co-existence of V^{5+} with V^{3+} and V^{4+} ions. Consequently, while the light greenish color of as-quenched glass indicates the existence of the V^{5+} ion only, the violet and bluish colors of GCs indicate the existence of the V^{4+} ion primarily, and the brownish color of GCs indicates a large portion of the V^{3+}ion, implying that that the V^{5+} ion in as-quenched glass is first reduced into V^{4+} and then V^{3+} further with progressing crystallization.

The photoluminescence (PL) spectra of samples are presented in Figs. 5.4(a) and (b). We can see that there exist excitations in the wavelength region of 345 – 348 nm and broad emissions in the region of 505 – 515 nm. As mentioned previously it, the charge transfer occurs by the V^{5+} ion in the glass, showing intense absorption in UV region, and the absorbed energy through the charge transfer from V^{5+} to O^{2-} ligand is released at about 500 nm as a reverse radiative decay process [11, 14, 15]. Thus, the broad emission in the region of 505 – 515 nm is assumed be caused by the V^{5+} ion. The intensities of both excitation and emission PL spectra of GVAl$_{1.5}$ are increased with increasing the growth temperature as shown in Fig. 5.4(a). It is known that the PL spectra of a transition metal ion in glasses are very weak due to a non-radiative decay process, and they can be enhanced by doping the transition metal ion into a crystalline phase to promote a radiative decay [16]. Thus, the enhanced PL spectra imply that the V^{5+} ion can be doped to the crystalline phase of GCs. The PL spectra of the GC samples heat-treated at 800 °C, which show various colors of dark bluish, greenish and brownish, are illustrated in Fig. 5.4(b). The intensities of both excitation and emission PL spectra of GVAl$_3$ and GVZ$_3$ are lower than those of GVAl$_{1.5}$ and GVZ$_{1.5}$, suggesting that the green color of GVAl$_{1.5}$ and GVZ$_{1.5}$ heat-treated at 800 °C might be derived not only from the absorption but also from the photoluminescence with the maximum intensity in the wavelength region of 505-515 nm.

In Fig. 5.4(c), the maximum intensities of PL excitation spectra at ~350 nm are plotted as a function of the heat treatment temperature. It is obvious that the maximum intensities are increased with increasing the growth temperature for all samples except the intensity drop of GVZ$_3$ at 800 °C. This intensity drop is attributable to a decrease in the amount of V^{5+} ion doped to the crystalline phase of

GCs. In addition, the intensities of PL emission spectra of GVAl$_3$ and GVZ$_3$ are lower than those of GVAl$_{1.5}$ and GVZ$_{1.5}$, suggesting that, as the Al/K and Zn/K ratios become higher, the doping content of V^{5+} ion to glass or crystalline phase becomes lower, clearly indicating that the ratios of Al/K and Zn/K additives affect the extent of fluorescence by controlling the doping content of V^{5+} ion to glass or crystalline phase.

5.3.3. Crystallization behavior

As previously mentioned, the LS2 GCs are fabricated by the molding/pressing process or CAD/CAM technique. Particularly, the GC composed of the LS phase and residual glass, normally formed at relatively lower growth temperature (~ 600 °C in general), is currently adapted as a machinable CAD/CAM block. After milling the block to have an aimed shape, the LS phase is converted into the LS2 phase which is stable at higher growth temperature of ~850 °C. If the V$_2$O$_5$ colorant assists to form the LS phase rather than the LS2 phase at relatively lower growth temperature, it can be used for CAD/CAM process. Oppositely, if it assists to the formation of the LS2 phase rather than the LS phase, the LS2 GCs with the V$_2$O$_5$ colorant should be shaped by the molding/pressing process. In addition, it may change the resultant microstructures of GCs, affecting optical and mechanical properties. Thus, it is essential to identify the effect of V$_2$O$_5$ colorant on the crystallization behavior.

Fig. 5.5 shows the DSC curves of all glass samples. Two exothermic peaks are observable in all samples except GVZ$_{1.5}$ having a shoulder peak. The characteristic DSC temperatures are listed in Table 5.3. The T$_g$, T$_{x2}$ and T$_m$ values of GVAl$_{1.5}$ are

similar to those of $GVAl_3$ except T_{x1} which is 25 °C higher than that of $GVAl_3$, implying that crystallization is promoted with increasing the ratio of Al/K at lower growth temperature below 600 °C. Similarly, the T_{x1} value of $GVZ_{1.5}$ is 10 °C higher than that of GVZ_3. However, its T_{x2} value is 36 °C lower than GVZ_3. In the previous chapter 3 [3], V_2O_5-undoped $GZ_{1.5}$ (with sample ID of Z/K0.5) showed three different exothermic peaks corresponding to the crystallization of LS and LS2 phases, that of cristobalite, and solid state reaction between LS and cristobalite phases, respectively. The third exothermic peak moved to lower temperature might result in the shoulder peak for $GVZ_{1.5}$, suggesting that V_2O_5 promotes the solid state reaction between LS and SiO_2 phase in lower temperature.

The crystallization sequence is the reaction sequence of the whole crystallization path which might include a metastable phase or secondary phase, affecting the nucleation or growth rate of a stable phase and also final microstructure. The LS2 GCs are known to have three different types of crystallization sequence, including the metastable LS phase in the early crystallization stage at relatively lower temperature which can disappear by reaction with SiO_2 to form the LS2 phase at higher temperature [17]. To investigate the effect of V_2O_5 on crystallization sequence, the HT-XRD analyses were carried out for $GVAl_{1.5}$ and GVZ_3 as shown in Fig. 5.6.

The color bar displays the X-ray diffraction intensity. For $GVAl_{1.5}$, the LS phase is crystallized in the early stage, followed by the formation of both cristobalite and LS2 phases at higher temperature. The XRD intensity of the LS2 phase is increased while those of the LS and cristobalite phases disappear at high temperatures over 780 °C, indicative of a type II crystallization sequence [17-19]. On the other hand, for GVZ_3, Both the LS and LS2 phases are crystallized simultaneously in the early

crystallization stage, and the diffraction intensities of the LS2 phase are aggressively increased as the LS phase is dissolved and the cristobalite phase emerges, indicating the type I crystallization sequence. In the final step, the intensity of cristobalite phase decreases with the formation of the quartz phase at ~ 850 °C. In the previous chapter 3 [3], V_2O_5-undoped GZ_3 showed relatively higher XRD intensity of the LS2 phase in the early crystallization stage than V_2O_5-doped GVZ_3, suggesting that 0.5 mol% of V_2O_5 addition tends to induce the LS phase rather than the LS2 phase, and hinder type I crystallization sequence. Although not presented here, V_2O_5-undoped $GAl_{1.5}$ showed type II crystallization sequence, implying that the effect of V_2O_5 colorant on type II crystallization sequence is negligible.

In addition, it is noteworthy that the $GVAl_{1.5}$ sample shows the LS phase in the early crystallization stage with the highest (111) diffraction peak located at 26.9° as shown in Fig. 6(a). On the other hand, the GVZ_3 sample presents the suppression of the maximum (111) main peak and the second peak of (200), resulting in the third peak of (310) as the main peak of LS phase, as shown in Fig. 6(b). In the previous chapter 3 [3], the Zn^{2+} ion (0.6 Å) might substitute the Li^+ ion (0.59 Å) together with a formation of vacancy to maintain the electrical charge neutrality. However, the Al^{3+} (0.39 Å) ion may not be incorporated into the LS crystalline phase.

Fig. 5.7 shows the XRD patterns of the samples which were nucleated at 500 °C for 1 h and subsequently raised to 600, 700, and 800 °C for 2 h. The LS phase is observed for $GVAl_{1.5}$ and $GVAl_3$ samples heat-treated at 600 and 700 °C. A small peak of the LS2 phase is detectable in $GVAl_3$ at 700 °C. At 800 °C, the LS2 and lithium phosphate (LP) phases are observed for $GVAl_{1.5}$ whereas a considerable quartz peak is observed in $GVAl_3$ along with the LS2 and LP phases. On the other

hand, the LS and LS2 phases are simultaneously crystallized at 600 °C for $GVZ_{1.5}$ and GVZ_3 as shown in Figs. 5.7(c) and (d), respectively. At 700 °C, the LS phase disappears, the LS2 phase is dominant, and also the cristobalite phase is formed.

Interestingly, the cristobalite phase survives after the solid state reaction at 800 °C in $GVZ_{1.5}$ while the quartz phase is remarkably pronounced in GVZ_3. As it can be seen in Fig. 5.7(b), the cristobalite phase is detectable for GVZ_3 in the temperature range from 750 to 900 °C, and its XRD intensity starts to decrease with the formation of quartz above 830 ºC, suggesting that the residual glassy phase or cristobalite phase transform to the stable quartz phase in the temperature above 800 °C with increasing the ratio of Al/K and Zn/K.

The quantitative phase analyses are presented in Table 5.4. With increasing the growth temperature, the volume fraction of residual glassy phase decreased and the that of LS2, LP, cristobalite and quartz phases increased. The cristobalite phase is found in $GVZ_{1.5}$ and GVZ_3 samples heat-treated at 600 and 700 °C, the while the quartz phase is detectable in GVZ_3 and $GVAl_3$ sample heat-treated at 800 °C. Interestingly, the GVZ_3 heat-treated at 800 ºC shows the smallest volume fraction of residual glassy phase among the samples.

5.3.4. Microstructures

The microstructures of the GCs after etching the residual glassy matrix are presented in Fig. 5.8. In Figs. 5.8 (a), (b) and (d), (e), nano-sized LS phase can be observed for the $GVAl_{1.5}$ and $GVAl_3$ samples, respectively, after the growth stage at 600 and 700 °C. When heat-treated at 800 °C, the acicular LS2 phase with the length

below 1 μm is observed for GVAl$_{1.5}$ in Fig. 5.8(c) while the tens-of-nanometers LS2 of irregular shape is observed for GVAl$_3$ in Fig. 5.8(f). For the GVZ$_{1.5}$ and GVZ$_3$ samples, the nano-sized LS2 phase is observed at the growth temperature of 600 °C in Figs. 5.8 (g) and (j), respectively, and it grows into the size of hundreds-of-nanometers at 700 °C as shown in Figs. 5.8 (h) and (k). At 800 °C, GVZ$_{1.5}$ is composed of acicular crystals with the length of ~1 μm in Fig. 5.8 (i). Compared with previous chapter 3 [22] on V$_2$O$_5$-undoped GZ$_{1.5}$ (with sample ID of Z/K0.5) and GZ$_3$ (Z/K2) having the LS2 crystal sizes of ~500 nm and ~300 nm, respectively, V$_2$O$_5$-doped samples of this study exhibit much larger size, suggesting that the addition of V$_2$O$_5$ colorant increases the growth rate of LS2 crystalline phase.

It is known that the maximum light scattering occurs when the grain size is close to the wavelength of incident light, and the light scattering decreases if it becomes smaller than the wavelength of the incident light [20]. In addition, the difference in refractive index between crystalline and glassy phases is the source of the light scattering at the phase boundary of crystal and glass. The refractive indices of the LS2 phase and matrix glass are known to be 1.55 and 1.5, respectively [1]. If the additives are located only at the residual glassy phase, it may be possible to increase the refractive index of residual glassy phase to match the refractive index of the LS2 phase, resulting in a reduced light scattering. Hence, the reason for high translucency in the GVAl$_{1.5}$ and GVAl$_3$ samples heat-treated at 600, 700 and 800 °C is ascribable to the nano-sized crystalline phase with the grain sizes smaller than the wavelength of visible light, and also to the minimal mismatch of refractive index between crystalline phase and residual glassy phase. On the other hand, although the GVZ$_{1.5}$ and GVZ$_3$ samples heat-treated at 700 °C reveal the crystal size of hundreds-of-nanometers, it is less translucent than the GVAl$_{1.5}$ and GVAl$_3$ samples heat-treated at

800 °C, suggesting that ZnO may be less effective for minimizing the mismatch of refractive index between crystalline phase and glassy phase compared with Al_2O_3, leading to lower translucency. However, for dental application, the translucency evaluated with lightness L* should be close to natural teeth with L* (67.6 ±7.0), and hence ZnO is favored for the appropriate translucency.

5.4 Discussion

5.4.1. The origin for the formation of different colors in GCs

While the color of glasses in all V_2O_5-doped samples is light greenish, the color of GCs is remarkably affected by the growth temperature as shown in Fig. 5.1. In particular, with increasing the growth temperature, the light greenish color of glasses changes continuously to violet, bluish, greenish, and brownish colors of GCs, which is attributable to a significant difference in relative proportions of V^{3+}, V^{4+} and V^{5+} ions existing in each sample. Also, the PL emission spectra at ~500 nm (green) are improved with increasing the growth temperature, suggesting the existence of V^{5+} ions in crystalline phase, and their intensities are higher in the samples with lower ratios of Al/K and Zn/K (= 0.5) compared with those with higher Al/K and Zn/K ratios (= 2). Therefore, it is important to identify the valence sates of vanadium and their locations in order to understand absorption and photoluminescence properties of samples

To identify the exact location of vanadium ions in the GCs, TEM analyses were conducted on the GVZ_3 sample grown at 800 °C as a representative of all samples. Fig. 5.9 shows the TEM micrographs and selected area diffraction patterns of this

sample. As shown in Figs. 5.9(b) and (c), the sample consists of a crystalline phase and a residual glassy matrix, respectively. The TEM-EDS point analysis data and compositional mapping are presented in Table 5.4 and Fig. 5.10, respectively. The point spectra of 1 and 4 are considered to originate from the LS2 and SiO_2 phases, respectively. From the point 1 spectrum for the LS2 phase in Fig. 5.10 (a), not only the P and K elements were detected from the additional additives of P_2O_5 and K_2O but also a small amount of V element from V_2O_5 colorant was detectable as listed in Table 5.4. From the point 4 spectrum for the SiO_2 phases of quartz and cristobalite, a very small amount of V was detected in Table 5.4. The small amount of V doped to the crystalline LS2 and SiO_2 phases can account for an increase in the PL emission spectra at $\sim$ 500 nm with progressing crystallization, where the V^{5+} ions (0.355 Å) are assumed to substitute the Si^{4+} (0.26 Å) sites either in the LS2 phase or the SiO_2 phases. The possible substitution of vanadium ion for the Si^{4+} site has been suggested on the basis of the X-ray diffraction and X-ray absorption near edge structure by Paszkowicz *et al.* [21], and the vanadium ion was expected to be V^{4+} although higher valence state was not completely excluded. In our samples, the small amount of V^{5+} ion might substitute the Si^{4+} site in LS2 or SiO_2 phases which is evidenced by the increase in the PL emission spectra at $\sim$ 500 nm.

On the other hand, much larger amounts of V are distributed in the residual glassy phases (spectrum points of 2, 3, 5 and 6 in Fig. 5.9) compared with those in crystalline phases as shown in Table 5.5. In addition, EDS-mapping image shows that the P, K, and Zn elements are distributed inhomogeneously in the residual glassy phases and LP phase with the size of $\sim$ 100 nm (where phosphorus is green color) is detectable as shown in Fig. 5.10(d). As the crystallization progresses, these additives for crystallization are ejected by newly grown LS2 crystalline phase unless those

have a sufficient solubility in the LS2 phase. This local compositional gradient in the residual glassy matrix may lead to a variation in the valence states of vanadium ion or crystal field splitting, resulting in various absorption bands including spin-forbidden band. The spin-forbidden band can appear when a strong distortion occurs by the adjacent cation which affects the charge density of oxygen ligands. According to Angell *et al*. [22, 23], the presence of cations of high polarizing power such as Zn^{2+} and Mg^{2+} favors a distortion of $[NiCl_4]$ group from tetrahedrality in molten KCl-$ZnCl_2$ mixtures and $MgCl_2$-H_2O solutions, respectively. Therefore, the strong distortion due to high content of Zn^{2+} ion in residual glassy might cause the spin-forbidden bands of V^{3+} ion which is responsible for main absorption bands of the brownish color in GVZ_3 sample. Furthermore, Morimoto *et al.* [24] also reported a drastic color change from emerald green to deep pink during crystallization of LS GCs with Cr_2O_3 colorant. While the valence state of Cr^{3+} ion was not varied with progressing crystallization, the absorption intensity in GCs was significantly enhanced, and the several spin-forbidden bands were appeared. They suggested that one Cr^{3+} ion replaces the three Li^+ ions in the LS crystal lattice, which might cause a large distortion of octahedral symmetry in the ligand polyhedral of Cr^{3+} leading to spin-forbidden transition. Unlike their report, in our study, the vanadium ion is expected to have various valence states with progressing crystallization of LS2 GCs, and the amount of V doped to LS2 or SiO_2 phases is much lower compared with than remaining in the residual glassy phase.

The concept of the optical basicity of glass, firstly proposed by Duffy *et al.* [25, 26] provides information on the electron donation power of glass matrix. If the optical basicity of the surrounding glass matrix consistently changes with progressing crystallization, the valence states of vanadium ions will be affected. It

is, however, very difficult to accurately estimate the optical basicity of the residual glassy matrix after crystallization because of its compositional fluctuation, and thus further study is required for better understanding. Instead, we suggest a qualitative explanation for the vanadium reduction as follows. Generally, the increase of basicity by addition of alkali oxide in glass cause the redox ion into higher oxidation state [27]. If both SiO_2 and Li_2O are consumed to transform into LS and/or LS2 phases, and both Li_2O and P_2O_5 are used to form LP phase, cristobalite or quartz phase are formed in the residual glassy phase. Therefore, the concentration of oxides such as K_2O, ZnO, and Al_2O_3 together with V_2O_5 is increased in the residual glassy phase, and the proportion of alkali oxide is decreased relatively because of the consumption of Li_2O, which is considered to cause the reduction of vanadium ion.

5.4.2. Effect of the V_2O_5 colorant on the crystallization behaviors of glasses

The V_2O_5 colorant turned out to assist the crystallization sequence type II which is appropriate for the CAD/CAM technique. Also, the quartz phase was formed in the samples with the Al/K and Zn/K ratios of 2 when they were heat-treated at 800 ℃. The size of LS2 and SiO_2 phase in GCs with the V_2O_5 colorant was found to increase. Therefore, one can see that the V_2O_5 colorant affects not only the optical properties of GCs but also their crystallization behaviors, significantly influencing their microstructures and mechanical properties.

The nucleation rate can be estimated by the inverse temperature of DSC exothermic peak, T_p^{-1}, which is proportional to density of nuclei. Compared with previous report [3] for the V_2O_5-undoped samples, it can be seen that the T_p^{-1} values

of undoped $GZ_{1.5}$ (1.65) and GZ_3 (1.67) are increased in V_2O_5-doped $GVZ_{1.5}$ (1.73) and GVZ_3 (1.76), suggesting that the nucleation rate was enhanced by the V_2O_5 addition. When the V_2O_5 is assumed as a glass network former in silicate, the V^{5+} ion has relatively high ionic field strength value (z/a^2=2.04, with coordination number of IV) similar to P^{5+} ion (2.1) and contains the additional positive charge compared with neighboring Si^{4+} ion (1.57) [28]. It may induce a significant distortion in Si-O-Si bond and lead to the phase separation to reduce the free energy [29]. The phase separation caused by V_2O_5 were also reported in Li_2O-SiO_2 glass [30], Na_2O-B_2O_3-SiO_2 glass [31] and cordierite glass-ceramics [32]. The nuclei are analyzed to be LS rather than LS2 phase in the GVZ_3 sample since the diminished LS2 peak in early crystallization stage is detectable in HT-XRD (Fig. 5.6(b)) compared with previous reported V_2O_5-undoped GZ_3 sample [3]. This means that the crystallization sequence type I gradually changes to type II with V_2O_5 addition in $GVZ_{1.5}$ and GVZ_3 samples while type II maintains in $GVAl_{1.5}$ and $GVAl_3$ samples. Further, the T_p^{-1} value of $GVAl_3$ (1.83) is the highest among all samples indicating the highest nucleation rate of the LS phase. However, the size of LS2 and SiO_2 phase increased with the V_2O_5 addition when they were heat-treated at 800 ºC. It is attributable to the enhanced growth rate by V_2O_5, which is in good agreement with the fact that V_2O_5 is likely to form a very fluid melt [33], implying that the viscosity of glass is lowered so that the crystal growth rate can be enhanced. Similarly, in our samples grown at 800 °C for 2 h, 0.5 mol% V_2O_5 addition to the $GVZ_{1.5}$ and GVZ_3 samples resulted in larger LS2 crystal size (~ 1 μm) compared with its size below 500 nm for the samples without the addition of V_2O_5, supporting that V_2O_5 might enhance the growth rates of the LS2 phase.

However, in $GVAl_{1.5}$ and $GVAl_3$ samples exhibit relatively smaller crystal size

than $GVZ_{1.5}$ and GVZ_3 samples suggesting that Al_2O_3 causes higher viscosity of glass matrix than ZnO and also accompanies the high nucleation rate, leading to impingement of the crystal. Therefore, for the matching with natural teeth of L* by increasing the incident light scattering, the nucleation rate of the LS and/or LS2 phase should be moderate, and the growth rate of LS2 must be enhanced to reach its crystal size of ~ 1 μm.

5.5 Summary

All glass samples were greenish, and they possessed only V^{5+} ions regardless of the Al/K and Zn/K ratios. With increasing the growth temperature, the contents of V^{4+} and V^{3+} ions were increased while the content of V^{5+} ion was monotonously reduced, which caused continuous change from light-greenish color of glass samples to violet, bluish, greenish and brownish colors of GCs. With progressing crystallization, while most of vanadium ions were inhomogeneously distributed in the residual glassy matrix of GCs, a small amount of V^{5+} ion (less than 0.02 mol%) was doped to the crystalline phases of LS2 and SiO_2, which induced the greenish fluorescence. In particular, the brownish color of the GVZ_3 (Zn/K of 2) sample heat-treated at 800 °C, which is desirable for dental application, possessed a* of 0.6 and b* of 11.4. Those color could be obtained by increasing the amount of V^{3+} ion in the residual glass matrix of GCs, where the high polarizing power of Zn^{2+} ion caused the distortion of ligand polyhedral of V^{3+} ion, resulting in the spin-forbidden bands.

The V_2O_5 colorant gradually changed from the crystallization sequence of type I (LS+LS2) to that of type II (LS) in the $GVZ_{1.5}$ and GVZ_3 samples, and the type II was maintained in $GVAl_{1.5}$ and $GVAl_3$ samples. The nucleation rate of the LS phase

in both ZnO– and Al_2O_3–containing samples was enhanced by the addition of V_2O_5 because of amorphous phase separation. At the growth temperature of 800 °C. the growth rate of LS2 increased by lowering the viscosity of the glass matrix, and thus the LS2 crystal size for the $GVZ_{1.5}$ and GVZ_3 samples became larger (~ 1 μm) compared with its size below 500 nm for the samples without the addition of V_2O_5. On the other hand, the $GVAl_{1.5}$ and $GVAl_3$ samples exhibited smaller LS2 size (< 1 μm) than $GVZ_{1.5}$ and GVZ_3 samples due to higher nucleation rate of LS and lower growth rate of LS2, leading to undesirable higher translucency for the dental application. The translucency appropriate for dental application was achievable by the addition of ZnO (in GVZ_3) rather than Al_2O_3 due to the LS2 crystal size of ~1 μm at 800 °C with and mismatch of refractive index between crystalline phase and residual glassy matrix.

Table 5.1. Nominal compositions (in mol%) of the glass samples.

Sample ID	SiO_2	Li_2O	P_2O_5	K_2O	Al_2O_3	ZnO	V_2O_5
$GVAl_{1.5}$	65.92	27.58	1.5	3	1.5	0	0.5
$GVAl_3$	65.92	27.58	1.5	1.5	3	0	0.5
$GVZ_{1.5}$	65.92	27.58	1.5	3	0	1.5	0.5
GVZ_3	65.92	27.58	1.5	1.5	0	3	0.5

Table 5.2. CIElab chromaticity values of L*, a* and b* of the samples where L* denotes lightness, the chromaticity parameter, a*, represents the green (negative) – red (positive) value, and the parameter b* indicates the blue (negative) – yellow (positive) value.

Sample ID	Heat treatment conditions	*L**	*a**	*b**
GVAl$_{1.5}$	As-quenched	29.82	0.42	1.07
	600 °C	10.48	3.17	-13.13
	700 °C	34.37	6.67	-25.02
	800 °C	53.25	-8.63	-12.40
GVAl$_3$	As-quenched	23.24	-1.12	-2.40
	600 °C	16.46	1.86	-4.84
	700 °C	27.81	3.72	-13.11
	800 °C	44.87	-4.85	-11.88
GVZ$_{1.5}$	As-quenched	27.5	-1.64	-1.34
	600 °C	38.46	1.93	-34.76
	700 °C	55.08	-8.40	-21.08
	800 °C	71.65	-6.43	3.69
GVZ$_3$	As-quenched	14.55	-0.88	-2.09
	600 °C	25.63	0.82	-16.24
	700 °C	55.14	-7.29	-20.85
	800 °C	62.17	-0.46	11.40

Table 5.3. Characteristic temperatures analyzed by DSC. T_g is the glass transition temperature, T_p^{-1} is the inverse temperature of the first exothermic peak, T_{x1} is the onset temperature of the first exothermic peak, T_{x2} is the onset of the second exothermic peak, and T_m is the melting peak temperature.

Sample ID	T_g (°C)	T_{x1} (°C)	T_p^{-1} ($\times 10^{-3}$/°C)	T_{x2} (°C)	T_m (°C)
GVAl$_{1.5}$	470.2	572.3	1.75	780.3	979.1
GVAl$_3$	473.7	547.9	1.83	777.2	976.7
GVZ$_{1.5}$	465.7	576.9	1.73	676.5	974.8
GVZ$_3$	458.3	567.6	1.76	712.3	986.5

Table 5.4. Calculated volume fraction of residual glassy and crystalline phase with growth temperature based on Partial Or No Known Crystal Structure (PONKCS) method.

Sample	Growth Temp. (°C)	Glass	LS	LS2	LP	Cristobalite	Quartz
GVZ$_{1.5}$	600	62.57 ± 2.87	24.41 ±1.92	13.02 ± 0.90	0	0	0
	700	30.74 ± 0.32	0	60.31 ± 1.46	6.24 ± 0.19	2.71 ± 1.58	0
	800	29.03 ± 0.37	0	59.63±0.18	6.71±0.15	4.62±0.21	0
GVZ$_3$	600	67.57 ± 1.77	18.41 ± 0.44	14.01 ± 1.32	0	0	0
	700	19.57 ± 1.09	0	66.71 ± 1.08	6.51 ± 0.45	7.21 ± 1.80	0
	800	16.08 ± 3.79	0	60.03 ± 2.71	6.82 ± 0.21	1.40 ± 0.40	15.66 ± 0.82
GVAl$_{1.5}$	600	71.76 ± 0.04	28.24 ± 0.01	0	0	0	0
	700	69.41 ±4.59	27.86 ± 3.77	2.73 ± 1.86	0	0	0
	800	36.02 ±2.12	0	58.03 ± 2.02	5.94 ±0.31	0	0
GVAl$_3$	600	77.28 ±0.56	22.72 ± 0.55	0	0	0	0
	700	74.91 ±0.90	22.46 ± 0.48	2.63 ± 1.38	0	0	0
	800	28.25 ±0.91	0	53.25 ± 0.36	5.76 ± 0.47	0	12.74 ± 1.01

Table 5.5. Compositional analyses of the GVZ$_3$ sample heat-treated at 800 ℃ by TEM-EDS.

Spectrum points	1	2	3	4	5	6
O	70.66	69.71	82.27	68.53	75.38	67.89
Si	29.26	28.66	15.08	31.43	23.15	30.54
P	0.03	1.49	2.02	0.01	1.2	0.41
K	0.03	0.05	0.2	0.00	0.1	0.6
Zn	0.00	0.00	0.00	0.02	0.05	0.34
V	0.02	0.1	0.44	0.01	0.12	0.22
Predicted phase	LS2	glass	glass	SiO$_2$	glass	glass

Fig. 5.1. Photographs of glass and glass-ceramics samples. The first column of left side are glass samples and the right side are GCs samples with the growth temperature.
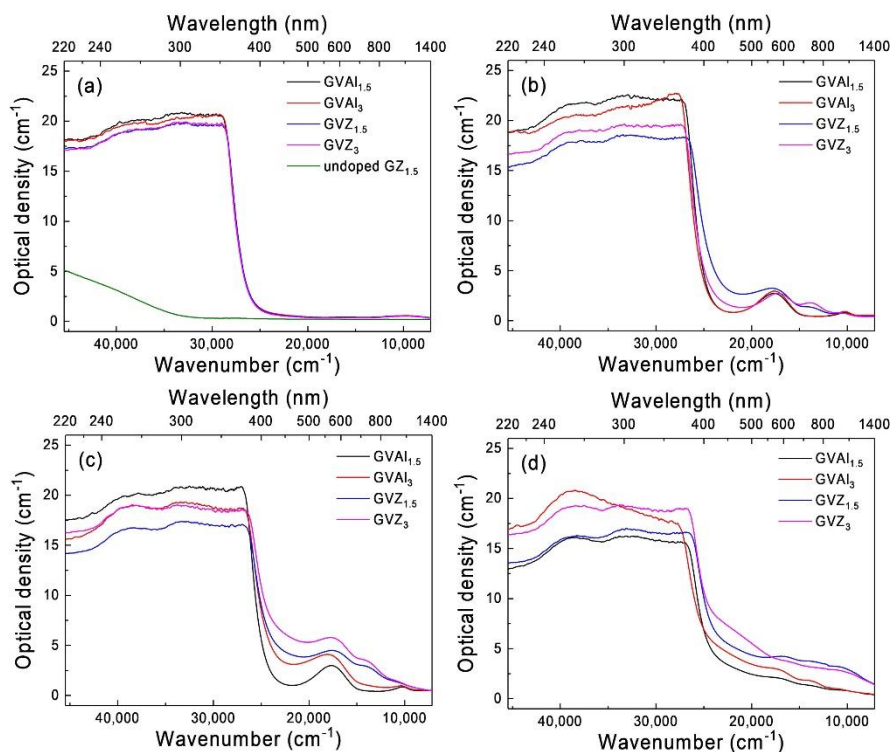
Fig. 5.2. Optical densities as a function of wavenumber for the samples (a) as-quenched and heat treated at (b) 600 ℃, (c) 700 ℃ and (d) 800 ℃.
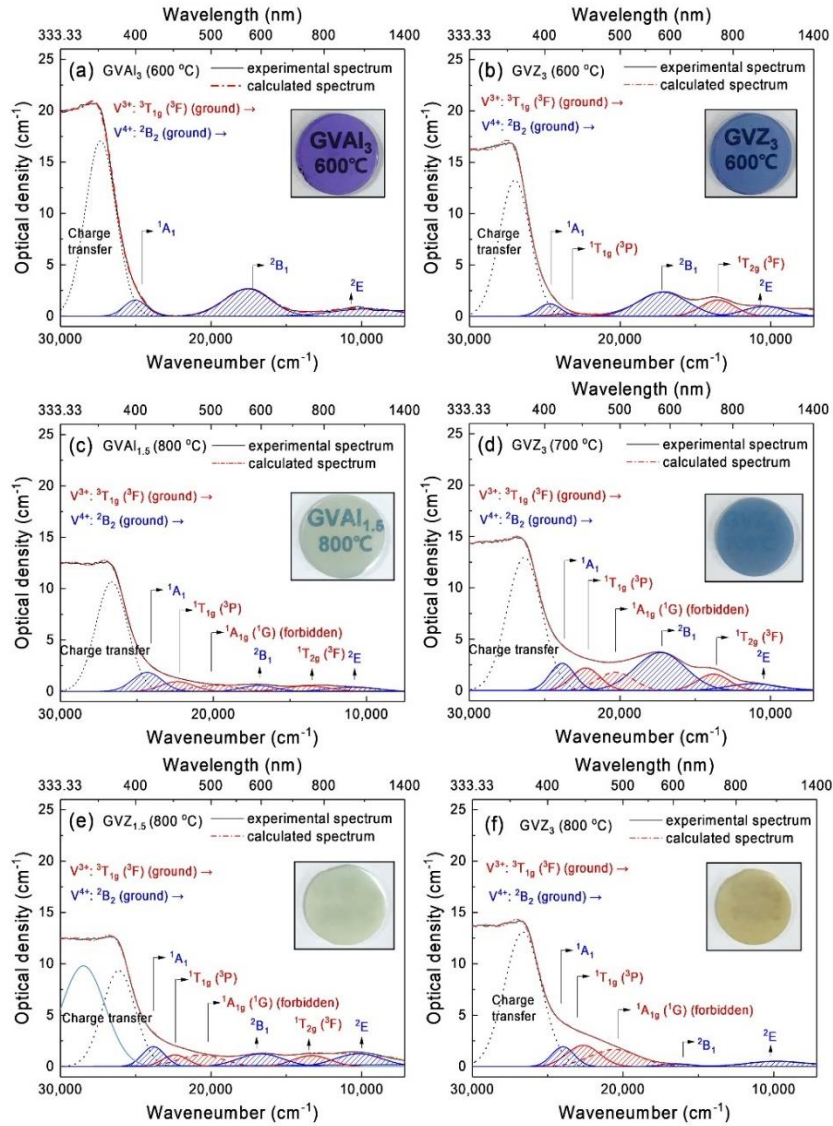
Fig. 5.3. Deconvolution of the optical densities for (a) GVAl$_3$ (600 ℃), (b) GVZ$_3$ (600 ℃), (c) GVAl$_{1.5}$ (800 ℃), (d) GVZ$_3$ (700 ℃), (e) GVZ$_{1.5}$ (800 ℃) and (f) GVZ$_3$ (800 ℃). The spectra were subtracted by a spectrum of the undoped GCs heat-treated at same conditions.
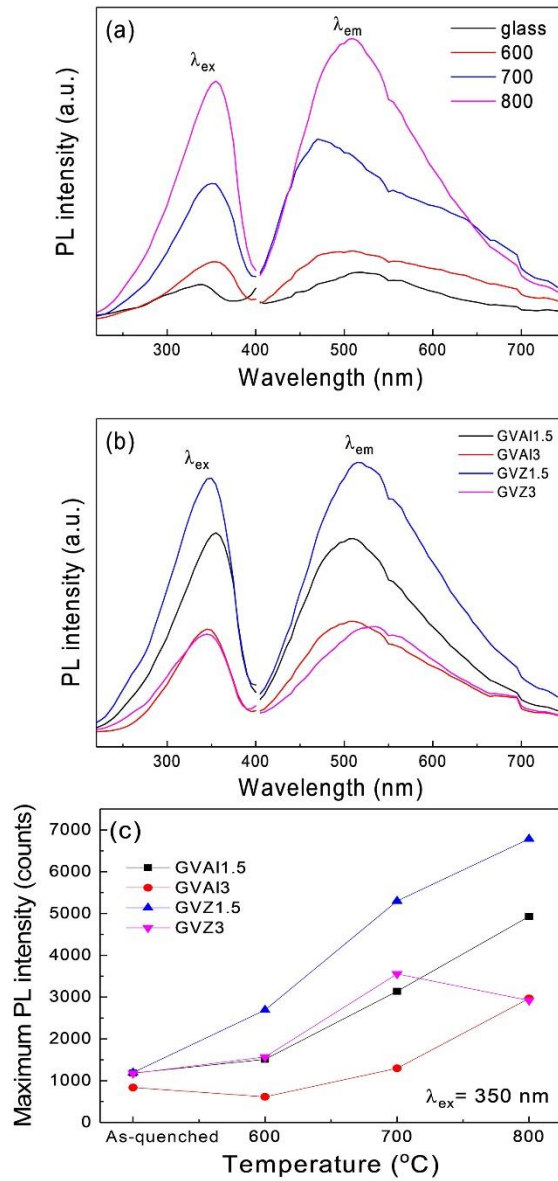
Fig. 5.4. Photoluminescence spectra of (a) GVAl$_{1.5}$ samples as-quenched and grown at different temperature, (b) GCs samples grown at 800 °C for 2 h, and (c) maximum photoluminescence intensity excited at 350 nm versus heat treatment for each samples.
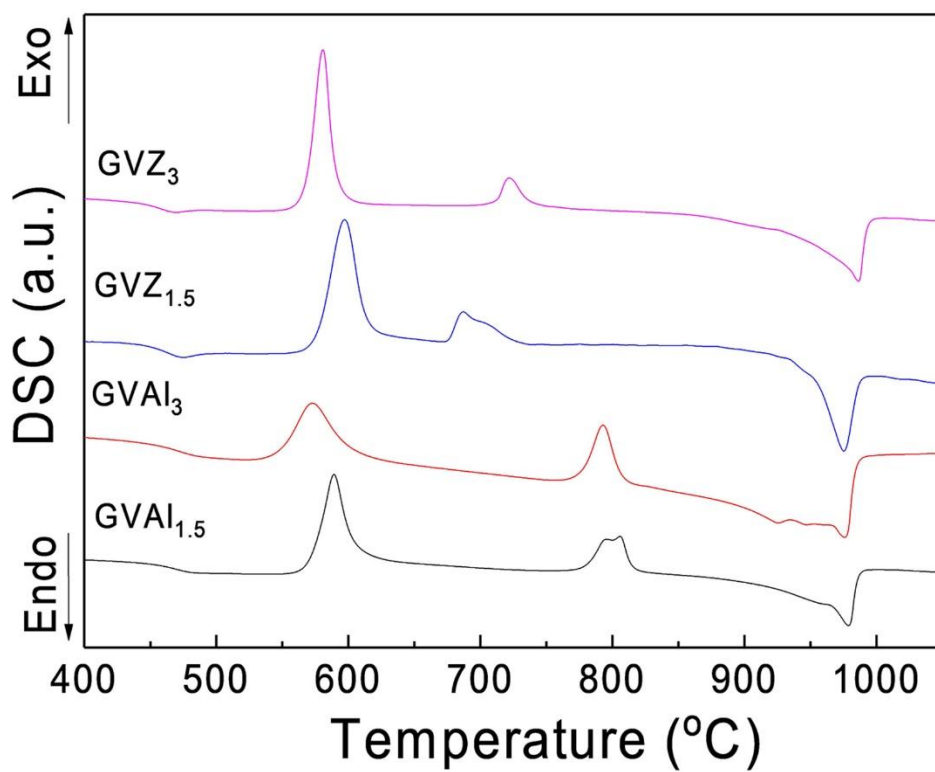
Fig. 5.5 DSC curves of the glass samples (a) $GVA_{1.5}$, (b) $GVAl_{1.5}$, (c) $GVZ_{1.5}$, and (d) GVZ_3.
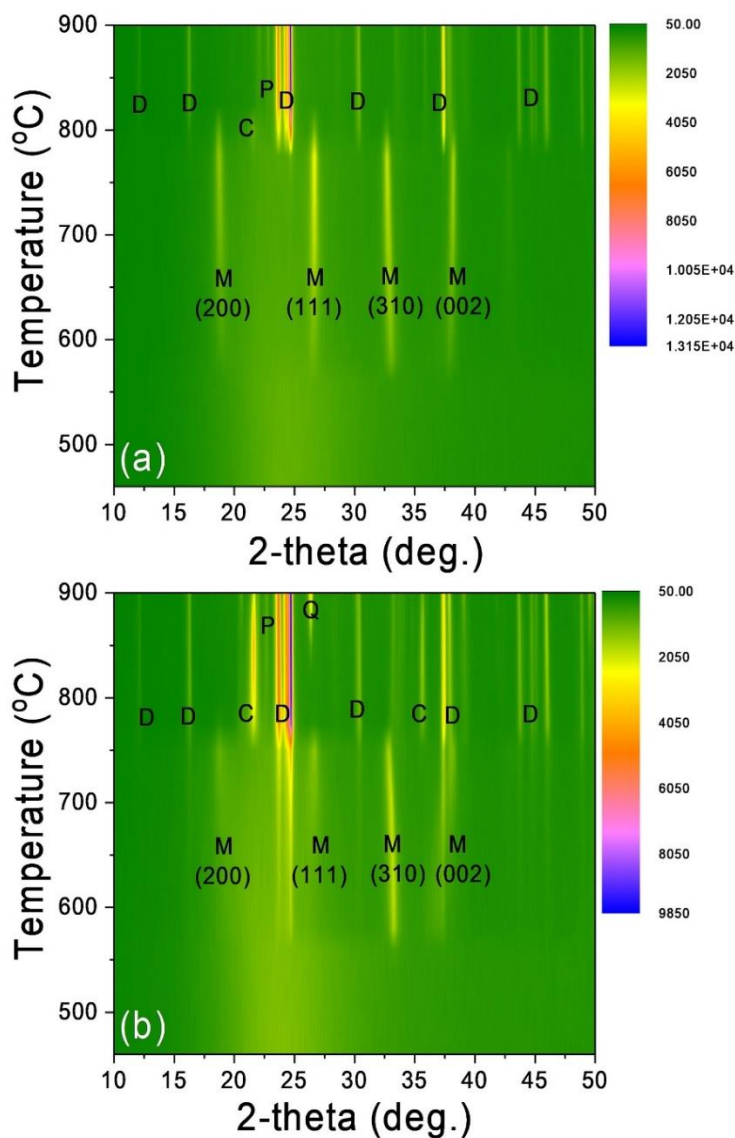
Fig. 5.6. In-situ HT-XRD patterns of the glass samples (a) GVAl$_{1.5}$ and (b) GVZ$_3$. D: Li$_2$Si$_2$O$_5$ (LS2), M: Li$_2$SiO$_3$ (LS), P: Li$_3$PO$_4$ (LP), C: cristobalite, Q: Quartz (ICDD PDF number of references: LS2 [01-070-4856], LS [00-029-0829], LP [04-006-8566], cristobalite [00-039-1425], Quartz [01-089-8937])
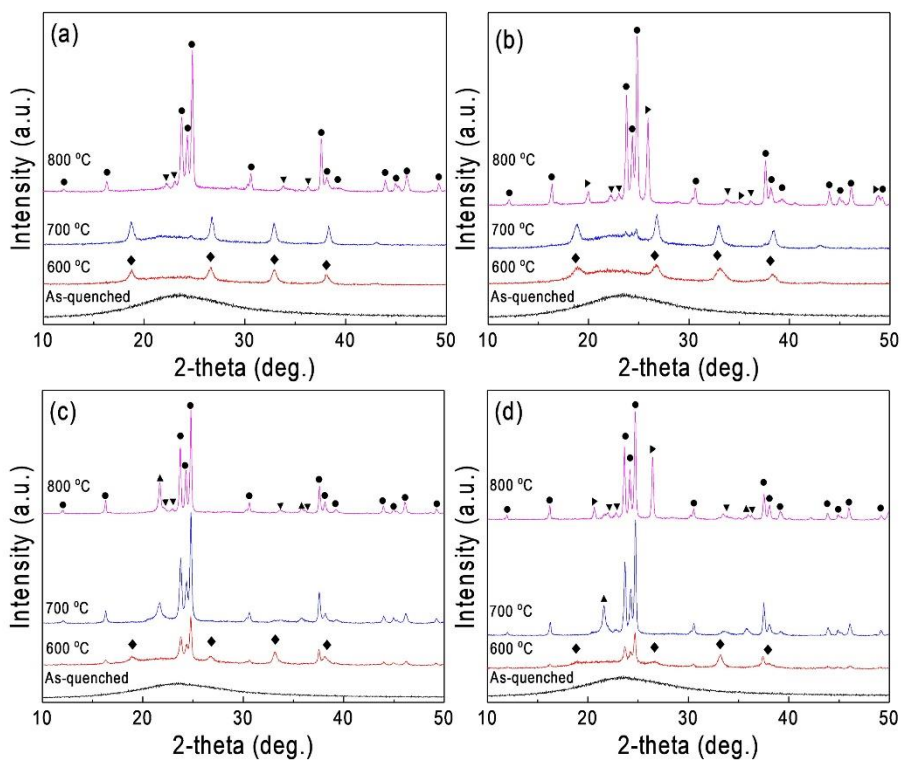
Fig. 5.7. Room-temperature XRD patterns of glasses and glass-ceramics heat treated at 600 °C, 700 °C and 800 °C for 2 h. (a) $GVAl_{1.5}$, (b) $GVAl_3$, (c) $GVZ_{1.5}$, and (d) GVZ_3. (●: LS2, ◆: LS, ▼: LP, ▲: cristobalite, ►: Quartz)
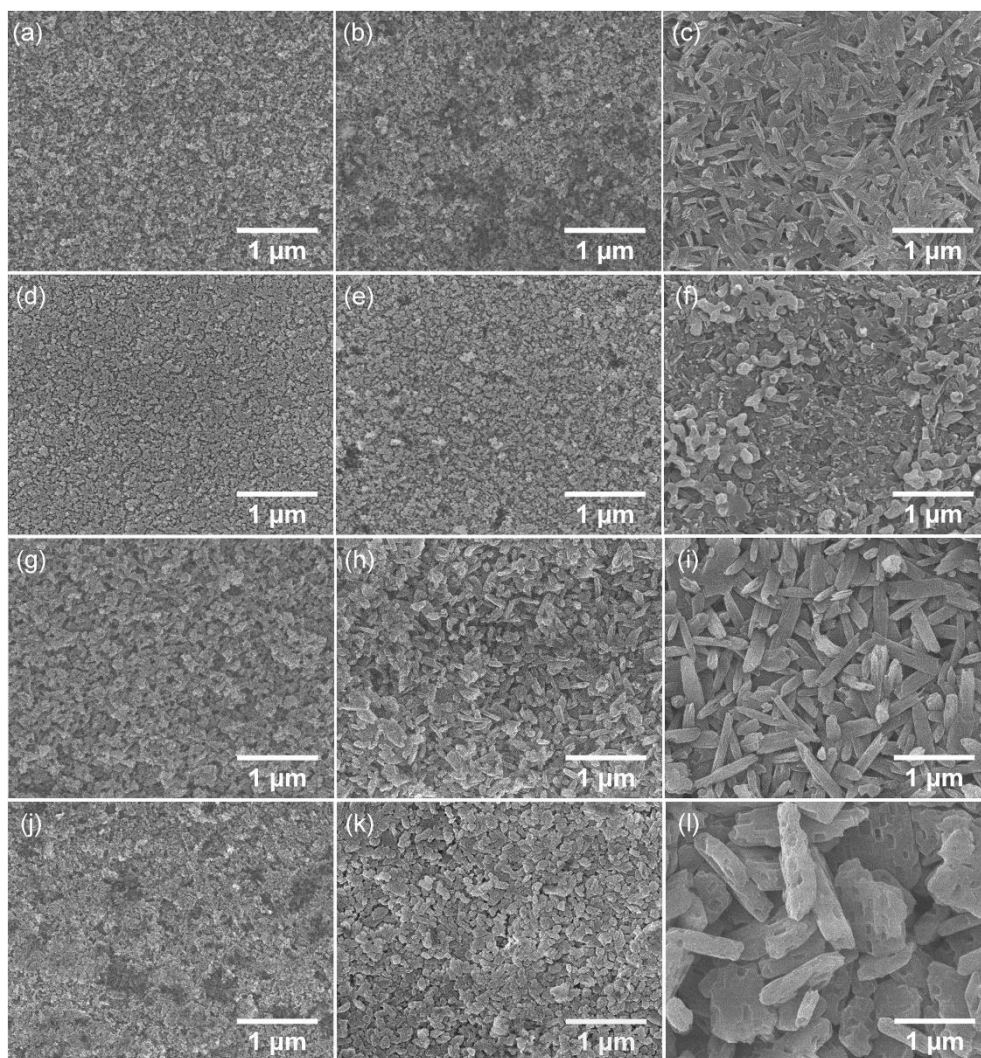
Fig. 5.8. Microstructures of the GCs heat-treated at 500 ℃ for 1 h as the nucleation stage and subsequently raised to 600, 700, and 800 ℃ for 2 h as the growth stage. Horizontal arrangement of micrographs indicates the samples with the same composition but with different growth temperatures: (a) 600 ℃, (b) 700 ℃, and (c) 800 ℃ for $GVAl_{1.5}$, (d) 600 ℃, (e) 700 ℃, and (f) 800 ℃ for $GVAl_3$, and (g) 600 ℃, (h) 700 ℃, and (i) 800 ℃ for $GVZ_{1.5}$, and (j) 600 ℃, (k) 700 ℃, and (l) 800 ℃ for GVZ_3.
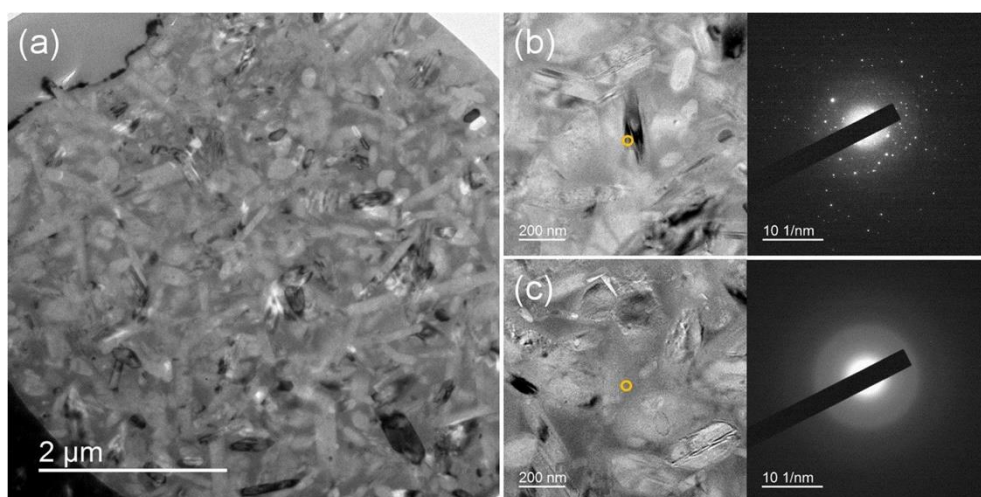
Fig. 5.9. TEM images of GVZ$_3$ heat treated at 800 ℃. Low magnification image in (a) and high magnification images and their selected area diffraction patterns of crystalline phases in (b) and residual glass phase in (c).
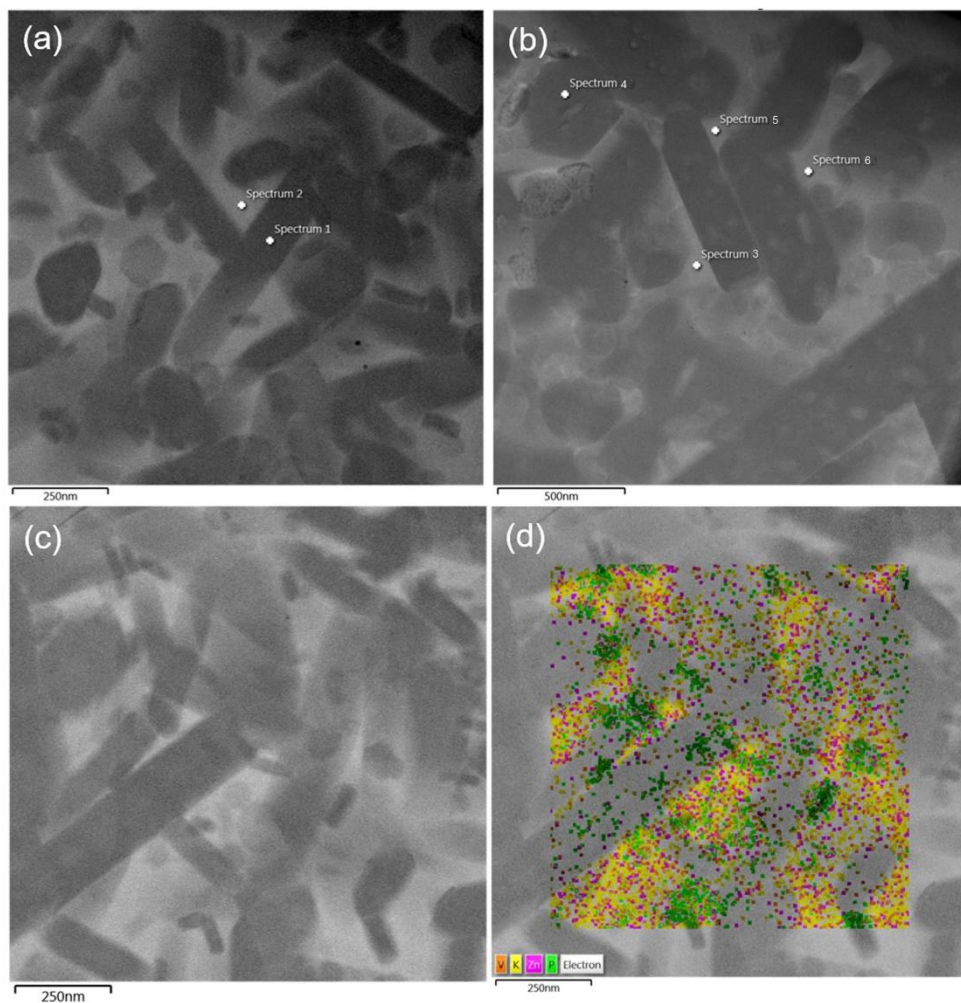
Fig. 5.10. TEM-EDS images of sample GVZ$_3$ heat treated at 800 ℃. (a) and (b) are EDS point analysis images, and (c) and (d) are EDS-mapping images. (orange is vanadium, yellow is potassium, purple is zinc and green is phosphorus)

References

[1] E. El-Meliegy, R. van Noort, Glasses and Glass Ceramics for Medical Applications, Springer Science & Business Media, 2011.

[2] H.R. Fernandes, D.U. Tulyaganov, A. Goel, M.J. Ribeiro, M.J. Pascual, J.M.F. Ferreira, Effect of Al_2O_3 and K_2O content on structure, properties and devitrification of glasses in the Li2O–SiO2 system, J. Eur. Ceram. Soc., 30 (2010) 2017-2030.

[3] D. Kim, H.-J. Kim, S.-I. Yoo, Effect of ZnO/K_2O ratio on the crystallization sequence and microstructure of lithium disilicate glass-ceramics, J. Eur. Ceram. Soc., 39 (2019) 5077-5085.

[4] W. Höland, V. Rheinberger, C. Van'T Hoen, E. Apel, P_2O_5 as an effective nucleating agent of lithium disilicate glass-ceramics, Phosphorus Research Bulletin, 19 (2005) 36-41.

[5] X.J. Xu, C.S. Ray, D.E. Day, Nucleation and crystallization of $Na_2O \cdot 2CaO \cdot 3SiO_2$ glass by differential thermal analysis, J. Am. Ceram. Soc., 74 (1991) 909-914.

[6] B. Henderson, G.F. Imbusch, Optical spectroscopy of inorganic solids, Oxford University Press, 2006.

[7] G. Kakabadse, E. Vassiliou, Isolation of Vanadium Oxides in Glasses, Phys. Chem. Glasses, 6 (1965) 33.

[8] A.M. Nassar, N. Ghoneim, Vanadium contribution in different glasses in view of the ligand field theory, J. Non-Cryst. Solids, 46 (1981) 181-195.

[9] P. Atkins, Shriver and Atkins' inorganic chemistry, Oxford University Press, USA, 2010.

[10] W. Johnston, Optical Spectra of the Various Valence States of Vanadium in $Na_2O.2SiO_2$ Glass, J. Am. Ceram. Soc., 48 (1965) 608-611.

[11] H. Wen, P.A. Tanner, Optical properties of 3d transition metal ion-doped sodium borosilicate glass, J. Alloys Compd., 625 (2015) 328-3

35.

[12] Y. Ohishi, S. Mitachi, T. Kanamori, T. Manabe, Optical absorption of 3d transition metal and rare earth elements in zirconium fluoride glasses, Phys. Chem. Glasses, 24 (1983) 135-140.

[13] A. Khudoleev, N. Bokin, Optical absorption and luminescence spectra of phosphate glasses activated with trivalent vanadium, J. Appl. Spectrosc., 14 (1971) 75-76.

[14] G. Gao, R. Meszaros, M. Peng, L. Wondraczek, Broadband UV-to-green photoconversion in V-doped lithium zinc silicate glasses and glass ceramics, Opt. Express, 19 (2011) A312-A318.

[15] S. Dzwigaj, M. Matsuoka, M. Anpo, M. Che, Evidence of three kinds of tetrahedral vanadium (V) species in VSiβ zeolite by diffuse reflectance UV−visible and photoluminescence spectroscopies, The Journal of Physical Chemistry B, 104 (2000) 6012-6020.

[16] Y. Teng, K. Sharafudeen, S. Zhou, J. Qiu, Glass-ceramics for photonic devices, J. Ceram. Soc. Jpn., 120 (2012) 458-466.

[17] S. Huang, Z. Huang, W. Gao, P. Cao, Trace phase formation, crystallization kinetics and crystallographic evolution of a lithium disilicate glass probed by synchrotron XRD technique, Scientific reports, 5 (2015) 9159.

[18] S. Huang, Z. Huang, W. Gao, P. Cao, In Situ High-Temperature Crystallographic Evolution of a Nonstoichiometric $Li_2O \cdot 2SiO_2$ Glass, Inorg. Chem., 52 (2013) 14188-14195.

[19] S. Huang, Z. Huang, W. Gao, P. Cao, Structural Response of Lithium Disilicate in Glass Crystallization, Crystal Growth & Design, 14 (2014) 5144-5151.

[20] C.B. Carter, M.G. Norton, Ceramic materials: science and engineering, Springer Science & Business Media, 2007.

[21] W. Paszkowicz, A. Wolska, M. Klepka, F. Ezz-Eldin, Combined X-Ray Diffraction and Absorption Study of Crystalline Vanadium-Doped Lithium Disilicate, Acta Physica Polonica, A., 117 (2010).

[22] C. Angell, D. Gruen, Octahedral-Tetrahedral Coordination Equilibria of Nickel (II) and Copper (II) in Concentrated Aqueous Electrolyte Solutions1, J. Am. Chem. Soc., 88 (1966) 5192-5198.

[23] C. Angell, D. Gruen, Short-Range Order in Fused Salts. I. Coordination States of Nickel (II) in Molten Zinc Chloride-Potassium Chloride Mixtures1, The Journal of Physical Chemistry, 70 (1966) 1601-1609.

[24] S. Morimoto, S. Khonthon, Y. Ohishi, Optical properties of Cr^{3+} ion in lithium metasilicate $Li_2O \cdot SiO_2$ transparent glass–ceramics, J. Non-Cryst. Solids, 354 (2008) 3343-3347.

[25] J. Duffy, M. Ingram, An interpretation of glass chemistry in terms of the optical basicity concept, J. Non-Cryst. Solids, 21 (1976) 373-410.

[26] J.A. Duffy, The refractivity and optical basicity of glass, J. Non-Cryst. Solids, 86 (1986) 149-160.

[27] A. Paul, Chemistry of glasses, Springer Science & Business Media, 1990.

[28] W. Vogel, Glass chemistry, Springer Science & Business Media, 2012.

[29] I. Donald, P. McMillan, Ceramic-matrix composites, Journal of materials Science, 11 (1976) 949-972.

[30] J.M. Rincón, C. González-Oliver, P. James, Phase separation in Li_2O-SiO_2 glasses with additions of V_2O_5, MnO_2 and Cr_2O_3, Journal of materials science, 23 (1988) 2512-2516.

[31] Z. Chaowu, Y. Ruilun, Effects of V_2O_5 on phase separation and leaching of Na_2O-B_2O_3-SiO_2 glasses, J. Non-Cryst. Solids, 112 (1989) 244-250.

[32] V. Marghussian, U. Balazadegan, B. Eftekhari-Yekta, The effect of BaO and Al_2O_3 addition on the crystallization behaviour of cordierite glass ceramics in the presence of V_2O_5 nucleant, J. Eur. Ceram. Soc., 29 (2009) 39-46.

[33] J. Williamson, A. Tipple, P. Rogers, The effect of vanadium oxides on the crystallisation of silicate glasses, Journal of Materials Science, 4 (1969) 1069-1074.

Chapter 6

Optimization of coloration for dental application

6.1 Introduction

Optimization of coloration in LS2 GCs for dental application can be achieved by considering the base glass composition and redox reaction between colorant ions. First, the lightness (L*) is the reflected light from the sample. It is known that the lightness of LS2 GCs is controlled by the difference in refractive index between the residual glassy phase and LS2 crystal, and also by the volume fraction of the crystalline phase and crystal size [1]. The refractive index of the LS2 crystalline phase is known to be about 1.55 and that of the matrix glass is ~1.5. Nb_2O_5, Ta_2O_5, and Eu_2O_3 are expected to modify the refractive index of the residual glass matrix due to its high ionic polarizability [2]. Meanwhile, the chromaticity of GCs is governed by the valency and concentration of the colorant ion. As we confirmed in the previous chapter, during crystallization, the colorant ion becomes incorporated in the residual glassy matrix unless it forms a solid solution in the LS2 crystal. The valency of the colorant ion predominantly depends on the composition of the residual glassy matrix. To mimic the coloration of human teeth, various colorants are needed since each colorant ion possesses a specific absorption band and the combination of colorants could impart a color similar to human teeth.

Chapter 6: Optimization of coloration for dental application

As previously mentioned, human teeth possess chromaticity with an L* of 67.6 ± 7.0, an a* of 4.3 ± 2.1, and a b* of 12.1 ± 3.3 [3]. To reproduce a color similar to human teeth, CeO_2 and TiO_2 are selected to increase the b* parameter (yellowish) since it is known that the characteristics of a yellow-orange color is caused by the formation of chromophoric centers containing products from the interaction of cerium and titanium ions [4, 5].

In addition, when a lot of colorant ions are added, light absorption is increased and reflected light is reduced, hence the L* value is reduced. Therefore, a glass base composition was designed to minimize the reduction of L* due to the addition of colorant ions. The decrease in L* occurs when the difference between the refractive index between the residual glassy matrix and the LS2 crystal is small. When a colorant ion is added, it is mainly located in the residual glassy matrix and improves the refractive index of the glass matrix, resulting in the decrease in the difference of refractive index with LS2 crystal. As the difference in refractive index is made smaller, less scattering occurs and L* decreases. ZnO added for chemical durability of the residual glassy matrix has a refractive index of ~2 and Al_2O_3 having the same role is ~1.69 [6]. Therefore, the effect of ZnO and Al_2O_3 on translucency with the addition of CeO_2 was investigated.

Furthermore, as mentioned in the previous chapter, the vanadium ion also exhibits a yellowish color when it is reduced to V^{3+}. Therefore, V_2O_5 is selected to increase the b* parameter with the addition of CeO_2. For the a* parameter, MnO_2 and Er_2O_3 are considered since Mn^{3+} exhibits a purple color [7-9] and Er^{3+} exhibits a pink color [2, 10]. In addition, the colorant may affect the crystallization behavior of LS2 GCs such as nucleation and crystal growth, causing the alteration of microstructure and

mechanical properties. Thus, in this chapter, we investigate the colorants CeO_2, MnO_2, V_2O_5, and Er_2O_3 on the coloration and crystallization behavior in LS2 GCs.

6.2 Experimental

Table 6.1. shows the glass composition doped with CeO_2 and TiO_2. The base glass composition is identical to the sample ID of P1.25Z/K0.7 shown in the previous chapter 4 ($66.27SiO_2$–$27.73Li_2O$–$1.25P_2O_5$–$2.75K_2O$–$2ZnO$). The glasses were designed as a two series. Series 1 is the single addition of each CeO_2 and TiO_2, and the increasing TiO_2 content from 0 to 1 mol% when CeO_2 was fixed to have 0.5 mol%. Series 2 is the combination of CeO_2 and TiO_2 with CeO_2 content varying from 0 to 2 mol% when TiO_2 was fixed to have 0.5 mol%. To produce the glass-ceramic, the glass block samples were nucleated at 500 °C for 1h in air with the heating rate of 10 °C/min, and subsequently heated up to 800 °C for crystal growth with the heating rate of 30 °C/min for 2h. The temperature for nucleation was chosen by Marotta's method which determines the temperature of maximum nucleation rate [11].

6.3 Results and discussion

6.3.1 Coloration in CeO₂/TiO₂-doped lithium disilicate glass-ceramics

Fig. 6.1 shows the photographs of glass and GCs samples. For series 1 glass samples in Fig. 6.1(a), the base, Ce0.5 and Ti0.5 are colorless while the Ce0.5Ti0.5

and Ce0.5Ti1.0 are weak yellowish. In GC samples, the base, Ce0.5 and Ti0.5 are white and translucent whereas the Ce0.5Ti0.5 and Ce0.5Ti1.0 are yellowish and highly translucent compared with single addition of CeO_2 and TiO_2. For series 2 glass samples in Fig. 6.1(b), with increasing CeO_2 content, the glass samples become more yellowish. On the other hand, in GC sample, the translucency is maintained until the addition of CeO_2 up to 0.75 mol%, however, addition of CeO_2 over 1.0 mol% leads to become completely opaque.

The L*a*b* color parameters of GC samples are listed in Table 6.1. L* describes lightness from black (0) to white (100) and a* denotes the green (negative) – red (positive) value, and b* indicates the blue (negative) – yellow (positive) value. Compared with Base sample, L* of the Ce0.5 and Ti0.5 sample slightly decrease and increase, and a* and b* values of that decrease. In contrast, when the CeO_2 and TiO_2 is added simultaneously such as Ce0.5Ti0.5 and Ce0.5Ti1.0 samples, it can be seen that the L* and a* values are decreased and the b* values are increased. It corresponds with the observation in Fig. 6.1(a) that the Ce0.5Ti0.5 and Ce0.5Ti1.0 GC samples becomes more yellowish and translucent. For series 2, when the TiO_2 is fixed to have 0.5 mol%, the L* values initially drops in Ce0.5Ti0.5 and increases with further CeO_2 addition, reaching the maximum value of 90.81 in Ce1.0Ti0.5 sample. The a* values initially shows the maximum negative value of -3.45 in Ce0.5Ti0.5 sample and it increases with increasing the CeO_2 addition, however, it ended up the negative value as -1.24 for the maximum. On the other hand, the b* values are constantly increased until the 0.75 mol% of CeO_2 is added, and it gradually decreased with further addition of CeO_2.

Fig. 6.2 shows the transmittance and absorption coefficient of glass and GCs samples for series 1. In Fig. 6.2(a), the maximum transmittance of all glass samples in series 1 presents over 80%. The UV cut-off for Ti0.5 glass lies at 290 nm and that for Ce0.5 glass locates at 350 nm. The combination of CeO_2 and TiO_2 such as Ce0.5Ti0.5 and Ce0.5Ti1.0 presents the shift of the UV cut-off to 380 nm and decrease in slope. This is in good agreement with the previous report that the cerium- and titanium containing glasses shows the long-wavelength shifts of the spectra and decreases slope with increasing cerium and titanium contents [5]. According to Trusova et al. [4], long wave-length shifts of the spectra with addition of CeO_2 and TiO_2 can be caused by high field strengths of Ce^{4+} and Ti^{4+} ion in glass, polarizing the surrounding oxygen ions and resulting in the weakened the electric field of Ce^{4+} and Ti^{4+} ions. Thus, the absorptions are shifted to longer wavelength. Likewise, the shifts of UV cut-off to longer wavelength in this study might be attributable to the addition of CeO_2 and TiO_2.

For GC samples, the maximum transmittance is different for each sample as shown in Fig. 6.2(b). The lowest transmittance is obtainable in Base sample and followed by Ce0.5, Ti0.5, Ce0.5Ti0.5 and Ce0.5Ti1.0 samples. It is seen that those decrease in transmittance is caused by the reflection in crystalline phase after crystallization. The UV cut-off for Ti0.5, Ce0.5, Ce0.5Ti0.5 and Ce0.5Ti1.0 samples are similar to that of corresponding glass samples.

Figs. 6.2(c) and (d) shows the absorption coefficient of glass and GC samples. For glass samples in Fig. 6.2(c), Base sample presents absorption with low slope below 300 nm which can be identified as optical band gap. Ti0.5 sample exhibits the absorption peak at 300 nm. It is reported that Ti^{3+} with electronic configuration

$3d^1$ shows absorption bands at 500-600 nm of the $^2T_2 \rightarrow {}^2E$ transition [12]. Ti^{4+} has a $3d^0$ electronic configuration with no electrons in the d orbital, hence no d-d transition is observable and only absorption occurs in the UV region by charge transfer and its absorption locates at 250 and 290 nm [13, 14]. Therefore, the titanium ion can be assigned as Ti^{4+} for Ti0.5 sample. For the samples containing CeO_2, two peaks are observable at 250–290 nm and 350 nm, respectively. The absorption bands of Ce^{4+} and Ce^{3+} ions are reported to be placed at 240 and 314 nm in silicate glass, 250 and 324 nm in barium aluminosilicate glass, respectively [15-19]. Thus, cerium ion is determined to be present in two valence states as Ce^{3+} and Ce^{4+} in the glass and its location is different with the literature due to the different host i.e. glass matrix [19, 20]. The absorption peak location of Ce^{3+} is seem to be fixed at 350 nm whereas that of Ce^{4+} constantly varies with addition of TiO_2 from the 250 nm to 270 and 290 nm. Furthermore, while the absorption peak intensity of Ce^{4+} is maintained, that of Ce^{3+} is gradually increased with addition of TiO_2, implying that the Ce^{4+} is reduced to Ce^{3+} by Ti^{4+} as the following,

$$Ce^{4+} + Ti^{3+} = Ce^{3+} + Ti^{4+} \quad (1)$$
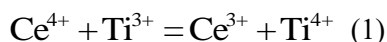
These redox reactions between cerium and titanium ion has been reported with respect to the glass, GCs and CeO_2-TiO_2 film [21-26]. Interestingly, the absorption peak intensities of Ce^{3+} at 350 nm is significantly increased in GC sample compared with glass samples, suggesting that the extent of reduction from Ce^{4+} to Ce^{3+} is enhanced. It might be attributable to the change of composition in residual glassy matrix after crystallization compared with original glass composition.

Fig. 6.3 shows the transmittance and absorption coefficient of glass and GCs samples for series 2. With increasing the CeO_2 content, the slope of UV cut-off in

transmittance in glass are decreased as shown in Fig. 6.3(a). On the other hand, for GC samples in Fig. 6.3(b), the highest transmittance is achieved in Ce0.5Ti0.5 sample and followed by the samples with increasing the CeO_2. In particular, samples added over CeO_2 of 1.0 mol% exhibits remarkably low transmittance. For absorption behavior in glass, the absorption peak intensities are increased with increasing CeO_2 content and it is announced in Ce^{3+} than in Ce^{4+}. However, in GC samples, the abrupt increase in absorption is observable in the samples added over CeO_2 of 1.0 mol% as shown in Fig. 6.3(d).

Fig. 6.4 illustrates the DSC curves of all glass samples. One exothermic peak was observable in all samples. The characteristic DSC temperature are listed in Table 6.2. For series 1 samples in Fig. 6.4(a), it is seen that the single addition of CeO_2 negligibly affects the glass transition temperature (T_g) whereas single addition of TiO_2 and combination with CeO_2 lead to increase in T_g. In general, when the ratio of glass modifier is increased by addition of alkali oxide, T_g decreases due to the weakening of glass structure by formation of non-bridged oxygen. On contrary, when the ratio of glass former is enhanced, T_g increase [27]. It suggests that the Ti^{4+} act as glass former, leading to strengthening of glass structure by forming $[TiO_4]$ group in glass and resulting in the increase of T_g. It is in accordance with the report of Matusita et al. [28] that T_g is increased by addition of TiO_2 in LS2 glass. With respect to the exothermic peaks, the single addition of CeO_2 shows a slight increase in onset (T_x) and peak temperature (T_p) for crystallization and a small decrease in height of crystallization peak (δT_p). For single addition of TiO_2, while the T_x and T_p is unaltered, δT_p is enhanced 10 °C compared with base sample. According to previous report [29-31], the nucleation rate can be estimated using the DSC characteristic

temperature, δT_p and T_p, which predict the number of nuclei and density of nuclei in glass, respectively. Thus, it implies that the total number of nuclei is increased by addition of TiO2. It is in good agreement with previous report that TiO_2 is well known nucleating agent for GCs for lithium aluminosilicate [32-35], and is known to induce surface crystallization for LS2 glass [36]. However, combination of CeO_2 and TiO_2 for Ce0.5Ti0.5 and Ce0.5Ti1.0 sample present the increase in T_x and T_p, and decrease in δT_p, indicating that number of nuclei is decreased.

For series 2 sample in Fig. 6.4(b), the T_x and T_p shift to higher temperature and the δT_p decrease with increasing the CeO_2 content. It is previously reported that CeO_2 is nucleation inhibitor in LS2 glass [37] and the growth velocities is significantly reduced with addition of CeO_2 and TiO_2 [38]. It signifies that the nucleation and crystal growth might be reduced with increasing the CeO_2.

Fig. 6.5 shows the XRD patterns of the glass and GCs samples. All glass samples are fully vitrified without any crystalline phase as shown in Figs. 6.5(a) and (b). For series 1 samples, the LS2 and Li_3PO_4 (LP) crystalline phases are detectable in all GC sample whereas cristobalite phase is only observable in base sample as shown in Fig. 6.5(c). On the other hand, for series 2 samples, CeO_2 phase is detectable in addition of CeO_2 over 1.0 mol% as shown in Fig. 6.5(d). Table 6.3 presents the calculated volume fraction of phases in GC samples. Compared with base sample, the volume fraction of glass phase is reduced ~ 20% in Ti0.5 and Ce0.5Ti0.5 samples. For series 2 sample, while the volume fractions of LS2 and LP phases are gradually decreased with increasing the CeO2 content, that of residual glassy matrix and CeO_2 is increased.

Fig. 6.6 shows microstructure of GC samples for series 1. It is seen that the single addition of CeO2 and TiO_2 and the combination of CeO_2 and TiO_2 insignificantly affect the crystal morphology. Thus, it is noticed that maximum biaxial flexural strength obtained in Ti0.5 sample might be attributable to lowest volume fraction of glassy phase among the samples. In addition, it should be noted that the Ce0.5Ti0.5 and Ce0.5Ti1.0 GC sample was highly translucent compared with base, Ce0.5 and Ti0.5 samples as shown in Fig. 6.1(a) although the variation of microstructure is negligible and volume fraction of glass phases are in the range of 21–26%. It suggests that these high translucency is not related to the microstructure or volume fraction of crystalline phase in GC sample. In general, it is known that the translucency of GCs generally depends on the volume fraction and size of crystalline phase and the difference of refractive index between crystalline phases and residual glassy phase [1]. The refractive index of the LS2 crystalline phase is reported be ~1.55 and that of the matrix glass is ~1.5 and the Nb_2O_5, Ta_2O_5 and Eu_2O_3 are believed to modify the refractive index of residual glass matrix due to its high ionic polarizability [2]. The refractive index of CeO_2 and TiO_2 are reported to be 2.08–2.23 and 2.3, respectively [39]. Therefore, it is speculated that the high translucency in Ce0.5Ti0.5 and Ce0.5Ti1.0 sample might be caused by combination of CeO_2 and TiO_2 located in residual glassy matrix after crystallization enhancing the refractive index of residual glassy matrix. It leads to cause low scattering at the interface between residual glassy matrix and LS2 crystal.

Fig. 6.7 exhibits microstructure of GC samples for series 2 with backscattered electron mode. One can see that white crystals with a size of 300 nm or less is observable from 0.75 mol% of CeO_2, and number of nano-sized particles were

increased and randomly distributed as the amount of CeO_2 increased. Furthermore, the crystal size of LS2 crystal is increased with increasing the CeO_2 content. It coincides the fact that the CeO_2 act as nucleation inhibitor as previously mentioned, which is also supported by the DSC results showing the shift of T_x and T_p to higher temperature and the decrease in δT_p.

To identify the nano-sized white crystal in Fig. 6.7, SEM-EDS analysis is conducted in Ce1.0Ti0.5 GC sample as shown in Fig. 6.8. The cubic morphology is observable in nano-sized white crystal as shown in Figs. 6.8(a) and (b). It was found that the white crystal is determined as CeO_2 phase based on EDS point spectrum analysis in Fig. 6.8(c), which agrees well with XRD results in Fig. 6.5 showing the CeO_2 precipitation when CeO_2 added over 1.0 mol%. Since cubic CeO_2 has a very high refractive index of 2.3 [39] compared with LS2 glass (~1.5) and LS2 crystal (~1.55), and also the CeO_2 phase of 300 nm or less is smaller than visible light, it increases Rayleigh scattering which is the elastic scattering of light described by the following equation [40],

$$I_s = I_0 \frac{9\pi^2 V^2}{2d^2\lambda^4} \left(\frac{m^2-1}{m^2+2} \right)^2 (1+\cos^2\theta) \quad (2)$$

where I_s is the intensity of scattered light, I is incident light, V is the volume of the particle, d is the distance to the particle, λ is the wavelength of light, m is the refractive index, and θ is the scattering angle. It suggests that the increased scattering of light due to CeO_2 phase is responsible for the decreased translucency of the samples containing 1–2 mol% CeO_2 for series 2 as described by the abrupt increased L* value in Table 6.1.

Fig. 6.9 shows biaxial flexural strength and Vickers hardness of GC samples. For series 1, it can be seen that the single addition of CeO_2 and TiO_2 improves the biaxial flexural strength compared with the base sample, and a particularly highest strength of 503.61 ± 21.49MPa among the sample is obtainable in Ti0.5 sample. When both CeO_2 and TiO_2 are added, the flexural strength decreases compared with single addition of CeO_2 and TiO_2. However, the Vickers hardness is consistently enhanced by the single addition and the combination of CeO_2 and TiO_2. It might be ascribable to the fact that the Ce and Ti ions are distributed in the residual glassy matrix and causes a strengthening of the glassy matrix [15, 16]. For series 2, the biaxial flexural strength and Vickers hardness are gradually decreased with increasing the CeO_2 content. It is attributable to the increase in the size of the LS2 crystals as shown in Fig. 6.7. In addition, the precipitated nano-sized CeO_2 might affects the stress distribution, resulting in the decrease in biaixial flexural strength and the Vickers hardness.

Based on these results, it was concluded that CeO_2 should be added to an amount that does not crystallize into nanocrystals, and TiO_2 should not be included because TiO_2 rapidly decreases the L* value below the that of human teeth. Still, a* parameter was not achieved by addition of CeO_2 and TiO_2. Therefore, it needs additional colorant for the increasing a* parameter.

Chapter 6: Optimization of coloration for dental application

6.3.2 Coloration in CeO$_2$/V$_2$O$_5$-, CeO$_2$/MnO$_2$-, and CeO$_2$/V$_2$O$_5$/MnO$_2$-doped lithium disilicate glass-ceramics

To obtain an adequate a* parameter, varying amounts of MnO$_2$ ranging in 0, 0.05, 0.1, 0.25, 0.5, and 1 mol% were added with a fixed amount of CeO$_2$, designated as CM. Since an acceptable b* parameter could not be obtained with CeO$_2$ alone, varying amounts of V$_2$O$_5$ ranging in 0, 0.05, 0.1, 0.25, and 0.5 mol% were added with a fixed amount of 0.5 mol% CeO$_2$, denoted as CV. Finally, to satisfy both the a* and b* parameter varying amounts of MnO$_2$ ranging in 0, 0.05, 0.1, 0.25, 0.5, and 1 mol% were added with a fixed amount of 0.5 mol% CeO$_2$ and 0.05 mol% V$_2$O$_5$, designated as CVM. All samples were heat treated at 500 ℃ for 1 h followed by 800 ℃ for 2 h for crystallization. The photograph of the CM, CV, and CMV GC samples are shown in Fig. 6.10 (a).

The L*a*b* color space is shown in Fig. 6.10 (b) and (c) in order to quantitatively compare the L*a*b* parameters of the samples. When MnO$_2$ was added alone, denoted with M0.5, it had a purple color due to the presence of Mn^{3+}. When CeO$_2$ was added simultaneously, the increase in a* was not dramatic. When V$_2$O$_5$ was added alone, denoted with V0.5, it showed a greenish color. When CeO$_2$ was added with V$_2$O$_5$, b* increased dramatically, and a* also decreased. In CV0.5, although b* of more than 20 and a* of 0 were obtained, the value of human teeth was not satisfied because the L* was as low as 42. This is attributable to the high concentration of V$_2$O$_5$ which absorbs light. When CeO$_2$-V$_2$O$_5$ was fixed and varying amounts of MnO$_2$ was added to improve a*, a* and b* were improved, however, an appropriate a* value approximating human teeth was still not achieved (Fig. 6.10(c)).

The absorbance of glass and GCs is shown in Fig. 6.11. As shown in Fig. 6.11(a), M0.5 shows a broad absorption band at 500 nm, which is due to Mn^{3+}. It can be seen that Mn^{3+} is reduced to Mn^{2+} (colorless) due to the presence of Ce by the following equation,

$$Ce^{3+} + Mn^{3+} = Ce^{4+} + Mn^{2+} \quad (3)$$
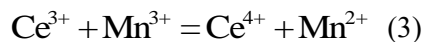
When Ce and Mn are co-doped, a* increases slightly as the amount of Mn^{2+} increases, but it can be seen that the increase is not large. In Fig. 6.11(b), V0.5 shows a broad absorption band in the UV region below 400 nm because of V^{5+} which has a $3d^0$ electronic configuration [41]. As the amount of V_2O_5 increased, it was observed that V^{5+} was reduced to V^{4+} and V^{3+} by CeO_2 as shown by the following redox reaction,

$$Ce^{3+} + V^{5+} = Ce^{4+} + V^{4+}$$
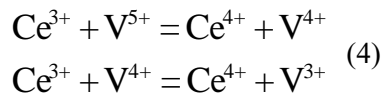$$Ce^{3+} + V^{4+} = Ce^{4+} + V^{3+} \quad (4)$$

Fig. 6.12 shows the XRD patterns of the CM, CV, and CVM GC samples. Only the LS2 and LP phases were crystallized. It can be seen that the addition of CeO_2, V_2O_5, and MnO_2 did not significantly affect crystallization. Similarly, the microstructure was not significantly varied with the addition of CeO_2, V_2O_5, and MnO_2 as shown in Figs. 6.13-15. It was found that the change in crystal size was negligible.

6.3.3 Control of translucency in ZnO_2-, Al_2O_3-, and ZnO_2/Al_2O_3-doped lithium disilicate glass-ceramics

In 6.3.2 chapter, it was found that b* was satisfied using a combination of CeO_2 and V_2O_5, however, a* was not achieved. Therefore, since the improvement of the refractive index of the residual glassy matrix is relatively suppressed, three base compositions including ZnO, Al_2O_3, and both ZnO and Al_2O_3 were fabricated and are denoted as samples Z, A, and ZA, respectively. Table 6.4 shows the glass compositions. All samples were added with 0, 0.5, 0.75, 1.0, and 1.5 mol% CeO_2, and were crystallized by heat treatments at 500 °C for 1 h followed by 800 °C for 2 h.

Fig. 6.16 shows the photographs and L*a*b* color space. As shown in Fig. 6.16(b), sample Z had the lowest L*, sample A showed an L* of ~72, and ZA showed an L* similar to A at 1 mol% CeO_2. In addition, the highest a* and b* parameters were satisfied in the ZA sample at 1 mol% CeO_2 with adequate value of L* for imitation of human teeth, as shown in Fig. 6.16(c). Therefore, the ZA composition was determined to the base glass composition.

6.3.4 Coloration in CeO₂/V₂O₅/Er₂O₃-doped lithium disilicate glass-ceramics

For the optimization of coloration for dental application, CeO_2 and V_2O_5 were selected for b* enhancement, and Er_2O_3 was selected for a* enhancement to perform the CeO_2-V_2O_5-Er_2O_3 mixture experiment. The amount of CeO_2 is fixed, Er_2O_3 is set at 0, 0.05, and 0.1 mol%, and V_2O_5 is varied from 0-0.05 mol%. The samples are shown in Fig. 6.17(a). All samples of L* value were within the human teeth value range. With increasing the V_2O_5, b* increased from ~3 to ~15. a* increased with the addition of Er_2O_3 as shown in Figs 6.17(a) and (b). When Er_2O_3 was added up to 0.1 mol%, it was confirmed that the color achieved the targeted human teeth range of L* of 67.6 ± 7.0, an a* of 4.3 ± 2.1, and a b* of 12.1 ± 3.3 [3]. Fig. 6.18 shows the absorbance with the addition of V_2O_5 and Er_2O_3. It can be seen that, when Er is added, an absorption peak exists at 520 nm, thereby improving the value of the complementary color a*. XRD analysis was conducted to confirm the effect of the colorants on crystallization as shown in Fig. 6.19, and it was confirmed that the the crystallization behavior was unaltered.

Finally, biaxial flexural strength was checked for the CeO_2-V_2O_5-Er_2O_3 mixture GCs. When a small amount of V_2O_5 was added (sample Er0), the strength increased slightly, and when Er increased to 0.05 and 0.1 mol%, a consistent decrease in biaxial flexural strength was obtained. This is due to the more open glass structure caused by the addition of Er_2O_3 which might weaken the residual glassy matrix [42]. Nevertheless, the high biaxial flexural strength value of 400 MPa or more was achieved with the satisfaction of coloration in GCs for dental application.

6.4 Summary

Ce^{4+} was reduced to Ce^{3+} by Ti^{4+}, and the absorption band of Ce^{3+} was located in 350 nm, which resulted in an increase in b* parameter and a decrease in a* parameter. Nano-sized CeO_2 crystals precipitated when over 1.0 mol% CeO_2 was added, causing significant light scattering by Rayleigh scattering mechanism, and resulting in an increase of L* over that of human teeth. CeO_2 addition reduced the nucleation rate of LS2 crystals, resulting in an increase in LS2 crystal size, and a decrease in biaxial flexural strength and Vickers hardness. Although the redox agent TiO_2 increased the b* parameter, it also decreased the a* parameter, and the translucency of GCs exceeded the range of the translucency of human tooth, resulting in low lightness. V^{5+} was reduced to V^{3+} (yellow) by Ce^{3+} ion and the color parameter b* increased with the increase in amount of V_2O_5. Mn^{3+} was reduced to Mn^{2+} (colorless) by Ce^{3+} ion and the color parameter a* increased with an increase in the amount of MnO_2. The combination of CeO_2-V_2O_5-MnO_2 colorants was unable to mimic the color of human teeth since the a* parameter was insufficient. The base composition of glass affected the lightness because it may enhance the refractive index of residual glassy matrix, resulting in a lower difference of refractive index with the crystalline phases. By adjusting the base glass composition and the use of proper colorants for chromaticity, appropriate colors for dental application was obtained by the optimization of colorant concentrations.

Table 6.1. Amount of CeO_2 and TiO_2 (in mol%), and CIElab color parameters L* (lightness), a* (green to red) and b* (blue to yellow) of the GCs samples.

Sample	CeO_2	TiO_2	L*	a*	b*
Series 1:					
Base	0	0	69.18	0.24	-1.77
Ce0.5	0.5	0	68.73	-0.70	-2.54
Ti0.5	0	0.5	70.79	-1.26	-3.73
Ce0.5Ti0.5	0.5	0.5	57.10	-3.45	3.65
Ce0.5Ti1.0	0.5	1.0	49.31	-4.37	6.90
Series 2:					
Ti0.5	0	0.5	70.79	-1.26	-3.73
Ce0.5Ti0.5	0.5	0.5	57.10	-3.45	3.65
Ce0.75Ti0.5	0.75	0.5	70.81	-2.72	5.02
Ce1.0Ti0.5	1.0	0.5	90.81	-2.89	4.82
Ce1.5Ti0.5	1.5	0.5	89.41	-1.76	3.96
Ce2.0Ti0.5	2.0	0.5	87.07	-1.24	3.08

Table 6.2. DSC characteristic temperatures of the glass samples measured with a heating rate of 10 °C/min in air, where T_g is the glass transition temperature, T_x is the onset temperature of the crystallization peak, T_p is the crystallization peak temperature, δT_p is the height of crystallization peak, and T_m is the melting peak temperature.

Sample ID	Glass transition	Exothermic peak			Melting peak
	T_g (°C)	T_x (°C)	T_p (°C)	δT_p (°C)	T_m (°C)
Series 1:					
Base	466.8	611.0	630.0	67.6	982.2
Ce0.5	467.1	614.5	633.1	65.0	978.8
Ti0.5	473.9	612.4	629.5	78.0	979.4
Ce0.5Ti0.5	476.3	616.7	635.0	72.4	975.7
Ce0.5Ti1.0	473.6	623.3	642.9	67.3	973.3
Series 2:					
Ti0.5	473.9	612.4	629.5	78.0	979.4
Ce0.5Ti0.5	476.3	616.7	635.0	72.4	975.7
Ce0.75Ti0.5	471.8	613.7	632.6	72.2	974.7
Ce1.0Ti0.5	470.2	628.6	650.0	61.6	973.0
Ce1.5Ti0.5	472.5	632.4	654.8	55.4	968.0
Ce2.0Ti0.5	473.2	640.3	666.5	46.4	968.0

Table 6.3. Calculated volume fraction of phases by the PONCKS method in the GCs samples.

Sample ID	Glass	LS2	LP	Cristobalite	CeO_2
Series 1:					
Base	23.7 ± 1.8	70.3 ± 1.5	4.6 ± 0.2	1.4 ± 1.2	0
Ce0.5	25.5 ± 1.1	70.7 ± 1.1	3.8 ± 0.1	0	0
Ti0.5	21.4 ± 2.1	72.9 ± 1.6	5.2 ± 0.1	0	0
Ce0.5Ti0.5	19.7 ± 2.1	75.7 ± 2.0	4.6 ± 0.1	0	0
Ce0.5Ti1.0	25.5 ± 2.4	70.1 ± 2.3	4.3 ± 0.2	0	0
Series 2:					
Ti0.5	21.4 ± 2.1	72.9 ± 1.6	5.2 ± 0.1	0	0
Ce0.5Ti0.5	19.7 ± 2.1	75.7 ± 2.0	4.6 ± 0.1	0	0
Ce0.75Ti0.5	29.0 ± 1.9	66.9 ± 1.8	4.1 ± 0.1	0	0
Ce1.0Ti0.5	26.3 ± 1.2	68.7 ± 1.0	4.0 ± 0.1	0	0.9 ± 0.1
Ce1.5Ti0.5	26.4 ± 0.6	68.5 ± 0.6	3.6 ± 0.1	0	1.6 ± 0.2
Ce2.0Ti0.5	27.2 ± 1.8	67.8 ± 1.7	2.4 ± 0.2	0	2.6 ± 0.1

Table 6.4. Compositions of the glass samples (mol%)

Sample ID	SiO_2	Li_2O	P_2O_5	K_2O	ZnO	Al_2O_3
Z	66.27	27.73	1.5	3	1.5	0
A	66.27	27.73	1.5	3	0	1.5
ZA	66.27	27.73	1.5	3	1.5	1.5
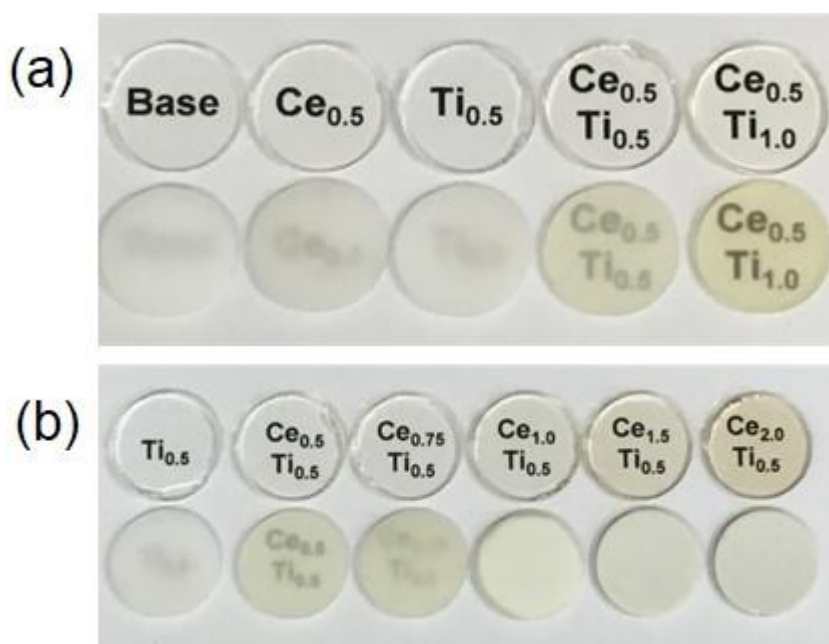
Fig. 6.1. Photographs of (a) mixture of CeO_2 and TiO_2 and (b) mixture of TiO_2 and with increasing the amount of CeO_2. The first low are glass samples and second low are GCs samples nucleated at 500 °C for 1 h and subsequently grown at 800 °C for 2 h.
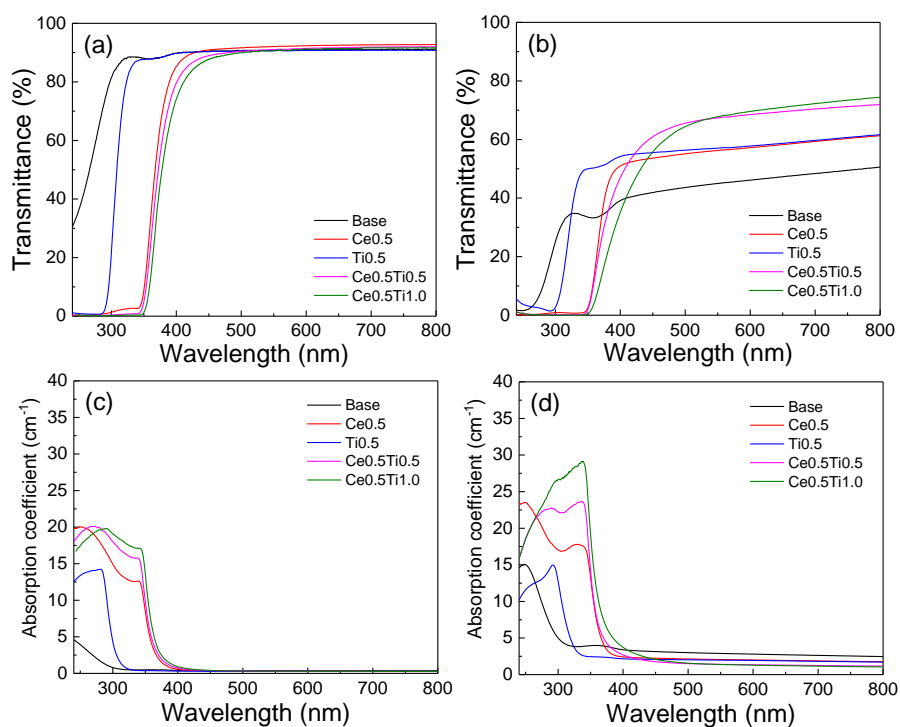
Fig. 6.2. Transmittance and absorption coefficient for Series 1 samples. (a) and (c) are glass samples, and (b) and (d) are GCs samples.
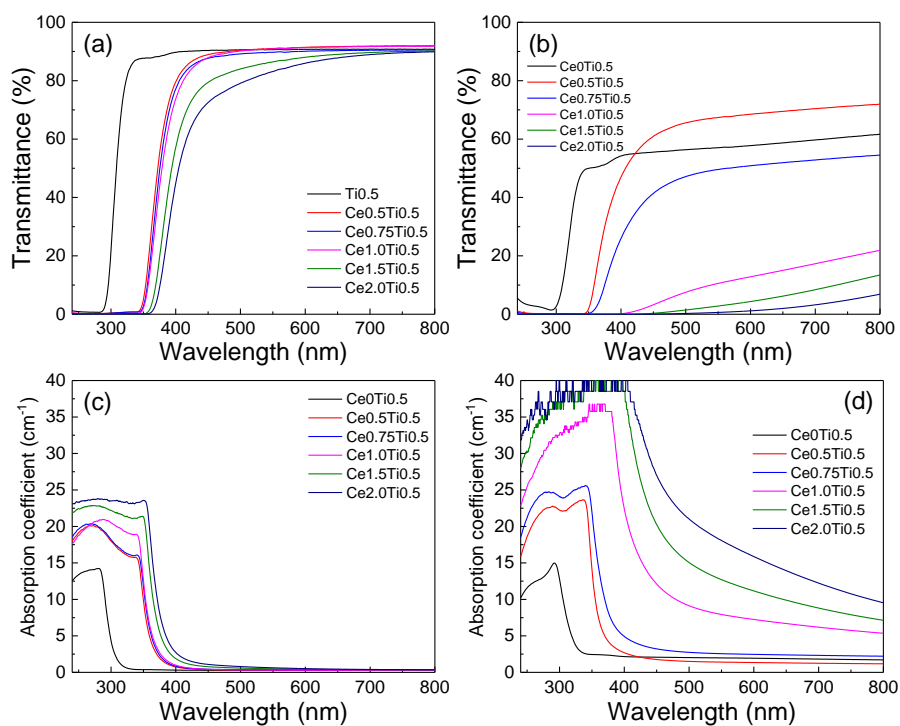
Fig. 6.3. Transmittance and absorption coefficient for Series 2 samples. (a) and (c) are glass samples and (b) and (d) are GCs samples.
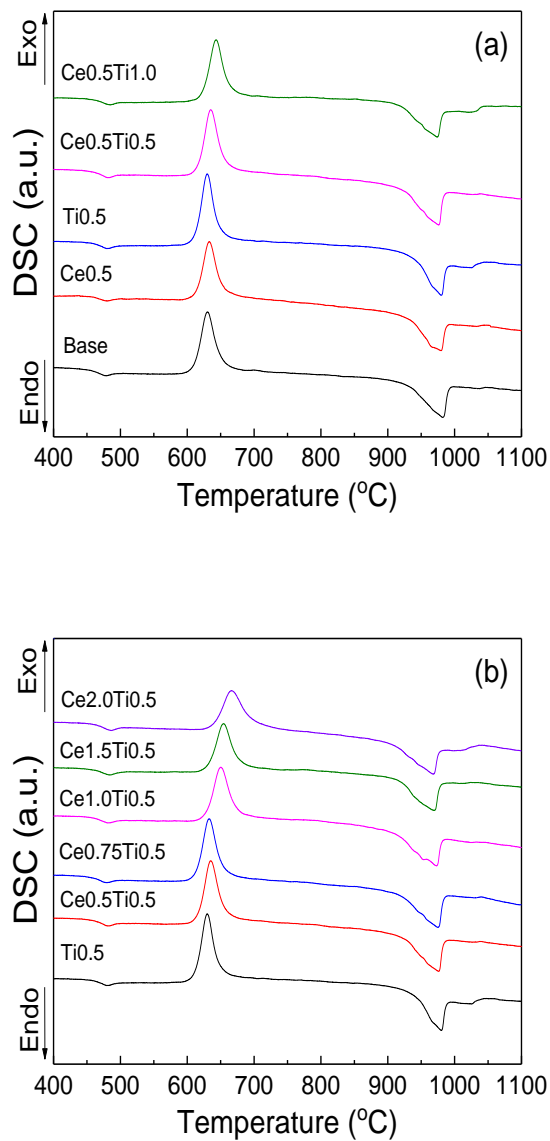
Fig. 6.4. DSC curves of the glass particles (a) series 1 and (b) series 2 with heating rate 10 ℃/min in air.
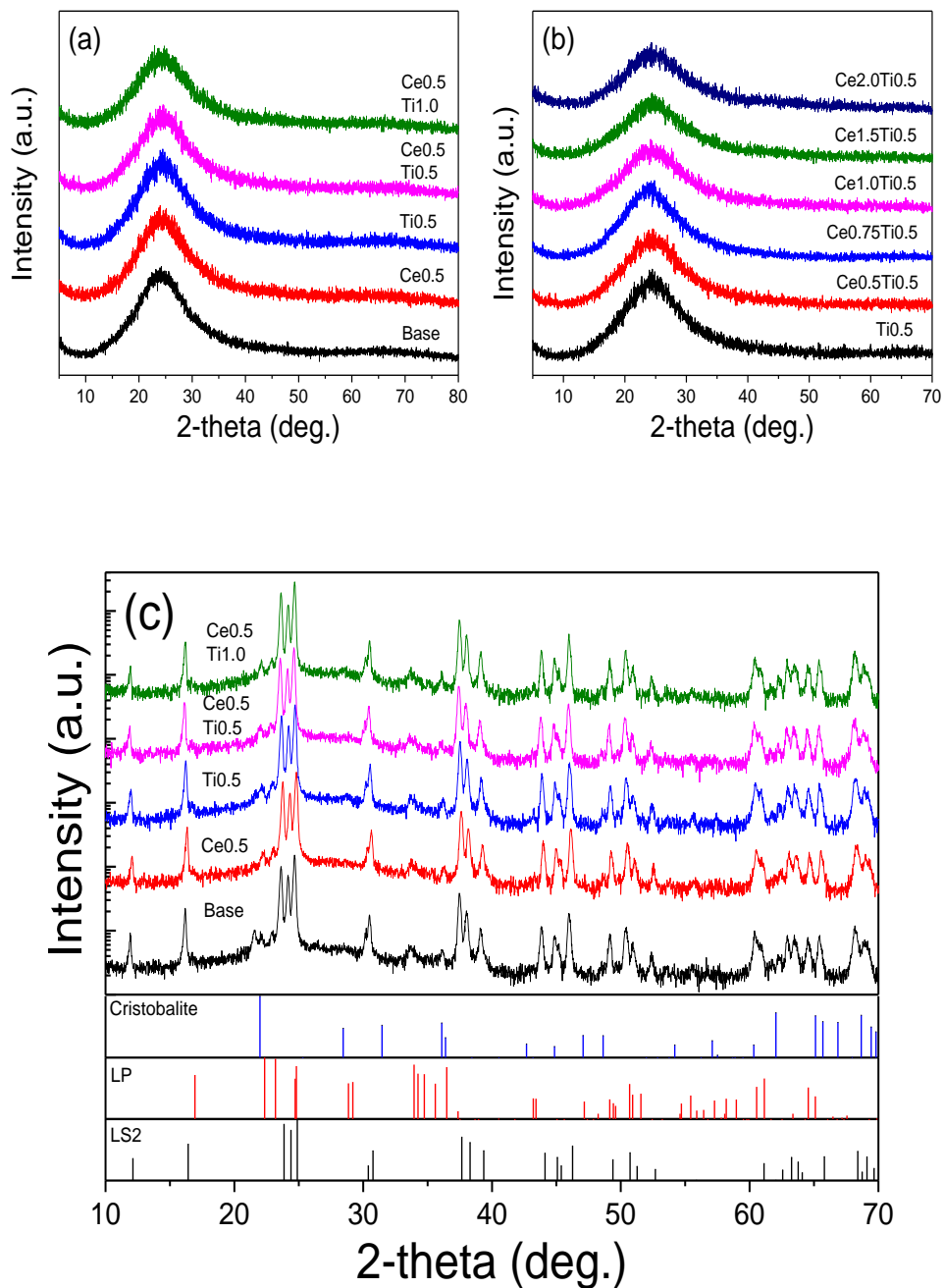
Fig. 6.5. XRD patterns of glass samples (a) series 1 and (b) series 2, and GC samples (c) series 1, and (d) series 2.
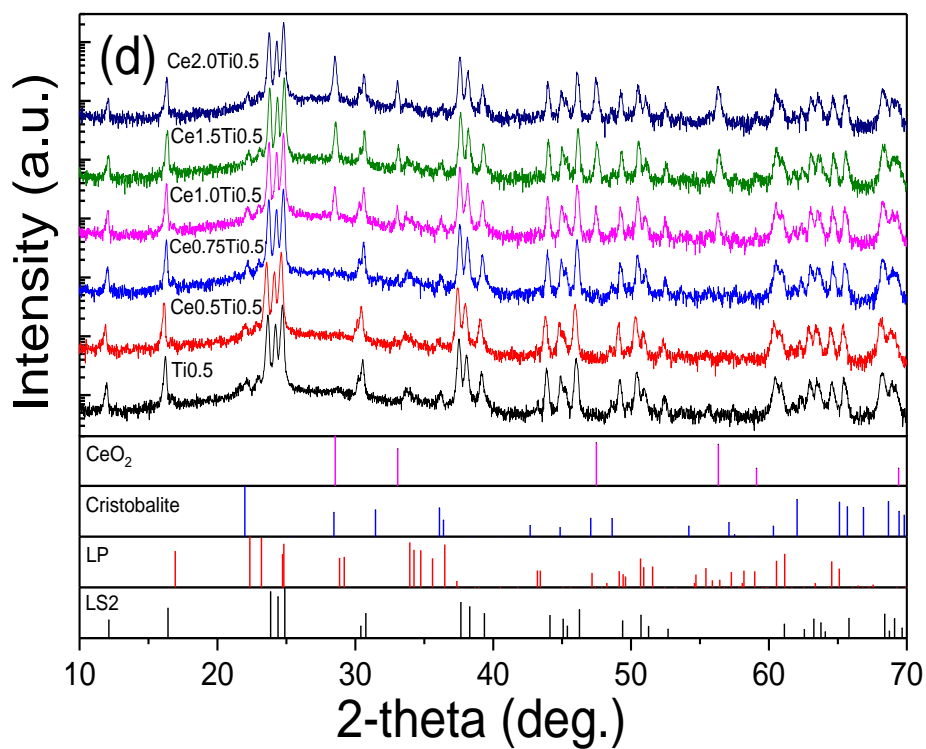
Fig. 6.5(d). (Continued)
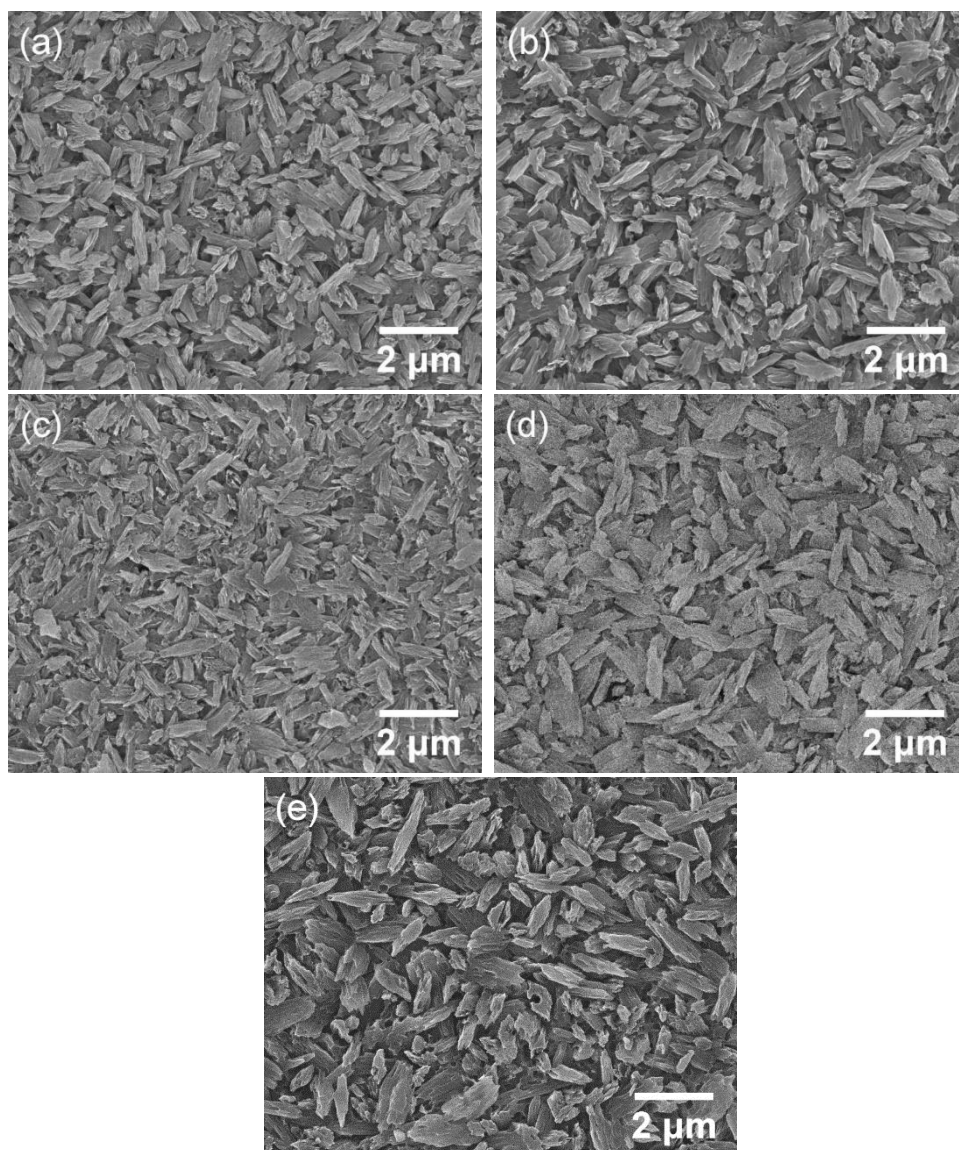
Fig. 6.6. Microstructures of GCs samples (a) Base, (b) Ce0.5, (c) Ti0.5, (d) Ce0.5Ti0.5 and (e) Ce0.5Ti1.0.
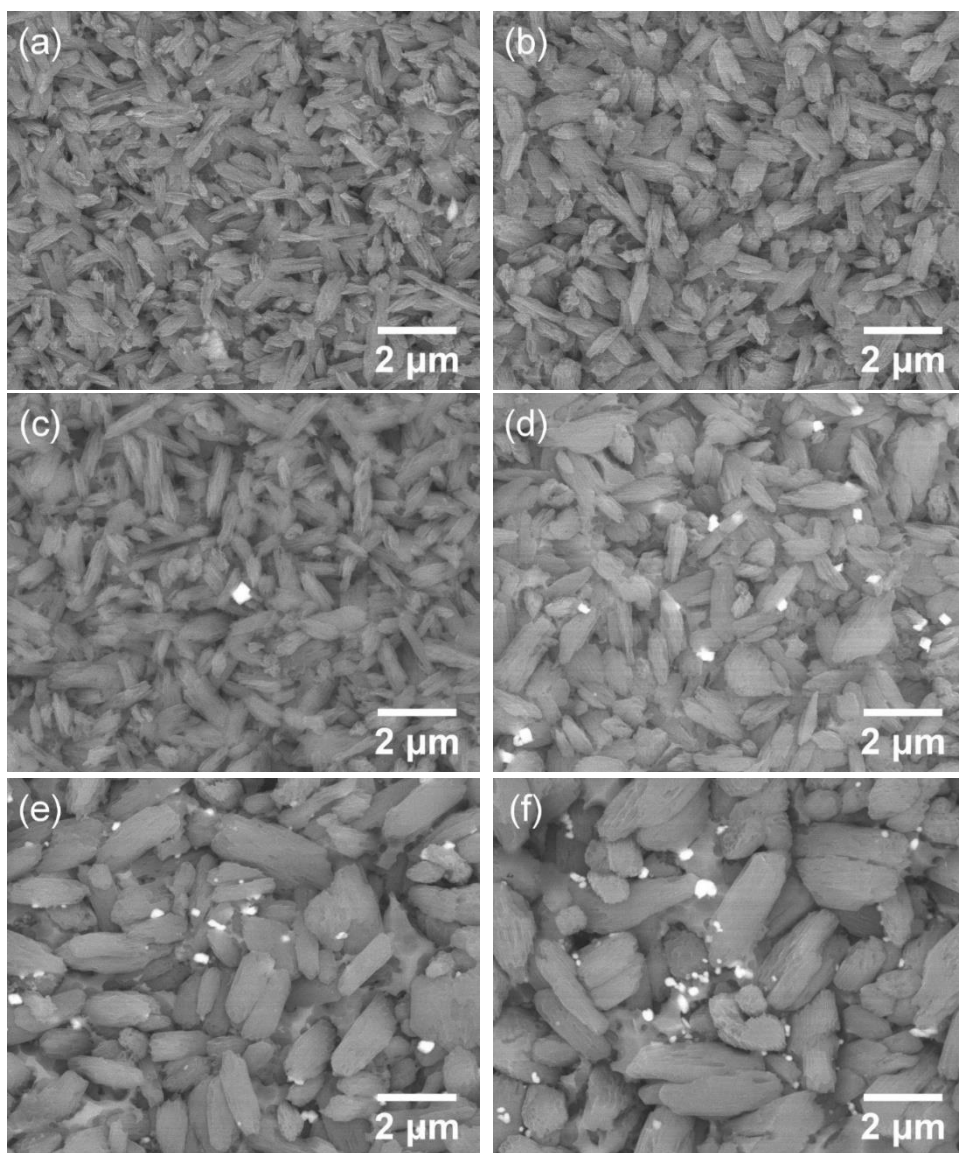
Fig. 6.7. Backscattered electron images of GCs samples (a) Ti0.5, (b) Ce0.5Ti0.5, (c) Ce0.75Ti0.5, (d) Ce1.0Ti0.5, (e) Ce1.5Ti0.5 and (f) Ce2.0Ti0.5.
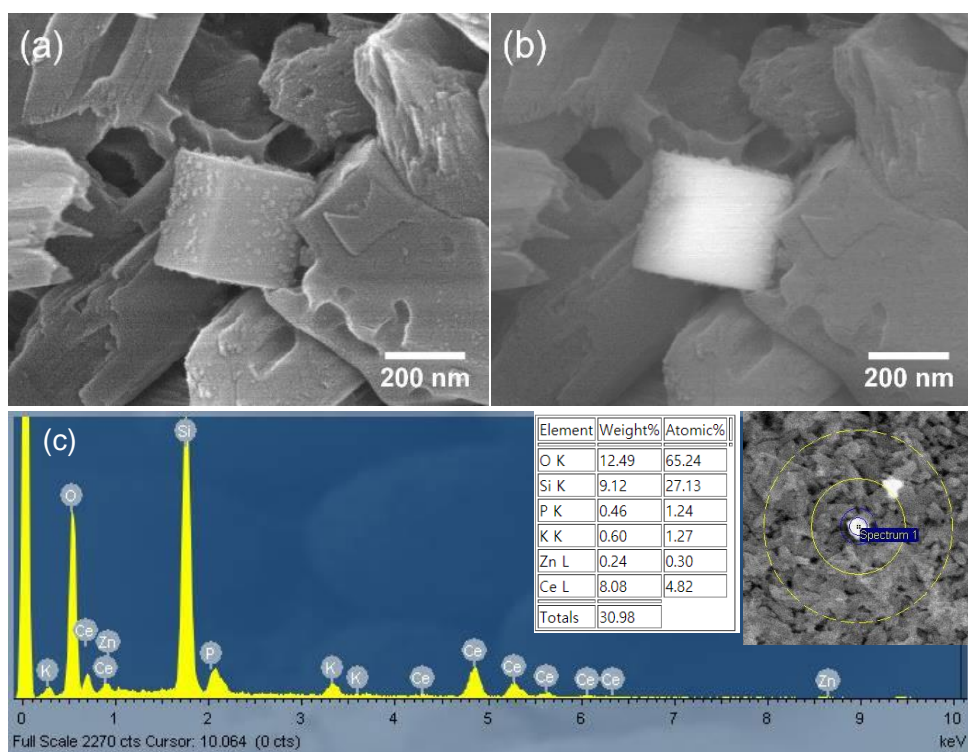
Fig. 6.8. (a) SEM micrograph and (b) back-scattered electron images and (c) SEM-EDS spectrum of Ce1.0Ti0.5 samples. The inset in (c) is quantitative analysis of point spectrum.
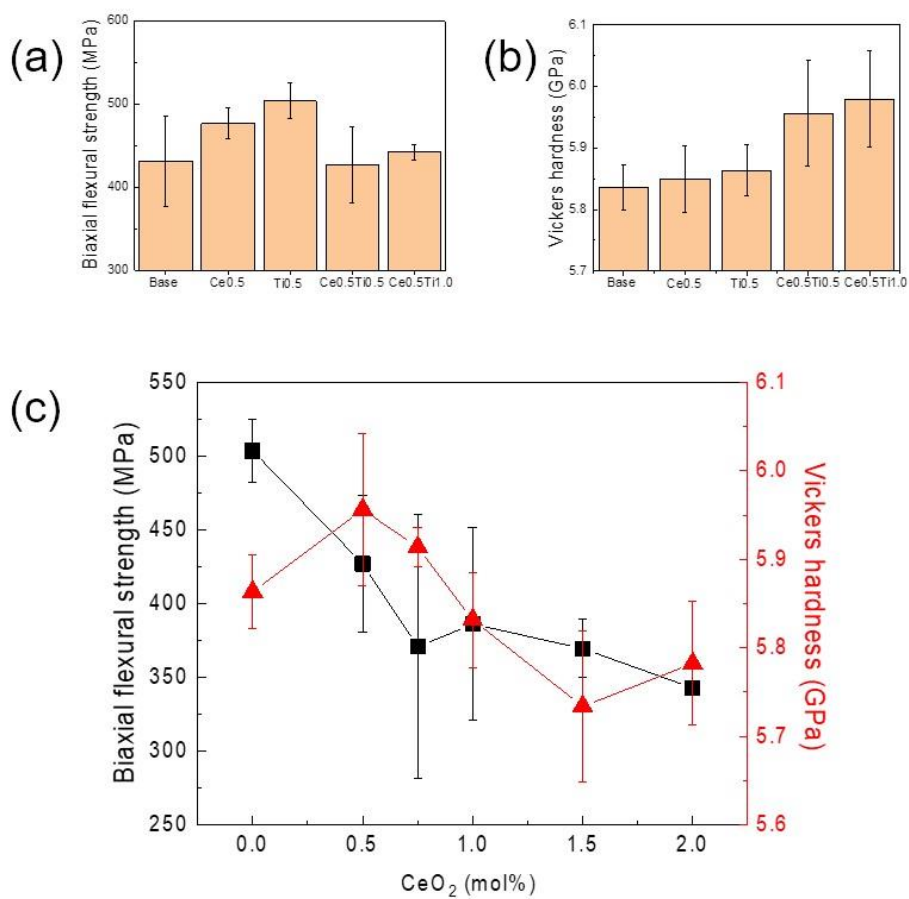
Fig. 6.9. (a) Biaxial flexural strength and (b) Vickers hardness of series 1 and (c) biaxial and Vickers hardness of series 2
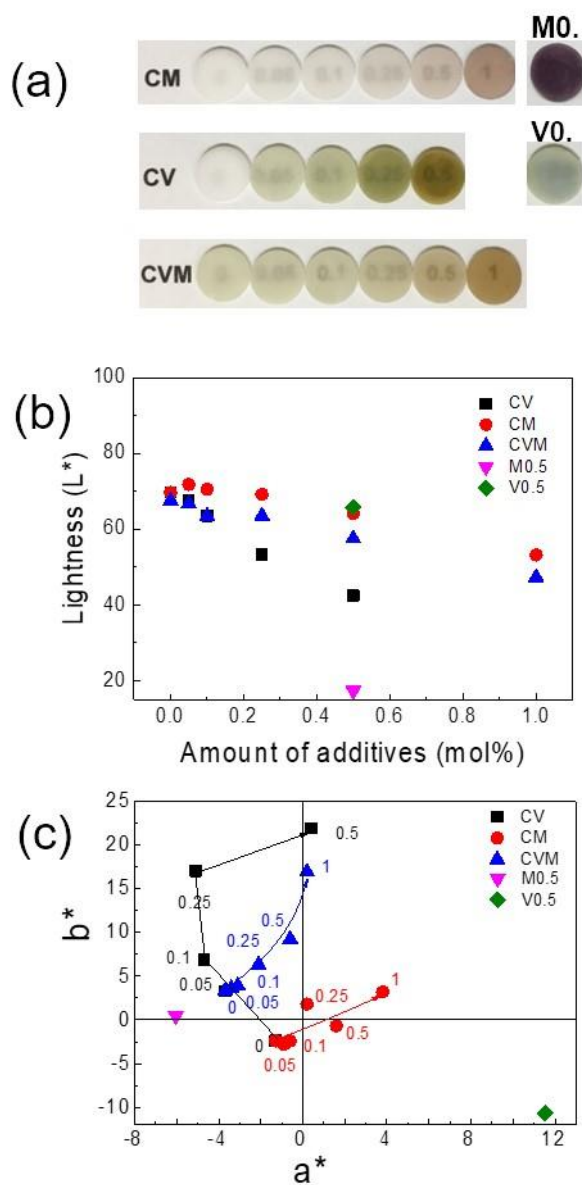
Fig. 6.10. (a) Photographs of GCs samples, (b) lightness L* and (b) chromaticity a* and b* with the amount of additives for CV, CM and CVM.
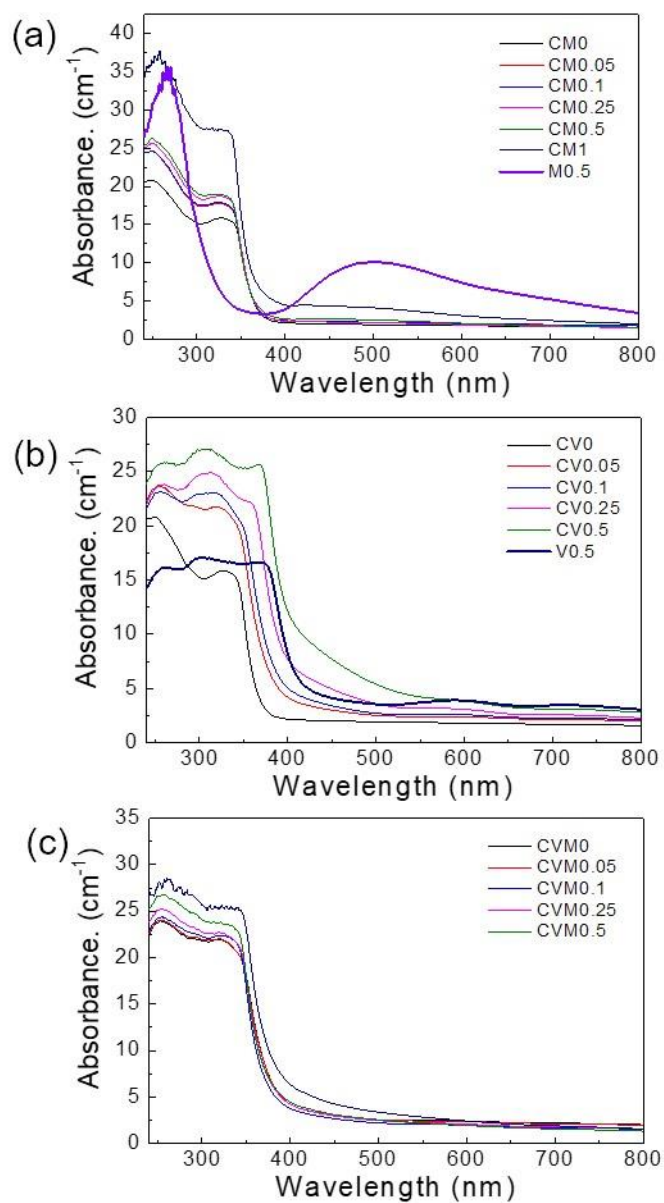
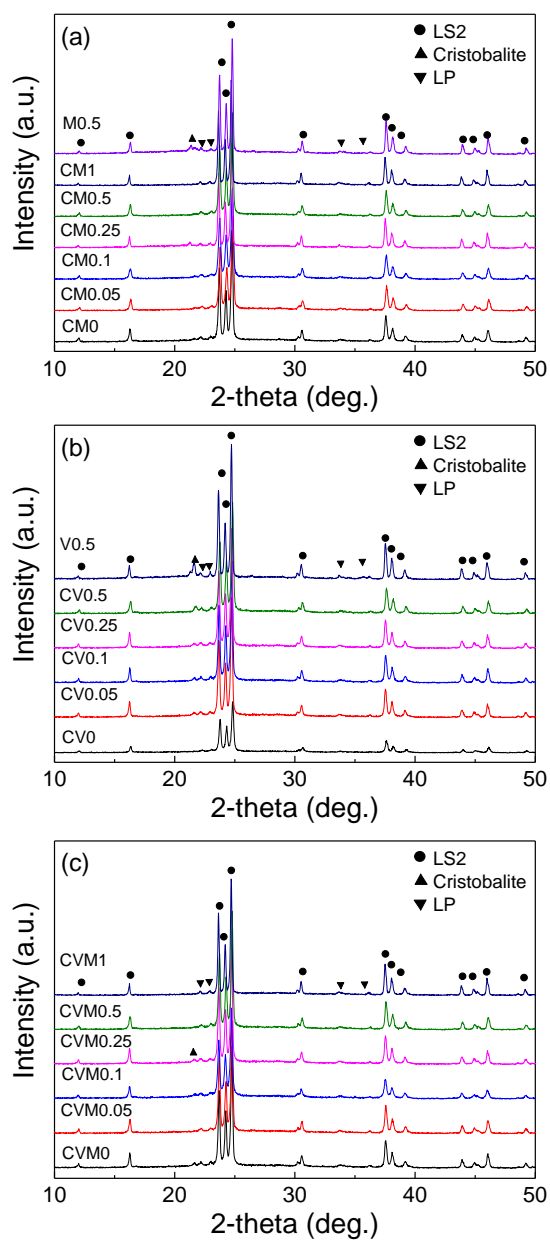**Fig. 6.11.** Absorbance of (a) CM, (c) CV and (e) CVM.

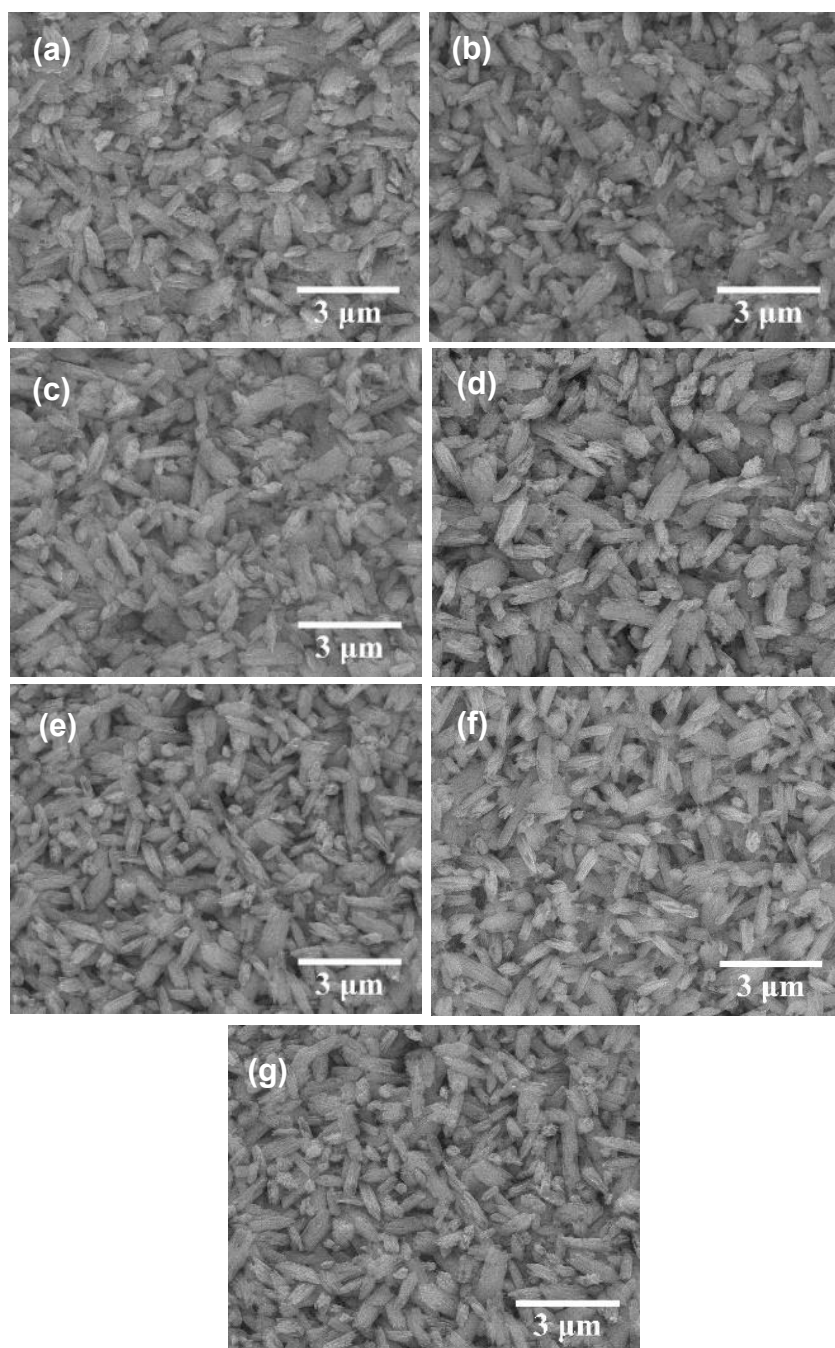**Fig. 6.12.** XRD patterns of the GCs samples of (a) CM, (b) CV, and (c) CVM.

Fig. 6.13. Microstructures of (a) CM0, (b) CM0.05, (c) CM0.1, (d) CM0.25, (e) CM0.5, (f) CM1 and (g) M0.5
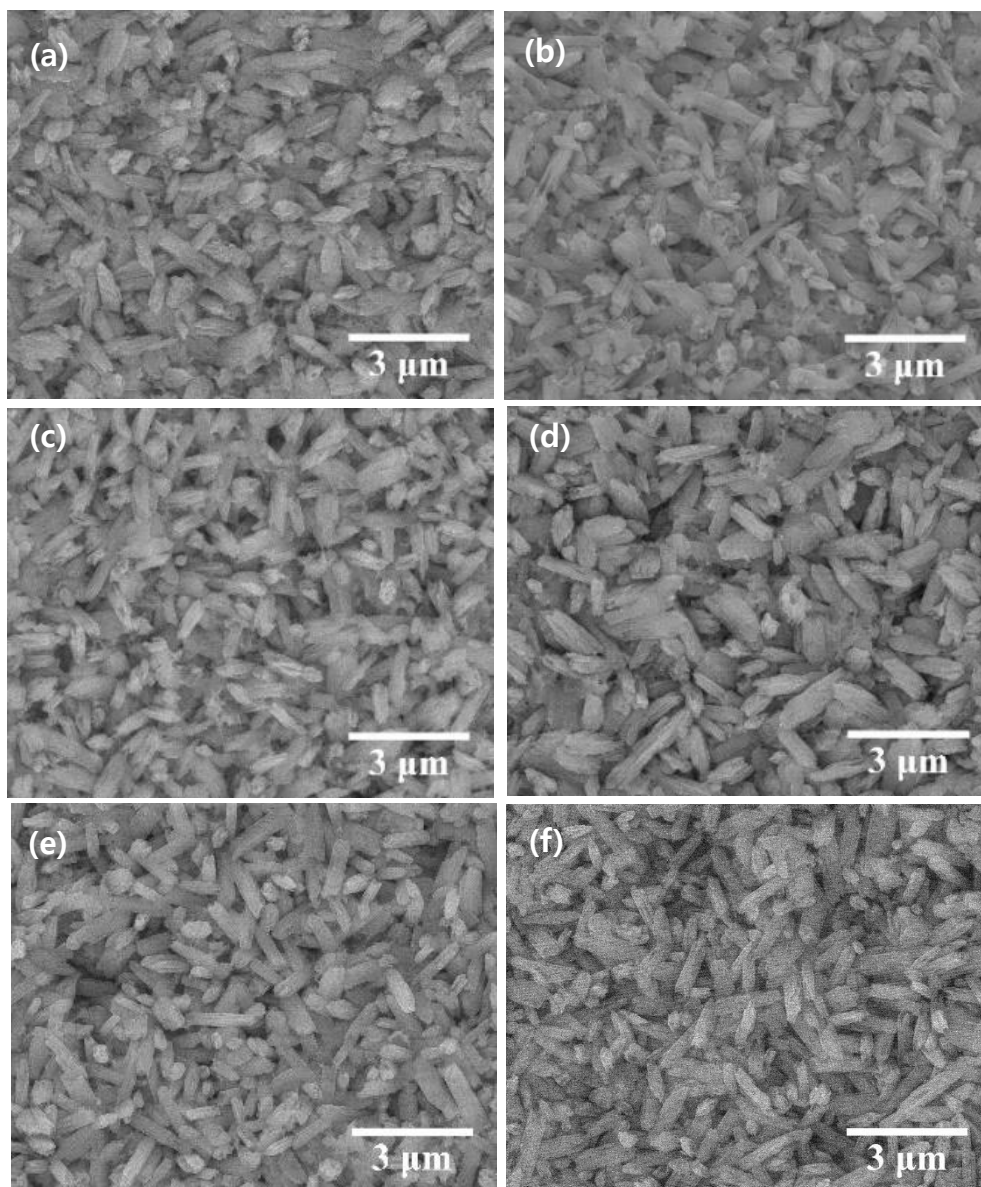
Fig. 6.14. Microstructures of (a) CV0, (b) CV0.05, (c) CV0.1, (d) CV0.25, (e) CV0.5, and (f) V0.5
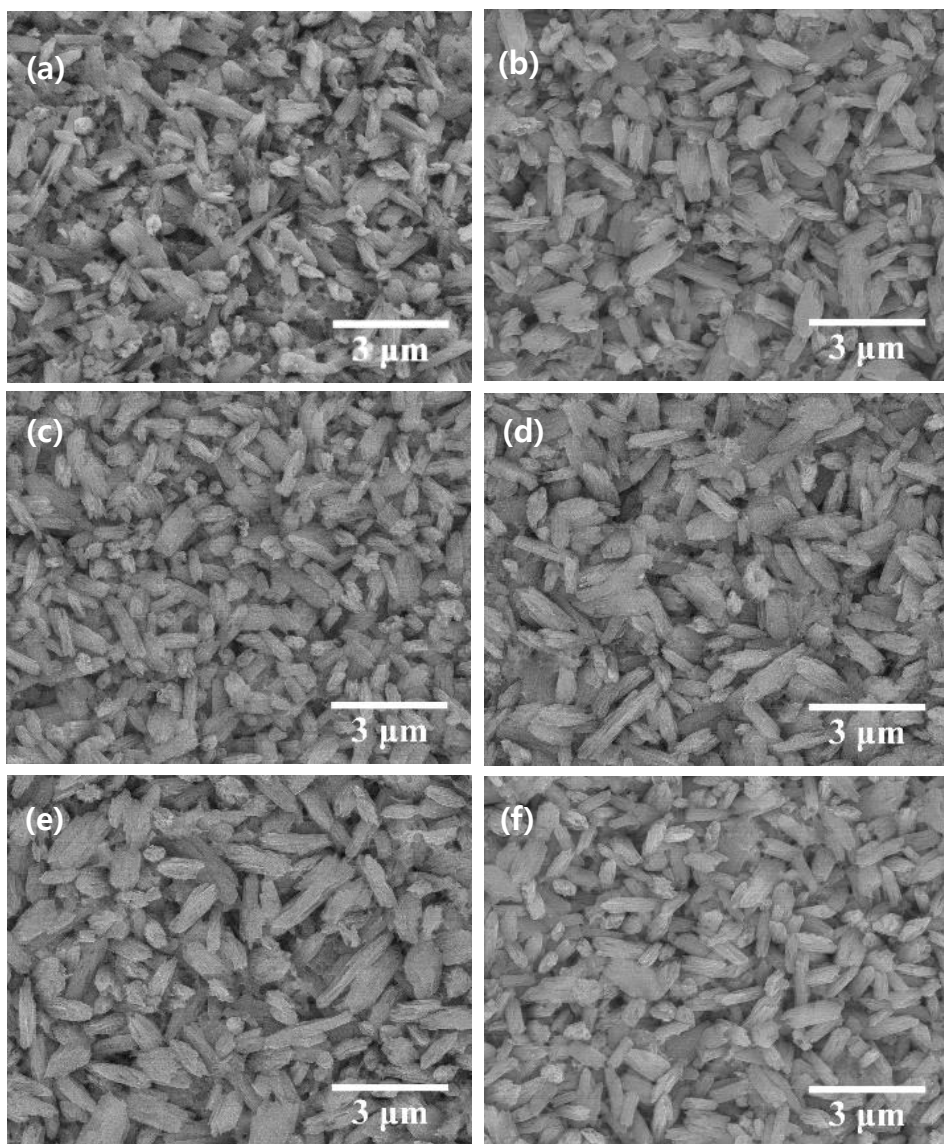
Fig. 6.15. Microstructures of (a) CVM0, (b) CVM0.05, (c) CVM0.1, (d) CVM0.25, (e) CVM0.5, and (f) CVM1.
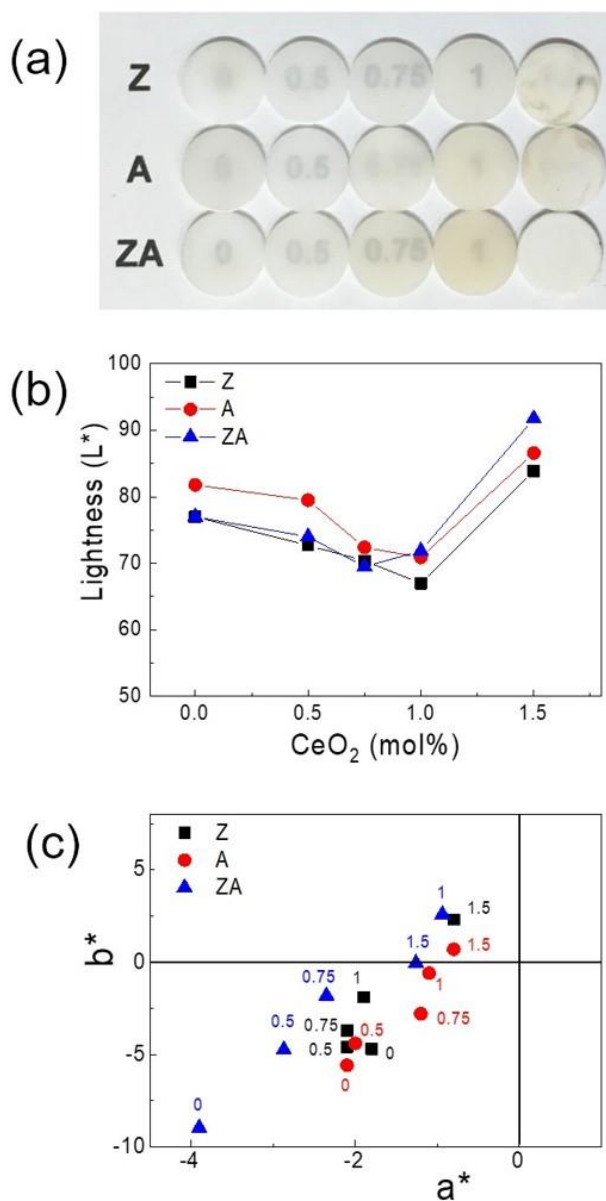
Fig. 6.16. (a) Photographs of GCs. The first low is Z and second low is A and third low is ZA samples. (b) lightness L* and (c) chromaticity a* and b* with the addition of CeO$_2$ 0, 0.5, 0.75, 1.0 and 1.5 mol%.
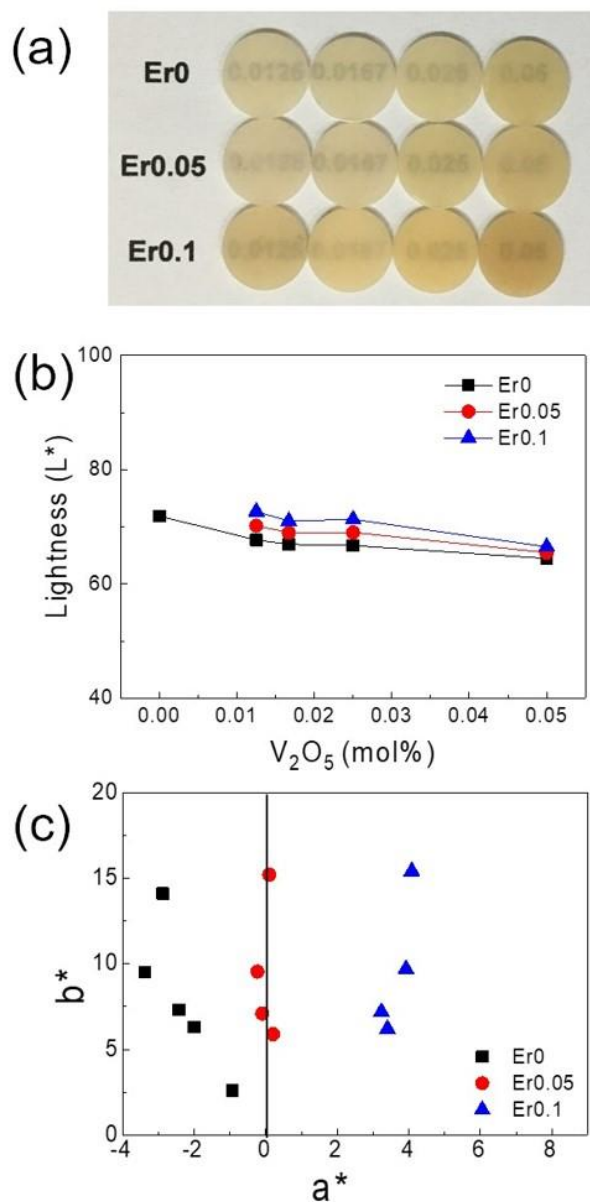
Fig. 6.17. (a) Photographs of GCs. The first low is Er0 and second low is Er0.05 and third low is Er0.1. The columns denote the addition of V_2O_5 0.0125, 0.0167, 0.25, 0.5 mol% from the left to right. (b) lightness L* and (c) chromaticity a* and b* with the addition of V_2O_5 0.0125, 0.0167, 0.25, 0.5 mol%.

Fig. 6.18. Absorbance of (a) Er0 and (b) Er0.1 GC samples with the addition of V_2O_5 0.0125, 0.0167, 0.25, 0.5 mol%.

Fig. 6.19. XRD patterns of the Er0.1 GC samples with the addition of V_2O_5 0.0125, 0.0167, 0.25, 0.5 mol%.

Fig. 6.20. Biaxial flexural strength versus amount of V_2O_5 with Er_2O_3 of 0, 0.05 and 0.1 mol%

References

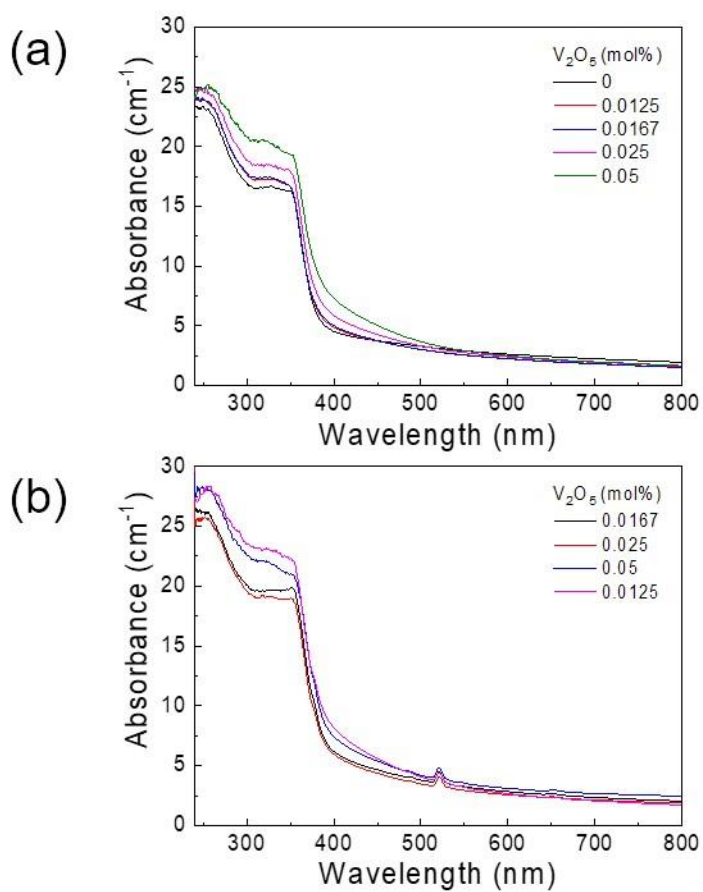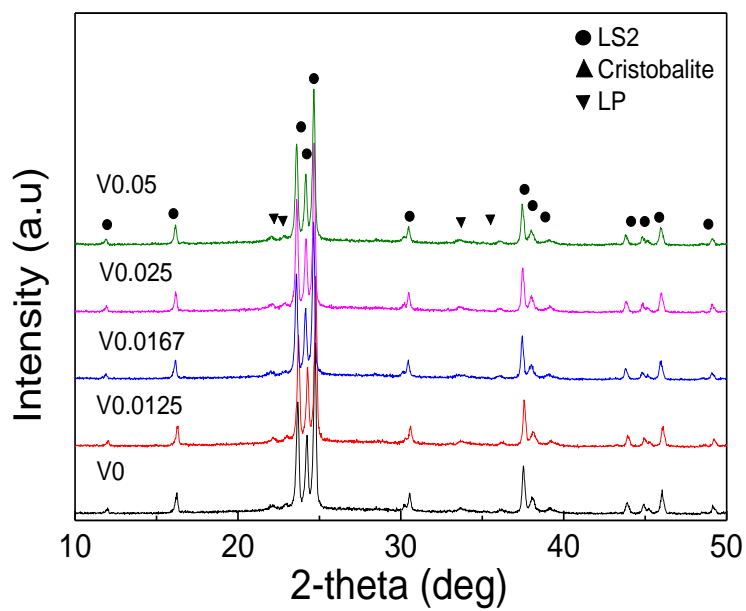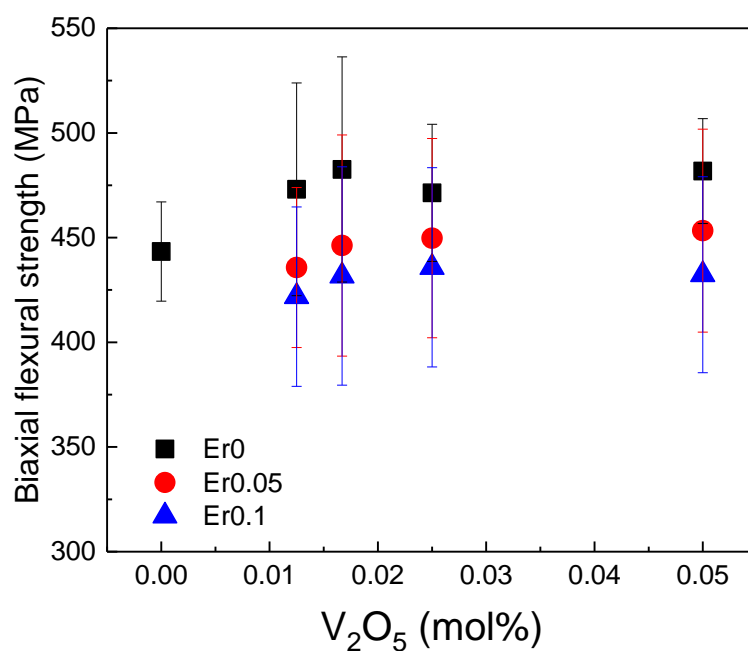[1] T. Berthier, V.M. Fokin, E.D. Zanotto, New large grain, highly cry stalline, transparent glass–ceramics, J. Non-Cryst. Solids, 354 (2008) 17 21-1730.

[2] E. El-Meliegy, R. van Noort, Glasses and Glass Ceramics for Med ical Applications, Springer Science & Business Media, 2011.

[3] M. Rubino, J. Garcia, L.J. Barco, J. Romero, Colour measurement of human teeth and evaluation of a colour guide, Color Research & A pplication, 19 (1994) 19-22.

[4] E. Trusova, N. Bobkova, V. Gurin, N. Gorbachuk, Formation of c oloring complexes in glass colored with cerium and titanium oxides, G lass Ceram., 64 (2007) 346-348.

[5] E. Trusova, N. Bobkova, V. Gurin, E. Tyavlovskaya, Nature of col or centers in silicate glasses with additions of cerium and titanium oxi des, Glass Ceram., 66 (2009) 240-244.

[6] C.B. Carter, M.G. Norton, Ceramic materials: science and engineeri ng, Springer Science & Business Media, 2007.

[7] A. İyiel, D. Öktem, F. Akmaz, Parameters Affecting the Color Me chanism of Manganese Containing Colored Glasses, J. Chem, 8 (2014) 849-858.

[8] A. Gaddam, H.R. Fernandes, D.U. Tulyaganov, M.J. Pascual, J.M. Ferreira, Role of manganese on the structure, crystallization and sinteri ng of non-stoichiometric lithium disilicate glasses, RSC Advances, 4 (2 014) 13581-13592.

[9] J. Wang, S. Yu, Q. Guan, Effect of transition metal ions Mn^{3+}, C o^{2+}, Ni^{2+} on the color of mixed Pr-Nd glasses, J. Non-Cryst. Solids, 5 2 (1982) 447-454.

[10] W. Kaewwiset, K. Thamaphat, J. Kaewkhao, P. Limsuwan, Er^{3+}-d oped soda-lime silicate glass: Artificial pink gemstone, American Journ al of Applied Sciences, 9 (2012) 1769-1775.

[11] A. Marotta, A. Buri, F. Branda, Nucleation in glass and differenti al thermal analysis, Journal of materials science, 16 (1981) 341-344.

[12] K. Moringa, H. Yoshida, H. Takebe, Compositional dependence of absorption spectra of Ti^{3+} in silicate, borate, and phosphate glasses, J. Am. Ceram. Soc., 77 (1994) 3113-3118.

[13] C.K. Jørgensen, S. Döger, M. Frydman, L. Sillén, Comparative lig and field studies IV. vandium (IV), titanium (III) and other systems wi th one d-electron, Acta Chem. Scand., 11 (1957) 73-85.

[14] R. Singh, S. Singh, Spectrochemical studies on charge transfer ba nds due to d^0, d^5 and d^{10} ions in a sodium silicate glass, Journal of materials science, 36 (2001) 1555-1562.

[15] M.-L. Brandily-Anne, J. Lumeau, L. Glebova, L.B. Glebov, Specif ic absorption spectra of cerium in multicomponent silicate glasses, J. N on-Cryst. Solids, 356 (2010) 2337-2343.

[16] J.L. Rygel, Y. Chen, C.G. Pantano, T. Shibata, J. Du, L. Kokou, R. Woodman, J. Belcher, Local structure of cerium in aluminophosphat e and silicophosphate glasses, J. Am. Ceram. Soc., 94 (2011) 2442-245 1.

[17] J.S. Stroud, Color centers in a cerium-containing silicate glass, Th e Journal of Chemical Physics, 37 (1962) 836-841.

[18] J.S. Stroud, Photoionization of Ce^{3+} in glass, The Journal of Che mical Physics, 35 (1961) 844-850.

[19] A. Herrmann, H.A. Othman, A.A. Assadi, M. Tiegel, S. Kuhn, C. Rüssel, Spectroscopic properties of cerium-doped aluminosilicate glasse s, Optical Materials Express, 5 (2015) 720-732.

[20] A.D. Sontakke, J. Ueda, J. Xu, K. Asami, M. Katayama, Y. Inad a, S. Tanabe, A comparison on Ce^{3+} luminescence in borate glass and YAG ceramic: understanding the role of host's characteristics, The Jour nal of Physical Chemistry C, 120 (2016) 17683-17691.

[21] A. Verma, A.G. Joshi, A. Bakhshi, S. Shivaprasad, S. Agnihotry, Variations in the structural, optical and electrochemical properties of C

eO$_2$–TiO$_2$ films as a function of TiO$_2$ content, Appl. Surf. Sci., 252 (2006) 5131-5142.

[22] A. Makishima, H. Kubo, K. Wada, Y. Kitami, T. Shimohira, Yellow Coatings Produced on Glasses and Aluminum by the Sol-Gel Process, J. Am. Ceram. Soc., 69 (1986) C-127-C-129.

[23] M. Sainz, A. Duran, J.F. Navarro, UV highly absorbent coatings with CeO$_2$ and TiO$_2$, J. Non-Cryst. Solids, 121 (1990) 315-318.

[24] M. Sainz, A. Duran, J. Fernandez Navarro, Titanium and cerium colouring in glasses, Glass Technol., 32 (1991) 99-101.

[25] A. Paul, Cerium-titanium yellow colour in glass, (1976).

[26] Z. Wang, L. Cheng, Gamma ray irradiation-induced variations in structure and optical properties of cerium/titanium-doped oxyfluoride transparent glass-ceramics, Mater. Res. Bull., 92 (2017) 104-112.

[27] E. Le Bourhis, Glass: mechanics and technology, John Wiley & Sons, 2008.

[28] K. Matusita, S. Sakka, T. Maki, M. Tashiro, Study on crystallization of glass by differential thermal analysis. Effect of added oxide on crystallization of Li$_2$O-SiO$_2$, Journal of Materials Science, 10 (1975) 94-100.

[29] C.S. Ray, Q. Yang, W.h. Huang, D.E. Day, Surface and internal crystallization in glasses as determined by differential thermal analysis, J. Am. Ceram. Soc., 79 (1996) 3155-3160.

[30] C.S. Ray, D.E. Day, An Analysis of Nucleation-Rate Type of Curves in Glass as Determined by Differential Thermal Analysis, J. Am. Ceram. Soc., 80 (1997) 3100-3108.

[31] M.C. Weinberg, Interpretation of DTA experiments used for crystal nucleation rate determinations, J. Am. Ceram. Soc., 74 (1991) 1905-1909.

[32] P.W. McMillan, Glass-ceramics, (1964).

[33] H. Bach, D. Krause, Low thermal expansion glass ceramics, Springer Science & Business Media, 2005.

[34] U. Schiffner, W. Pannhorst, Nucleation in a precursor glass for a Li_2O-Al_2O_3—SiO_2 glass ceramic. I: Nucleation kinetics, Glastechnische Berichte, 60 (1987) 211-221.

[35] E. Kleebusch, C. Patzig, M. Krause, Y. Hu, T. Höche, C. Rüssel, The effect of TiO_2 on nucleation and crystallization of a Li_2O-Al_2O_3-SiO_2 glass investigated by XANES and STEM, Scientific Reports, 8 (2018) 1-8.

[36] H.R. Fernandes, D.U. Tulyaganov, J.M.F. Ferreira, The role of P_2O_5, TiO_2 and ZrO_2 as nucleating agents on microstructure and crystallization behaviour of lithium disilicate-based glass, Journal of Materials Science, 48 (2012) 765-773.

[37] K. Thieme, C. Rüssel, CeO_2 and Y_2O_3 as nucleation inhibitors in lithium disilicate glasses, Journal of Materials Science, 51 (2016) 989-999.

[38] K. Thieme, C.J.J.o.M.S. Rüssel, The effect of dopants on crystal growth kinetics of lithium disilicate: surface versus bulk crystallization, 54 (2019) 1099-1111.

[39] R. Bueno, J. Martinez-Duart, M. Hernandez-Velez, L. Vazquez, Optical and structural characterization of rf sputtered CeO_2 thin films, Journal of materials science, 32 (1997) 1861-1865.

[40] R.J. Tilley, Colour and the optical properties of materials: an exploration of the relationship between light, the optical properties of materials and colour, John Wiley & Sons, 2010.

[41] A.M. Nassar, N. Ghoneim, Vanadium contribution in different glasses in view of the ligand field theory, J. Non-Cryst. Solids, 46 (1981) 181-195.

[42] R.A. El-Mallawany, Tellurite glasses handbook: physical properties and data, CRC press, 2011.

Chapter 7

Conclusion

The purpose of this study was to improve the strength of LS2 GCs with microstructure engineering by changing the crystallization sequence of the GCs. The crystallization sequence was controlled from sequence type II (LS) to type I (LS+LS2) through Z/K ratio. As a result, at a low Z/K ratio, crystallization sequence type II is induced, and the metastable LS phase is first crystallized and reacts with the SiO_2 phase at high temperatures to form LS2, thereby obtaining a needle-shaped crystal with a large aspect ratio. At high Z/K ratio, crystallization sequence type I was induced to improve the nucleation of LS2, resulting in fine crystal morphology of equiaxed crystals.

It was investigated the effect of the fine microstructure of the GCs on the mechanical properties and found that when the crystal size decreased from 10 μm to 270 nm, the biaxial strength and the Vickers hardness increased in accordance with the Hall-Petch relation. However, when 8.4 vol% of cristobalite was included, severe scattering occurred in strength regardless of crystal size. This was due to the beta-to-alpha phase transformation of cristobalite. In addition, it was found that when the thermal expansion coefficient of the residual glass material is increased and larger than the thermal expansion coefficient of the LS2 crystal, tensile stress is generated in the residual glass material which lowered the mechanical strength. It was

suggested that the cristobalite should not be included as much as possible, and that the mechanical strength could be improved by controlling the thermal expansion coefficient of the residual glass and causing the crystal size smaller.

Since it is necessary to mimic the color of human teeth in order to use dental applications, the coloration mechanism and coloration of LS2 GCs have been studied. As a result, it was found that the colorant ion is mainly located in the residual glassy matrix and the composition of the residual glassy matrix changes as the crystallization progresses, affecting the valency of the colorant ion and altering absorption i.e. color. Therefore, it was found that even the same colorant can develop different colors after crystallization.

Since yellowish color is required to mimic the color of human teeth, the effect of CeO_2 and TiO_2 colorants on coloration, crystallization and mechanical properties was investigated. Although Ti^{4+} reduced Ce^{4+} to Ce^{3+}, it was effective to obtain yellowish color, however, the translucency was excessively improved, causing it more transparent than that of human teeth. When a large amount of CeO_2 was added exceeding 1 mol%, CeO_2 nanocrystals precipitated, resulting in Rayleigh scattering and significantly lowered the translucency. The CeO_2 colorant lowered the nucleation rate of the LS2 crystals, thereby increasing the size of the LS2 crystals, thus reducing strength and hardness. Thus, it was suggested that the addition of CeO_2 is minimized not to cause the precipitation of CeO_2 nanocrystal.

For optimization of coloration for dental application, CeO_2 and V_2O_5 was selected for yellowish color and MnO_2 was selected for reddish color to investigate the effect on coloration and crystallization. As a result, the yellowish color was satisfactory, however, the reddish color was insufficient. Therefore, Er_2O_3 was selected for

Chapter 7: Conclusion

reddish color and CeO_2-V_2O_5-Er_2O_3 mixture experiment was performed. As a result, it was possible to derive additive ratios that can reproduce human teeth while showing mechanical strength of 430 MPa.

국문 초록

리튬 다이실리케이트 결정화 유리의 미세구조, 기계적 물성 및 착색 특성

김 다 미

서울대학교 공과대학 재료공학부

세계적으로 인구 고령화에 따른 치아상실 및 치주질환이 증가하고 있어 치과 보철물의 수요가 증가하고 있다. 다양한 치과 재료 중에서도, 임플란트 크라운 소재인 리튬다이실리케이트 결정화 유리는 우수한 기계적 물성과 심미성으로 전치부에 적용되어 오고 있다. 최근 환자의 상당수가 노령으로 인한 잇몸뼈의 약화로 잇몸뼈에 식립하는 고정체를 여러 개 사용할 수 없어 프레임워크 고정성 보철의 수요가 증가하고 있다. 고정성 보철물은 기존 크라운 보다 높은 기계적 물성이 요구 되기 때문에 리튬다이실리케이트 결정화 유리의 기계적 물성의 향상이 필요하다. 리튬다이실리케이트 결정화 유리의 기계적 물성 향상 시키기 위해 여러 연구들이 수행되었지만 괄목할 만한 결과가 없는 상황이다. 결정화 유리의 기계적 강도 향상을 위해서는 미세구조의 제어가

필수적이나, 미세구조 제어에 관한 체계적인 연구는 충분히 시도된 적이 없었다.

따라서 본 연구에서는 SiO_2-Li_2O-K_2O-ZnO-P_2O_5 시스템에서 기존 연구에서 제안 되지 않은 결정화 순서를 변화시켜 미세구조 제어하는 새로운 접근 방법을 개발하고자 하였고 이를 통해 드라마틱한 미세구조 제어 가능성을 확인하였다. 결정화 순서를 조절하기 위해 핵형성제인 P_2O_5 는 1.5 mol%로 고정하고 유리수식제인 ZnO + K_2O 는 4.5 mol% 로 고정한 후, ZnO/K_2O (Z/K) 비율 0 에서 3.5 로 변화시키고 결정화 거동과 미세구조를 살펴보았다. K 의 비율이 큰 조성에서 결정화 순서 II (LS)를 보였고, 초기 열처리 과정에서 준안정상인 리튬메타실리케이트 상이 먼저 핵형성 및 결정성장을 일으키고 800 도 이상의 고온에서 실리카 상과의 고체반응으로 장단축비가 큰 바늘 모양의 결정으로 구성되는 미세구조를 얻을 수 있었다. 반대로 Zn 의 비율이 큰 조성에서는 결정화 순서가 II 에서 I (LS+LS2) 로 점차 변화하였고 이를 통해 초기 열처리 과정에서 리튬메타실리케이트 상 뿐만 아니라 리튬다이실리케이트 상의 핵형성이 향상되어 핵수가 비약적으로 증가함에 따라 결정크기가 미세해지고 장단축비가 감소하여 최종적으로 등방상의 결정구조로 이루어진 미세구조를 얻을 수 있었다. 본 결과를 통해 첨가제의 비율을 조절하여 결정화 순서를 변화 시켜 미세구조를 장단축비가 큰 바늘 상의 구조로부터 등방상의 결정구조로 드라마틱한 변화를 유도할 수 있다는 것을 최초로 밝혀냈다.

이를 통해 미세구조제어가 가능해졌기 때문에 SiO_2-Li_2O-K_2O-P_2O_5 시스템에서 제어된 미세구조가 기계적 강도에 미치는 영향을 조사하였다. 미세구조를 제어하기 위해 6 mol%의 첨가제 (P_2O_5, ZnO,

K$_2$O) 의 비율을 조절하여 3 개의 조성을 디자인하였고 한 조성 당 12 개의 열처리 조건을 통해 결정화 유리를 제조하였다. 그 결과, 결정화 유리의 평균 결정 크기는 0.3-10 μm 이었고, 결정상의 부피 분율은 0.70-0.73 이었다. ~10 에서 ~1 μm 의 결정 크기에서는 크리스토발라이트 상이 존재하지 않을 때 결정크기가 감소할수록 Hall-Petch 관계식에 따라 이축 굴곡 강도가 향상되었고 2.75 mol% P$_2$O$_5$, 2.7 5mol% K$_2$O, 2 mol% ZnO 조성에서 540 ℃ 에서 1 시간 동안 핵형성 시키고 850 ℃ 에서 4 시간 성장 시켰을 때 445.8 ± 7.2 MPa 의 최대 굴곡 강도가 얻어졌다. 크리스토발라이트상이 8.4 vol% 포함되었을 때는 결정 크기에 관계없이 강도값에서 심한 편차를 보인 반면 경도는 Hall-Petch 관계에 따라 증가하였다. 이는 열처리 후 상온으로 냉각 시 고온에서 형성된 크리스토발라이트 상이 베타상에서 알파상으로 상전이를 일으켜 발생한 미세균열 때문인 것으로 밝혀졌다. 뿐만 아니라 P$_2$O$_5$ 와 Z/K 비율이 증가할수록 잔류유리질의 열팽창계수가 비약적으로 증가하여 결정상 과의 열팽창계수 차이가 커짐에 따라 잔류유리질에 인장응력이 발생하여 강도가 감소하는 것을 확인하였다. 이를 통해 크리스토발라이트 상은 포함되지 않아야 하고 결정화 후 잔류유리질의 열팽창계수의 증가를 일으키지 않는 조성을 설계해야 기계적 물성을 향상시킬 수 있는 가능성을 발견하였다.

또한 리튬다이실리케이트의 치과소재로서의 적용을 위해서는 심미성을 만족시키기 위해 자연 치아와 유사한 색과 투명도의 재현이 필수적이다. 그러나 결정화 유리는 결정화 과정 때문에 착색제의 연구가 매우 어렵고 보고가 드문 실정이다. 따라서 본 연구에서는 결정화 유리의 착색제의 착색 메커니즘을 규명하고 이를 통해 자연치아와

유사한 색과 투명도를 얻기 위해 여러 개의 착색제를 선정하고 그 비율을 조절하였다.

착색 매커니즘을 규명하기 위해서 노란색을 발현한다고 알려져 있는 V_2O_5 을 선정하고 $SiO_2-Li_2O-K_2O-P_2O_5-ZnO$, $SiO_2-Li_2O-K_2O-P_2O_5-Al_2O_3$ 시스템의 기본 유리 조성에서 ZnO/K_2O (Zn/K) 과 Al_2O_3/K_2O(Al/K) 의 비율이 V_2O_5 의 valency 에 미치는 영향을 살펴보았다. 그 결과, 착색제 이온은 초기에 V^{5+}으로 유리에 존재하나, 결정화가 진행될수록 V^{4+}, V^{3+} 로 환원이 되었고 이로 인해 약한 초록색의 유리에서 파란색, 보라색, 초록색, 갈색의 다양한 색의 결정화 유리가 얻어졌다. 이는 착색제 이온이 결정화가 진행됨에 따라 잔류유리질에 포함되게 되는데 결정화에 따라 잔류유리질의 조성이 변화하기 때문에 착색제 이온의 valency 가 변화하는 것을 발견하였다. 이를 통해 같은 착색제 이온이라도 잔류유리질의 조성에 따라 발현되는 색이 달라지기 때문에 잔류유리질의 디자인이 결정화 유리의 착색에 매우 중요하다는 것을 처음으로 규명했다.

이와 같은 이해를 바탕으로, 자연치아와 유사한 색을 재현하기 위 노란색을 발현하다고 알려져 있는 CeO_2 와 TiO_2 의 비율을 조절하여 착색 및 결정화 거동, 기계적 물성에 미치는 영향에 대해서 확인하고자 하였다. 그 결과, CeO_2, TiO_2 동시 첨가는 Ti^{4+} 이온이 Ce^{4+} 을 Ce^{3+}으로 환원하여 노란색 발현의 정도가 증가하였으나 자연치아 색에서 필요한 빨간색의 발현이 감소하였고, 크라운 소재 적용에 불가할 정도의 투명도 향상을 보였다. CeO_2 1 mol% 이상의 첨가에서 CeO_2 이차상이 석출되어 자연 치아의 투명도보다 낮아 지는 것을 확인하였고

CeO_2 가 LS2 결정의 핵형성 억제제로 작용하여 결정 크기가 증가함에 따라 기계적 강도의 감소를 초래한 것을 발견하였다.

빨간색 발현을 위해 MnO_2 를 선정하여 CeO_2-V_2O_5-MnO_2 의 mixture 실험 결과 노란색 발현 효과는 있었지만 빨간 색 발현은 미미하였으며 투명도가 높아지는 점을 발견하였다. 이는 빨간색을 발현하는 Mn^{3+} 이온이 Ce^{4+}, V^{5+} 에 의해 무색의 Mn^{2+} 으로 환원되기 때문이라는 것을 밝혀냈다. 따라서 다른 첨가제에 의해 valency 가 변화하지 않는 착색제의 선택이 중요하다는 것을 확인하였다. 빨간색 발현을 위해 Er_2O_3 을 선정하여 CeO_2-V_2O_5-Er_2O_3 mixture 실험 결과, 자연치아와 유사한 색을 발현하는 조성 비를 도출할 수 있었고 기계적 강도가 430 MPa 인 자연치아와 유사한 GCs 를 제조할 수 있었다.

키워드: 리튬다이실리케이트, 결정화 유리, 미세구조 최적화, 기계적 물성, 광학적 특성

학번: 2015-30178

Dami Kim

Research Area

Fabrication and microstructure engineering of lithium disilicate glass-ceramics and characterization of their mechanical, optical properties.

Education

2015.3–2020.8 **Ph.D.**
Department of Materials Science and Engineering
Seoul National University, Seoul, Korea
Supervisor: Prof. Sang-Im Yoo

2011.3–2013.2 **M.S.**
Division of Materials Science and Engineering
Hanyang University, Seoul, Korea
Supervisor: Prof. Sung-Churl Choi

2007.3–2011.2 **B.S.**
Department of Ceramic Engineering
Gyeongsang National University, Jinju, Korea

Publications (1st Author: 6, Contributed papers: 3)
Citation: 15, *h*-index: 2 (2020.7)

1st Author

1. **<u>Dami Kim</u>**, H. J. Kim, and S. I. Yoo, "Optimization of colorant in lithium disilicate glass-ceramics for the dental application" (*in preparation*)

2. **<u>Dami Kim</u>**, H. J. Kim, and S. I. Yoo, "Optical and mechanical properties of CeO_2/TiO_2 doped lithium disilicate glass-ceramics for dental application", (*in preparation*)

3. **<u>Dami Kim</u>**, A. Sharma, and S. I. Yoo, "Effect of Ge doping in the electrical, optical and TFT properties of Zn-Sn-O semiconductor", (*in preparation*)

4. **<u>Dami Kim</u>**, H. J. Kim, and S. I. Yoo, "Effects of microstructures on the mechanical properties of lithium disilicate glass-ceramics for the SiO_2-Li_2O-P_2O_5-K_2O-ZnO system", (*submitted to Materials Science and Engineering A*)

5. **<u>Dami Kim</u>**, H. J. Kim, and S. I. Yoo, "Effect of V_2O_5 colorant on the optical properties and crystallization behaviors of lithium disilicate glass-ceramics", *Journal of Alloys and Compounds*, 836, (25) pp. 155333. (2020).

6. **<u>Dami Kim</u>**, H. J. Kim, and S. I. Yoo, "Effect of ZnO/K_2O ratio on the crystallization sequence and microstructure of lithium disilicate glass-ceramics.", *Journal of European Ceramic Society*, 39, pp. 5077–5085 (2019).

Contributed papers

7. C. Y. Bon, **<u>Dami Kim</u>**, K. Y Lee, S. J. Choi, I. S. Park and S. I. Yoo, "Enhanced electrical properties of Nb-doped HfO2 high-κ dielectrics in MIM capacitor", *(in preparation)*

8. A. Sharma, **<u>Dami Kim</u>**, and S. I. Yoo, "Subsolidus phase diagram in the GeO_2–ZnO–SnO_2 system at 1100° C in air" (in press, *Current Applied Physics)*

9. A. Sharma, **Dami Kim**, and S. I. Yoo, "Subsolidus phase diagram in the GeO$_2$–ZnO–SnO$_2$ system at 1100° C in air" *Ceramics International*, 44(8), pp. 9848–9853 (2018).

Acknowledgement (감사의 글)